The Dissertation Committee for Brennan Donovan Dubuc
certifies that this is the approved version of the following dissertation:

Acoustoelasticity and Data Processing for Acoustic-Based Corrosion Monitoring in Structures

Committee:

_____

Salvatore Salamone, Supervisor

_____

Raissa Ferron

_____

Loukas Kallivokas

_____

Preston Wilson

Acoustoelasticity and Data Processing for Acoustic-Based Corrosion Monitoring in Structures

by

Brennan Donovan Dubuc

Dissertation

Presented to the Faculty of the Graduate School
of the University of Texas at Austin
in Partial Fulfillment
of the Requirements
for the Degree of

Doctor of Philosophy

The University of Texas at Austin

May 2020

For Irene

Acknowledgments

The research presented in this thesis was not carried out in a vacuum. Many people across the civil and mechanical engineering departments at the University of Texas were instrumental in the progression of this work. I would first like to thank my entire committee for the time they invested in considering and evaluating my doctoral work, including Profs. Salvatore Salamone, Raissa Ferron, Loukas Kallivokas, and Preston Wilson. Special thanks are due to my supervisor Prof. Salamone for creating a constructive working environment and continually pushing and supporting me through the advancement of my research. For the funding of all the research carried out in this thesis, I would like to thank the Texas Department of Transportation. On a related note, thanks are also due to the Center for Transportation Research team of Prof. Ferron, Mr. Mike Rung, and Ms. Savitha Sagari for valuable discussions and experimental assistance. I would like to thank Dr. Arvin Ebrahimkhanlou for extensive assistance in preparing and conducting experiments, as well as for countless helpful discussions. A number of undergraduate and graduate students also assisted with experimental and data analysis aspects at various points during the project, including Mr. Marco Munoz, Ms. Xinran (Annie) Li, Ms. Marina Nakajima, Ms. Vinutha Kancharla, and Mr. Konstantinos Sitaropoulos. The team at the Ferguson Structural Engineering Laboratory were very helpful in experimental aspects, including Mr. David Braley, Mr. Dennis Filip, and Dr. Mike Brown. I would also like to thank everyone else in the Smart Structures Research Group for providing a great working environment, including Mr. Korkut Kaynardag, Mr. Stylianos Livadiotis, Dr. Apostolos Athanasiou, Ms. Melanie Schneider, and Mr. Chi Yang.

Lastly, and most importantly, I would like to thank Irene for giving me the reason for all my hard work.

Acoustoelasticity and Data Processing for Acoustic-Based Corrosion Monitoring in Structures

by

Brennan Donovan Dubuc, Ph.D.

The University of Texas at Austin, 2020

SUPERVISOR: Salvatore Salamone

Corrosion is one of greatest concerns in a variety structures, from cable-stayed and suspension bridges to prestressed and post-tensioned concrete members. The common theme in these structures is corrosion of the load-bearing steel strands. These members carry significantly larger stresses compared to steel reinforcing bars, and corrosion can therefore be particularly catastrophic. Aiming towards real-time diagnosis and prognosis, this thesis investigates active and passive acoustic methods for nondestructive corrosion monitoring in steel strands and prestressed concrete, while incorporating advanced data processing techniques. The main goal is to take advantage of complex acoustic data in new ways, allowing the extraction of richer and more robust corrosion information for longterm monitoring.

Guided waves and acoustic emission constitute the active and passive acoustic methods considered, with each designed to target a unique aspect of the corrosion process. Guided waves are used to actively interrogate the stress redistribution within a corroding strand, which may point to loss of load-carrying capacity. On the other

hand, acoustic emission is used to passively monitor corrosion and its various mechanisms (*e.g.*, concrete cracking and steel pitting). Several data processing techniques are adapted and proposed to realize these aims, including time-frequency transforms, modal modulation, data fusion, topological data analysis, and hidden Markov modeling. In addition, acoustoelasticity theory is advanced in order to predict the effect of stress on guided wave propagation in strands. Particular emphasis is placed on higher-order guided wave modes, which possess several advantageous characteristics for corrosion-induced stress monitoring.

To validate the abovementioned acoustic methods, accelerated corrosion experiments were conducted on loaded strands and small-scale prestressed concrete specimens. The experiments were designed to evaluate the performance of guided waves in monitoring corrosion-induced stress redistribution, as well as acoustic emission in monitoring the evolution of corrosion mechanisms. The results showed that higher-order guided wave modes were able to reveal the underlying trend in stress redistribution, as well as critical moments like wire fracture. In addition, the topology of acoustic emission data was shown to indicate mechanisms appearing at the onset of corrosion. Combining this information with traditional frequency analyses through hidden Markov modeling then allowed for a realtime automated diagnosis of the corrosion process.

Contents

List of Tables

List of Figures

Nomenclature

Acronyms

AE	Acoustic emission
DAQ	Data acquisition
GPR	Gaussian process regression
GW	Guided wave
HMM	Hidden Markov model
KED	Kinetic energy density
RA/AF	Risetime-amplitude/average frequency
SHM	Structural health monitoring
TDA	Topological data analysis
UTS	Ultimate tensile strength

Notation

a	Scalar
$\mathbf{a}$	Vector or matrix
$\hat{a}$	Fourier transform
$\tilde{a}$	Wavelet transform
$\bar{a}$	Normalized value
$\breve{a}$	Excluded quantity
$\{a\}$	List
$\langle \mathbf{a} \rangle$	Simplex
A	Simplicial complex
$\mathcal{A}$	Transform operator
$\mathbb{A}$	Probability operator
$\mathscr{A}$	Body, energy, or collection
Δa	Change in a quantity
$\mathrm{d}a$	Differential quantity
a'	Incremental quantity
$a^{(m)}$	Quantity for m-th mode
$a^{\langle m \rangle}$	Quantity for m-th mode pair
$a_{\cdot}, a_{\cdot\cdot}$	Covariant component (placeholder "$\cdot$" may take on i, j, k, l)
$a^{\cdot}, a^{\cdot\cdot}$	Contravariant component (placeholder "$\cdot$" may take on i, j, k, l)
$a^{\cdot}_{\cdot}$	Mixed component (placeholder "$\cdot$" may take on i, j, k, l)
a_c	Value at c-th corrosion cycle

Operators

$\mathcal{F}$	Fourier transform
$\mathcal{W}$	Wavelet transform
$\mathcal{H}$	Hilbert transform
$\mathcal{E}$	Envelope operator
$\partial_0, \partial_1, \ldots$	Boundary operators
$\mathbb{P}$	Probability
$\mathbb{E}$	Expected value
$\lvert \cdot \rvert$	Absolute value
$\lvert\lvert \cdot \rvert\rvert_2$	ℓ_2-norm
max	Maximum
arg max	Argument yielding maximum
det	Determinant
ker	Kernel
img	Image
rank	Rank
$\cdot$	Dot product
$\times$	Cross product
$\cdot^{\mathrm{T}}$	Transpose
$\cdot^{-1}$	Inverse
$\cdot^*$	Complex conjugate
$\Re$	Real part
$\cup$	Union
$\setminus$	Set minus
$\lvert$	Given
$\ddot{\cdot}$	Double time derivative
$\cdot_{,i}$	Derivative with respect to i-th curvilinear coordinate
$\lvert_i$	Covariant derivative with respect to undeformed body
$\lvert\lvert_i$	Covariant derivative with respect to predeformed body

CHAPTER 1

Introduction

1 Corrosion in Structures

Corrosion has been identified as the single greatest problem facing infrastructure in the United States [3]. Corrosion-related costs in infrastructure, in particular, make up about 16% of the total corrosion costs across the country [1], as illustrated in Fig. 1.1. This damage mechanism remains a consistent threat, with its total cost constituting roughly 3% gross domestic product over the last several decades [1, 2], also shown in Fig. 1.1. Aside from the large direct costs of infrastructure corrosion, indirect costs (*e.g.*, traffic congestion due to repairs) have been estimated at an order of magnitude larger [3].

The implications of corrosion may be immediately seen in the many examples of deteriorating infrastructure worldwide: the Ynys-y-Gwas bridge in the United Kingdom collapsed without warning in 1985 due to unseen corrosion in its prestressing strands [4]; similar unforeseen collapses occurred in the Italian Saint Stefano bridge in 1999 and soon after in a pedestrian bridge at Lowe's Motor Speedway in 2000 [5]. These examples particularly highlight the susceptibility and implications of corrosion in the primary load-bearing steel strands and cables.

With the widespread implications of corrosion, however, also comes significant room for improvement. At the forefront, this includes economic and human losses associated with failures in corrosion-susceptible infrastructure. Along with reducing the need for rebuilding efforts after such failures also comes reduced pollution and

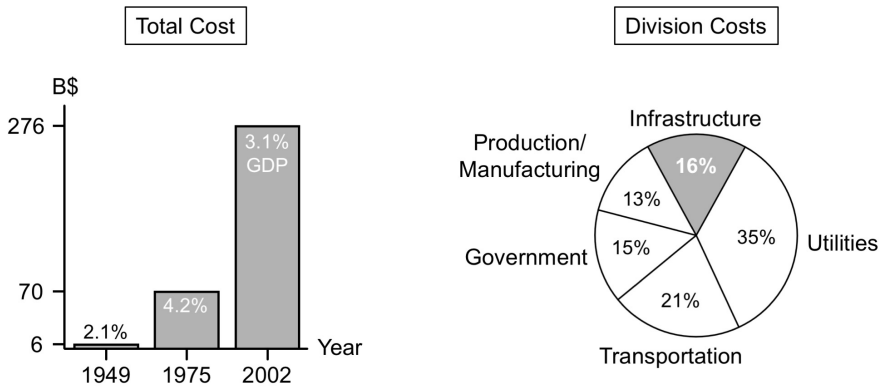

Fig. 1.1 Corrosion costs in the United States, in terms of total amount and distribution across various divisions. (Data obtained from [1, 2].)

increased resource conservation [3]. The construction process for reinforced and pre-stressed concrete structures in particular is highly consumptive [6]. Lastly, the ability to monitor corrosion in its early stages and over time may also constitute a step toward quantifying the resilience of structures within the wider contexts of cities and communities.

1.1 Steel strands

Under marine-like conditions, the electrochemical process of corrosion in steel (*i.e.*, the consuming of its primary constituent, Iron), may be described as follows [7]:

$$\begin{aligned} \mathrm{Fe} &\rightarrow \mathrm{Fe}^{2+} + 2\mathrm{e}^- \\ \mathrm{O}_2 + 2\mathrm{H}_2\mathrm{O} + 4\mathrm{e}^- &\rightarrow 4\mathrm{OH}^- \\ \mathrm{Fe}^{2+} + 2\mathrm{OH}^- &\rightarrow \mathrm{Fe(OH)}_2 \\ \mathrm{Fe(OH)}_2 + \mathrm{O}_2 &\rightarrow \gamma\text{-FeOOH} + \mathrm{H}_2\mathrm{O} \end{aligned} \tag{1.1}$$

where γ-FeOOH is ferric oxide. Corrosion in a load-bearing steel strand can lead to stress redistribution and increases, as visualized in Fig. 1.2. Such stress increases are caused by the loss of material along a segment of strand, where the load carried is distributed over a smaller cross-section. Before corrosion reaches catastrophic levels

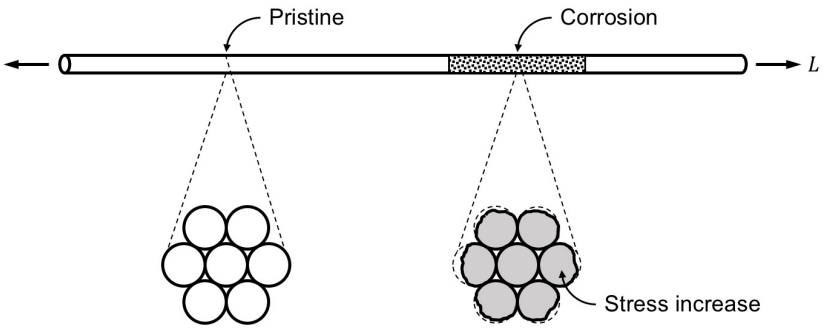

Fig. 1.2 Illustration of corrosion in a strand under some axial load L. Cross-sections at pristine and corroded locations along the strand shown, with the area of stress increase over the reduced cross-section highlighted.

and consumes material throughout an entire bundle of strands, it first targets the peripheral wires in a given strand. Due to their positioning, these outer wires then tend to shield the core wire from corrosion. This shielding behavior is visualized in Fig. 1.2 and may be seen in a variety of studies [8–10]. Aside from the situation of uniform corrosion, this behavior has also been built in to models of pit-depth distribution in strands [11], with the pitting taking place in the peripheral wires. From these considerations, stress changes within a strand are intimately linked to corrosion.

1.2 Prestressed concrete

When a strand is embedded in concrete, the progression of corrosion is somewhat more complicated. Corrosion in prestressed concrete is often due to the penetration of chlorides (such as from deicing salts or marine exposure) from the outer concrete surface. In this scenario, the electrochemical process building off of Eq. (1.1) may be described as [7]

$$\mathrm{Fe(OH)_2 + H^+ + Cl^- \rightarrow FeCl_2 + H_2O} \tag{1.2}$$

A widely accepted model of chloride-induced corrosion in concrete is that of Tuutti [12, 13]. Although this model was originally designed for reinforced concrete

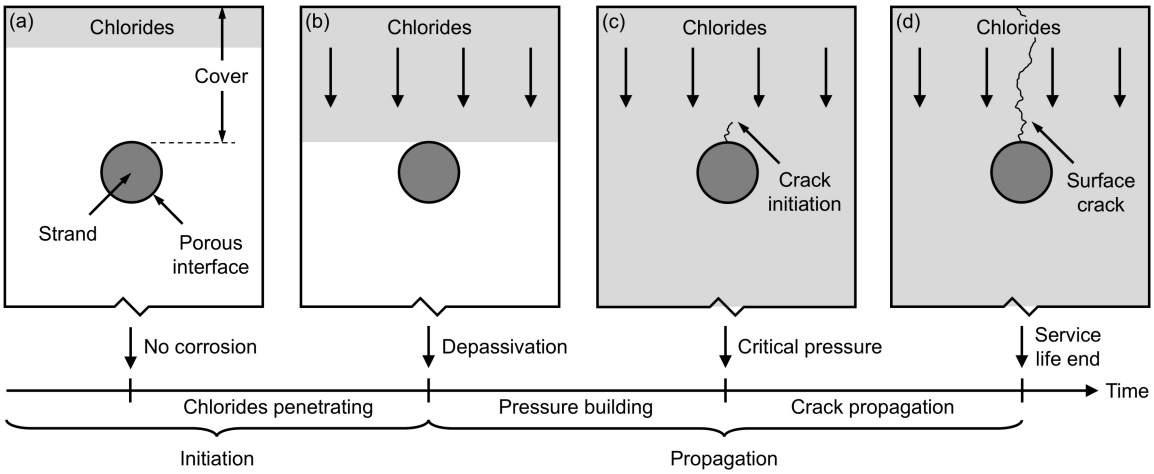

Fig. 1.3 Illustration of chloride-induced corrosion in prestressed concrete cross-section. (a) No corrosion before chlorides reach strand. (b) Depassivation when chlorides penetrate to strand. (c) Corrosion products have expanded into porous interface, reaching critical pressure for crack initiation. (d) End of service life when crack reaches surface.

(as opposed to prestressed concrete), the corrosion process within the two types may be treated in similar manners [14]. The model divides the service life of corroding concrete into two stages: (1) initiation; and (2) propagation. The initiation stage constitutes the time required for chlorides to penetrate to the strand, at which time corrosion onsets and the propagation stage begins. The propagation stage is associated with the accumulation of corrosion products and the resulting corrosion-induced cracking of concrete. The end of the propagation stage is based on the definition of service life, which is usually taken as the point when surface cracking emerges in the concrete [15, 16].

Schematics of four major points in the corrosion process are shown in Fig. 1.3. The first shows an arbitrary point during the initiation stage in Fig. 1.3(a), where chlorides are penetrating through the concrete cover but have not yet reached the strand. There is therefore no corrosion taking place during this stage. The end of the initiation stage is shown in Fig. 1.3(b), where chlorides have reached the strand. At this point, the chlorides begin to break down the passive layer surrounding the strand [17], thus depassivating it and increasing the corrosion susceptibility. Compared to reinforcing bars, the stronger passive layer surrounding strands (due to their smoother

surface) makes the chloride breakdown more difficult and results in localized (pitting) corrosion at various locations on the strand surface [18]. Pitting corrosion has therefore been one of the corrosion mechanisms most strongly associated with structural collapse [18]. Between corrosion onset and concrete crack initiation, corrosion products accumulate in the thin ($\approx$ 10 μm thick) porous interface between the strand and the concrete [19, 20]. This accumulation produces pressure within the interface, since the corrosion products occupy a larger volume than the consumed steel. Once the porous interface is saturated with corrosion products, pressure due to corrosion buildup can increase beyond the capacity of the concrete cover. The point at which a critical pressure is reached may be seen in Fig. 1.3(c), resulting in crack initiation toward the nearest free surface (*i.e.*, through the cover). With further corrosion buildup, the crack may propagate until it reaches the surface, marking the end of service life, as shown in Fig. 1.3(d). For a 5 cm (2 in.) cover, for example, such surface cracking can be caused by as little as 4-6% mass loss in the strand [21]. In addition, the surface cracking can raise the corrosion rate due to the freer penetration of aggressive agents [15]. This makes the corrosion susceptibility of strands in cover-cracked concrete significantly greater than otherwise. Lastly, the cover-cracking point is also structurally important in terms of diminishing steel-concrete bond strength [13].

2 Methods of Corrosion Inspection

2.1 Established methods

The financial, safety, and resource implications of unidentified corrosion have motivated a number of inspection methods for detecting this particular damage mechanism. The most traditional and prevalent is perhaps visual inspection, through the use of experienced inspectors. However, this method is only able to detect corrosion when its effects are apparent from the exterior of a structure. Naturally, this limits

its ability to identify corrosion before it becomes severe. Other inspection methods may be distinguished based on their application to reinforced/prestressed concrete or strands alone.

For strands, the penetration method is a relatively simple approach to gathering information about load-carrying capacity [22, 23]. Here, an inspector attempts to pry apart individual wires of a strand to evaluate potential stress losses or broken wires. However, the method only gathers qualitative information and is usually semi-destructive in gaining access to a region of the strand. One example of a more recent and sophisticated approach for concrete is the half-cell potential method [24], in which electrochemical measurements are taken and converted to corrosion probabilities. However, this method relies on physical access to the embedded strand, which may also involve semi-destructive aspects.

2.2 Structural health monitoring

Currently, if any of the above inspection methods are implemented, they are done so on a periodic time-based schedule. Under this framework, it is oftentimes the case that inspections are performed only to reveal a "no corrosion" or "healthy" condition. Resources are therefore often wasted in inspecting healthy structures.

This reality has motivated the transition from a time-based to a condition-based paradigm. The goal is to allow maintenance to be performed only when necessary, as dictated by the condition of the structure. Structural health monitoring (SHM) is one of the primary means to achieve this paradigm. Through networks of sensors performing nondestructive evaluation, SHM aims for continuous automated monitoring of structural condition, including such mechanisms as corrosion. Acoustic-based methods are some of the most promising in this area due to the rich corrosion-sensitive characteristics of wave propagation in structures and the versatility of their implementation.

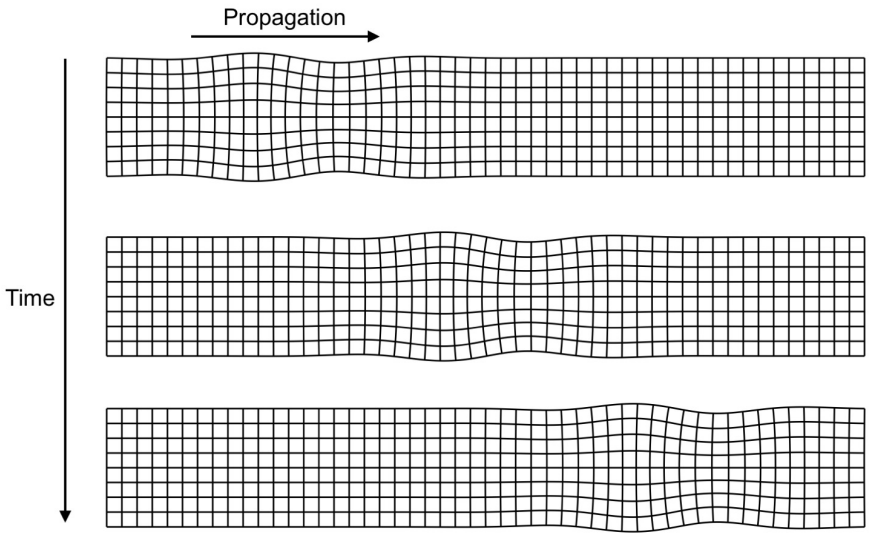

Fig. 1.4 Illustration of a guided wave propagating along the axis of a rod (side view).

3 Acoustic Methods for Corrosion Monitoring

Acoustic-based SHM methods come in two forms: *active* and *passive*. The active form is considered here in terms of guided wave (GWs), while the passive form is considered in terms of acoustic emission (AE), with each described below. Both the generation and reception of acoustic waves may be achieved through contact piezoelectric transducers. These allow conversion of (mechanical) acoustic waves to electrical signals, which may then be digitized for storage and analysis.

3.1 Guided waves

An acoustic wave is termed a GW when its propagation is guided by the bounded geometry of a structure. An example is shown in Fig. 1.4 for a GW propagating along a rod. The wave is bounded in the lateral directions and therefore only propagates along the axis of the rod. This behavior differentiates such waves from those propagating in a boundless medium, termed bulk waves. Due to the fact that they are guided by the medium (or structure), GWs are highly sensitive to the structural geometry and any changes that occur within it.

The initial attraction of GWs for SHM came from their potential for damage monitoring through geometric sensitivities. This includes damage mechanisms such as corrosion-induced material loss [10] and debonding [25]. However, with the valuable structural information potentially gained by monitoring the stress state in strands, researchers looked into the use of GWs to probe this information as well.

3.1.1 Guided-wave-based stress monitoring

The first study revealing the stress-dependent nature of GWs in strands was perhaps that of Kwun, *et al.* [26] in 1998. They experimentally discovered missing frequency content (termed the *notch frequency*), which was due to applied stress in the strand. In particular, a linear relation was empirically found between the notch frequency in the fundamental low-frequency GW mode and the logarithm of stress. The fact that this relationship is monotonic provided a strong motivation for its use in stress monitoring, since a given notch frequency could be uniquely associated with a given stress level. Interestingly, an explanation for the cause of the notch frequency eluded researchers for roughly 20 years. Later, in 2016 Treyssède [27] used numerical simulations to deduce that a stress-dependent interwire contact area explained the notch frequency. The interwire contact area increases with increasing tensile stress; this causes the strand to gradually behave more and more like a single cohesive rod, as opposed to a bundle of wires interacting with each other. Recently, Liu [28] derived a stress monitoring technique based on the notch frequency. Their technique was validated in three types of pristine multiwire strands.

In parallel with notch-frequency investigations were studies on the stress dependence of GW velocity (termed acoustoelasticity). These similarly focused on the fundamental GW mode. Some studies were empirical, and discovered linear relations for certain regions of high stress ($> 50\%$ ultimate tensile strength, or UTS) [29, 30]. Interestingly, strongly nonlinear and non-monotonic stress dependence was observed for lower stress levels ($< 35\%$ UTS). Other researchers proposed approximate theo-

retical analyses for the effect of stress [31–33]. Assuming that a GW generated in a strand wire propagates as in a rod, the theories consisted of a modified version of the Pochhammer-Chree equation [34, 35] governing GWs in an unstressed rod. The slope of the stress dependence was shown to be similar to the theoretical slope at high stress levels ($> 50\%$ UTS) [33].

Aside from frequency- and acoustoelastic-based approaches, there have been a number of other related works on the fundamental mode. Collectively, these may be classified into energy-based approaches. For example, studies have been made on the stress-dependent transmission of energy within [36] and between [37] strand wires. Others concerned the stress-dependent generation of higher harmonics [38, 39].

3.1.2 Summary of approaches

The above review suggests that three types of approaches exist for acoustic-based stress monitoring in strands: (1) acoustoelastic-based; (2) frequency-based; and (3) energy-based.

Arguments may be made for the advantage of acoustoelasticity over frequency- and energy-based approaches. First, the notch frequency is known to be susceptible to geometric effects such as corrosion-induced surface roughness [40]. The presence of two phenomena both linked to the notch frequency may make quantification of a single one (such as stress) challenging. Second, since energy-based methods use absolute measurements of energy, factors like transducer bond weakening or transducer replacement can contaminate the results. This is in addition to confounding attenuation effects, such as from evolving surface roughness under corrosion.

It should be noted that acoustoelasticity is not immune to confounding effects. For instance, the fundamental mode which has been targeted in the literature is sensitive to geometrical corrosion effects, such as cross-section reduction. In addition, its velocity exhibits a non-monotonic stress-dependence, yielding ambiguity when translating stress to velocity. However, acoustoelasticity may perhaps be the most flexible

approach toward circumventing these issues. For instance, since acoustoelasticity is not restricted to a particular GW mode, it may be possible to identify specific modes which limit or remove these confounding effects. This thesis is therefore interested in whether the confounding effects of corrosion on acoustoelasticity can be minimized (and possibly made sufficiently small) through an appropriate simplification of the generated GWs.

3.2 Acoustic emission

Acoustic emission is the idea of gathering information about damage evolution by continuously "listening" to the sudden releases of energy due to such damage. Acoustic energy can be generated from a variety of sources, including pitting [41], crack propagation [42], friction between crack faces [43], and plastic deformation [44], to name a few. The continuous aspect of AE allows for large amounts of data to be collected, from which a wealth of information may be strategically extracted.

Two main approaches to analyzing AE may be adopted. The first, termed *feature-based* AE, is to extract a number of features from AE waveforms, and then disregard the waveforms themselves. This can be thought of as a simple form of dimension reduction on the AE data, where each digital waveform has a compressed representation in terms of a handful of features. Subsequent analysis of AE is then carried out on the features, which has the advantage of lessening the computational expense. The second approach is to directly analyze the AE waveforms themselves, termed *waveform-based* AE. This approach only recently became feasible, with the advent of sufficient computational power. However, it can still prove infeasible in the event of large amounts of AE being rapidly generated. This thesis focuses on the feature-based approach, since the lower computational burden is more amenable to real-time analysis. In addition, it has an established history in the analysis of corrosion-induced AE in concrete.

In the context of AE, this thesis is specifically focused on its application to corro-

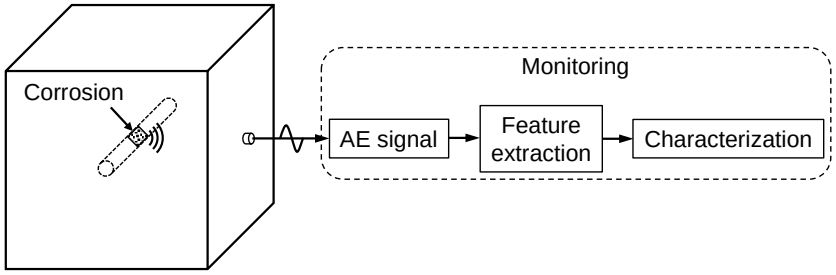

Fig. 1.5 Illustration of acoustic emission process for corrosion monitoring in prestressed concrete.

sion monitoring in prestressed concrete. The more complex nature of corrosion in the coupled strand-concrete system of prestressed concrete lends itself to the complexity of information that is potentially able to be gained through AE. In addition, strands embedded in prestressed concrete may be difficult to access directly for GW generation. Instead, AE has the potential to remotely monitor corrosion from the exterior concrete surface. A schematic of AE monitoring applied to a prestressed concrete element may be seen in Fig. 1.5.

3.2.1 Corrosion-induced acoustic emission in prestressed concrete

A wide range of AE studies have been performed toward evaluating corrosion in prestressed and reinforced concrete. These have largely used feature-based AE, with most considering features related to AE activity and frequency content. Here, AE activity may denote the amount of energy or number of waveforms generated, for instance, while frequency content may denote the peak frequency in a waveform.

In early work on the subject, numerous researchers found that the onset of corrosion produces an initial spike in AE activity [17, 45–49]. This was confirmed by Austin, *et al.* [17] by breaking open specimens before and after the first activity spike. For those specimens opened before such time, visual inspections found that the steel surface remained pristine. However, early-stage corrosion pits were found in the specimens which had been opened after the initial activity spike. This feature was also found to indicate concrete cracking due to corrosion buildup, which results in additional activity spikes [42, 50]. Dunn, *et al.* [42] posited that such spikes occur

in succession, due to the cyclic nature of corrosion buildup, pressure increase, and crack propagation. Other researchers have found the overall trends in AE activity to be correlated with the extent of corrosion [51–53].

On the other hand, from work on prestressing strands [41, 54] and reinforced concrete [55], it has also been demonstrated that different corrosion mechanisms produce AE with different frequency content. The peak frequency feature in particular has been shown to distinguish a number of corrosion mechanisms, including corrosion onset and steel pitting. Di Benedetti, *et al.* [55] showed that corrosion onset produces frequency content near 35-90 kHz. They suggested that content outside this range may be due to saltwater infiltration into the concrete pores. Li, *et al.* [54] suggested that pitting in the strand produces frequency content near 120-160 kHz. This was in accordance with earlier work by Ramadan, *et al.* [41], who observed pitting phenomena near 140 kHz. On the whole, these works illustrate that studying frequency content in addition to AE activity can provide enhanced corrosion information.

3.2.2 Summary of approaches

From a diagnostic and prognostic perspective, the points of corrosion onset and corrosion-induced concrete cracking are two of the most important to determine. Corrosion onset marks the start of both time-to-cracking and pit-depth distribution models, while concrete cracking is recognized as a service-life limit state due to decreased steel-concrete bond strength and increased ingress of corroding agents. AE activity and frequency content are widely used in laboratory testing to determine these points. However, it is possible to foresee issues in transitioning to field applications. Although valuable in laboratory settings, the real-world reliability of activity features is questionable due to contamination from extraneous sources of acoustic activity. It would therefore be useful to glean additional corrosion indicators from the wealth of collected AE data. Fortunately, such large collections of data bring about the possibility of gathering new types of information about corrosion. This includes

the shape (*i.e.*, topology) of an AE datacloud itself.

During the last two decades, topological data analysis (TDA) has emerged as a quantitative computational method for studying the topology of dataclouds [56]. It is a form of data science based on algebraic topology, and has seen a broad range of noteworthy applications, including time series analysis [57], classification of breast cancer subtypes [58], aviation data analytics [59], and natural image statistics [56]. Through TDA, it has been demonstrated that meaningful information can be embedded in a datacloud's topology. However, to the best of the author's knowledge, no prior studies have been carried out on applying TDA within AE, let alone within a SHM framework. This thesis is therefore interested in whether topological characteristics of AE data are linked to corrosion in prestressed concrete structures.

4 Overview

4.1 Research statement

Corrosion monitoring methods based on acoustic wave propagation possess unique advantages due to their high sensitivities and versatility between active and passive modalities. Such high sensitivities, however, also pose a challenge. Accounting for extraneous sensitivities is one of the forefront missions within the broad field of SHM [60]. Ignoring certain factors, for instance, can lead to false positives in damage detection and biased metrics of structural health.

With the wealth information embedded in acoustic waveforms, there is a need of either simplifying the waveforms collected, or developing tools to effectively sift through the data. This thesis investigates each of these two approaches within specific case studies of corrosion. The overall form of the research statement for this thesis is then the following:

Harnessing complexities in acoustic data can enhance corrosion monitoring.

This form can be divided into two alternate approaches: on the one hand, simplifying complexities in acoustic data to target desired corrosion information; on the other hand, understanding complexities to gather new insights for monitoring corrosion. The two approaches form the basis of the research investigated in this thesis. The first is applied to GWs and the second to AE, stated as follows:

1. *Simplifying GW generation for active acoustic monitoring can address complex data by targeting specific corrosion phenomena.*

2. *Understanding the topology of complex AE data in passive acoustic monitoring can reveal underlying corrosion information.*

In both cases, there is a need to appropriately handle the complex information once it is broken down. For this reason, several data processing techniques are proposed and adapted to effectively automate the monitoring process.

4.2 Research objective

First, the simplifying approach is taken for active GW-based corrosion monitoring of strands. Specifically, the monitoring of corrosion-induced stress redistribution is investigated. This approach is a natural fit for active methods since wave generation and reception are under control, thus allowing them to be tailored toward a certain cause. For this purpose, acoustoelasticity is advanced within the context of beneficial GW modes which can target stress while minimizing confounding geometric effects. Various methods of data processing are incorporated to enhance the results for longterm monitoring scenarios. This includes the wavelet transform, modal modulation, and data fusion. An accelerated corrosion test is then designed to experimentally validate the use of GWs for continuous stress monitoring in a corroding strand.

Second, in an application to prestressed concrete, tools are adapted to extract and understand meaningful corrosion information from passively monitored AE data.

With the lack of control over wave generation in passive methods, the related complexities arising in the data need to be intelligently sifted through. The use of TDA is a main focus, under the proposition that corrosion information is embedded in the topology of AE data. An additional level of data processing based on hidden Markov modeling is then used to probabilistically combine traditional and topological indicators for automated corrosion diagnostics. Accordingly, two accelerated corrosion tests are carried out on prestressed concrete specimens to first understand the data and then evaluate and generalize that understanding.

The work presented in this thesis was mainly established through the author's following published studies [61–67]:

- B. Dubuc, A. Ebrahimkhanlou, and S. Salamone, "Higher order longitudinal guided wave modes in axially stressed seven-wire strands," *Ultrasonics*, vol. 84, pp. 382-391, 2018.*
- B. Dubuc, A. Ebrahimkhanlou, and S. Salamone, "Stress measurement in seven-wire strands using higher order guided ultrasonic wave modes," *Transp. Res. Rec.*, vol. 2672, no. 41, pp. 123-131, 2018.†
- B. Dubuc, A. Ebrahimkhanlou, and S. Salamone, "A spectral method for computing guided waves in stressed plates and rods," *Health Monitoring of Structural and Biological Systems*, vol. 10600, p. 106001Z, SPIE, 2018.‡
- B. Dubuc, A. Ebrahimkhanlou, and S. Salamone, "Corrosion monitoring of prestressed concrete structures by using topological analysis of acoustic emission data," *Smart Mater. Struct.*, vol. 28, no. 5, p. 055001, 2019.§

* According to the publisher's website (`https://www.elsevier.com` accessed on February 19, 2020) inclusion of articles in full or in part in a research dissertation is permitted.

† According to the publisher's website (`https://us.sagepub.com` accessed on February 19, 2020) inclusion of articles in a research dissertation is permitted.

‡ Written permission from the Society of Photo-Optical Instrumentation Engineers on March 19, 2020 verified the inclusion in whole or in part of proceedings in a research dissertation.

§ According to the publisher's website (`https://publishingsupport.iopscience.iop.org` accessed on February 19, 2020) inclusion of articles in a research dissertation is permitted.

- B. Dubuc, A. Ebrahimkhanlou, and S. Salamone, "Data fusion approach for characterization of corrosion-induced stress change in prestressing strands using modulated higher-order guided ultrasonic waves," *Health Monitoring of Structural and Biological Systems*, vol. 10972, p. 109721D, SPIE, 2019.‡

- B. Dubuc, A. Ebrahimkhanlou, and S. Salamone, "Stress monitoring of prestressing strands in corrosive environments using modulated higher-order guided ultrasonic waves," *Struct. Health Monit.*, vol. 19, no. 1, pp. 202-214, 2020.†

- B. Dubuc, A. Ebrahimkhanlou, K. Sitaropoulos, and S. Salamone, "Topological-based acoustic emission data analysis for passive corrosion monitoring in prestressed concrete structures," *Health Monitoring of Structural and Biological Systems*, vol. 11381, p. 113811T, SPIE, 2020.‡

The author of this dissertation was the lead author of the above papers, devising the theory and methodology, conducting the experiments, and performing data analyses.

CHAPTER 2

Acoustoelasticity

This chapter* lays the foundation of the elastodynamics and acoustoelastic theory used throughout this thesis. The theory is based on Green and Zerna [68] and Suhubi [69], from which the author's own advancements are then made. It is first formulated in terms of an arbitrary curvilinear coordinate system for wave motion superposed on a finite predeformation in an isotropic hyperelastic body. Special cases are then detailed for cartesian and cylindrical coordinates, which allow applications to bulk waves in unbounded bodies and guided waves (GWs) in rods.

Consider a body which is initially undeformed, referred to as the body $\mathscr{A}$. Due to some static finite predeformation, the body is transformed to the predeformed body $\mathscr{B}$. Small-amplitude wave motion is then superposed on the predeformed body, yielding the deformed body $\mathscr{C}$. The terms *undeformed*, *predeformed*, and *deformed* are used to describe quantities related to these three bodies, respectively. Let the position vectors for a material point in the undeformed, predeformed, and deformed bodies be denoted $\mathbf{r}$, $\mathbf{R}$, and $\mathbf{R}+\epsilon\mathbf{R}'$. The point is mapped from the undeformed to the predeformed body according to the displacement $\mathbf{u}$, so that $\mathbf{R}=\mathbf{r}+\mathbf{u}$. Similarly, the point is then mapped from the predeformed to the deformed body according to a small displacement $\epsilon\mathbf{u}'$, so that $\mathbf{R}+\epsilon\mathbf{R}'=\mathbf{R}+\epsilon\mathbf{u}'$. The smallness is imposed by retaining only linear terms in the small quantity ϵ. These deformations are illustrated in Fig. 2.1.

* This chapter is derived in part from the author's work in [62, 63].

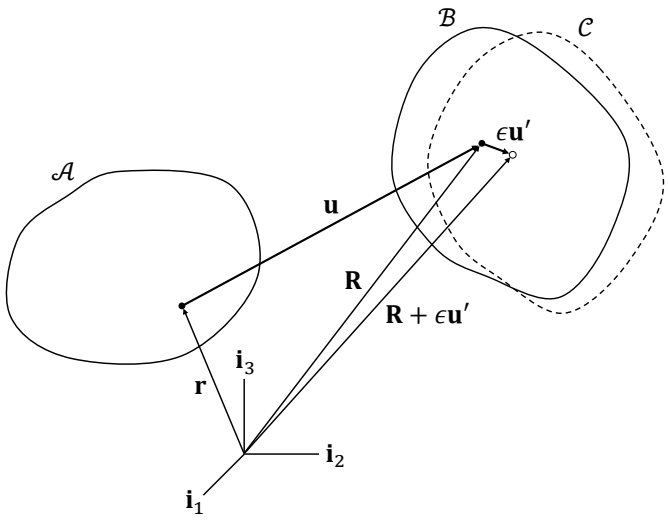

Fig. 2.1 Deformation sequence of a body from $\mathscr{A}$: undeformed, to $\mathscr{B}$: predeformed, to $\mathscr{C}$: deformed. Position vectors and displacements of an arbitrary point indicated. Origin indicated by cartesian basis vectors.

5 Predeformation

This section analyzes the predeformation stage introduced above, where the body $\mathscr{A}$ is transformed to $\mathscr{B}$. It considers the strain and stress associated with a finite predeformation and their connection through a constitutive relation. In addition, the equation of motion is outlined, along with the special case of a static predeformation.

5.1 Strain

Strain is a measure of geometrical change due to the deformation of a body. Following the convention of [68], strain describes this change by comparing the squared length of small (differential) line segments within the body before and after deformation.

In order to analyze such line segments, let a differential segment $\mathrm{d}\mathbf{r}$ be located at the position $\mathbf{r}$ in the undeformed body $\mathscr{A}$. The differential segment may be expressed in terms of cartesian coordinates x^i as

$$\mathrm{d}\mathbf{r} = \mathrm{d}x^1\mathbf{i}_1 + \mathrm{d}x^2\mathbf{i}_2 + \mathrm{d}x^3\mathbf{i}_3 = \mathrm{d}x^i\mathbf{i}_i \tag{2.1}$$

where $\mathbf{i}_i$ are the cartesian basis vectors, and the summation convention over repeated indices is implied from here onward. To add necessary generality, the segment may also be expressed in terms of curvilinear coordinates θ^i and a set of curvilinear basis vectors $\mathbf{g}_i$ (to be determined) as

$$\mathrm{d}\mathbf{r} = \mathrm{d}\theta^i \mathbf{g}_i \tag{2.2}$$

Analyzing the differential segment using the chain rule, it may be found that the curvilinear basis vectors are related to the cartesian basis vectors as follows:

$$\mathbf{g}_i = \frac{\partial x^j}{\partial \theta^i}\mathbf{i}_j = \frac{\partial \mathbf{r}}{\partial \theta^i} \tag{2.3}$$

Unlike the cartesian basis vectors, the curvilinear basis vectors may not have unit length, may not be dimensionless, and may vary in space.

For notational simplicity, derivatives with respect to the components θ^i will from here onward be expressed using indicial notation. In particular, a comma before a subscript indicates partial differentiation with respect to that component,

$$\frac{\partial \cdot}{\partial \theta^i} = \cdot_{,i} \tag{2.4}$$

It should be noted that this only applies to differentiation with respect to θ^i. For differentiation with respect to other variables, the full form is explicitly written (*e.g.*, $\partial \cdot / \partial x^i$). In this way, the curvilinear basis vectors may be written more simply as $\mathbf{g}_i = \mathbf{r}_{,i}$.

For curvilinear components, it is important to distinguish between *contravariant* components θ^i and *covariant* components θ_i. Here, a superscript indicates a contravariant component, while a subscript indicates a covariant component. To illustrate the difference, the differential segment $\mathrm{d}\mathbf{r}$ may be expressed in either of two ways: (1) using contravariant components and covariant basis vectors, *i.e.*, $\mathrm{d}\mathbf{r} = \mathrm{d}\theta^i \mathbf{g}_i$;

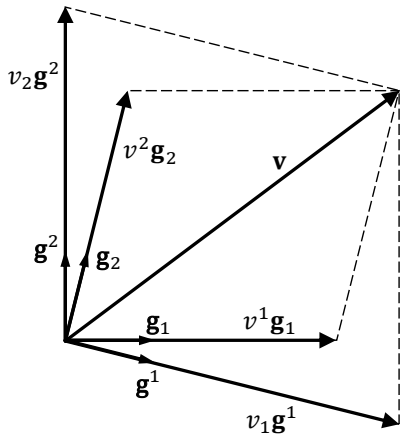

Fig. 2.2 Representation of an arbitrary vector $\mathbf{v}$ in terms of covariant $\mathbf{g}_i$ and contravariant $\mathbf{g}^i$ basis vectors.

or (2) using covariant components and contravariant basis vectors, *i.e.*, $\mathrm{d}\mathbf{r} = \mathrm{d}\theta_i \mathbf{g}^i$. Naturally, the same may be done with cartesian coordinates, $\mathrm{d}\mathbf{r} = \mathrm{d}x^i \mathbf{i}_i = \mathrm{d}x_i \mathbf{i}^i$, although for this special case there is no difference between the two.

Since covariant and contravariant components are intimately linked, it is useful to consider both for the curvilinear case. In particular, the contravariant basis vectors $\mathbf{g}^i$ are defined to be orthogonal the covariant basis vectors $\mathbf{g}_i$ in the following manner:

$$\mathbf{g}_i \cdot \mathbf{g}^j = \delta_i^j \tag{2.5}$$

where "$\cdot$" denotes the dot product, and $\delta_i^j = \delta_{ij} = \delta^{ij}$ is the Kronecker delta. From Eq. (2.3), the contravariant basis vectors are then

$$\mathbf{g}^i = \frac{\partial \theta^i}{\partial x^j} \mathbf{i}^j \tag{2.6}$$

The representation of a vector in terms of covariant and contravariant basis vectors is illustrated in Fig. 2.2. Here, the orthogonality between the two sets of basis vectors may also be seen.

The squared length of the differential segment $\mathrm{d}\mathbf{r}$ may now be written in terms of the curvilinear components as

$$\mathrm{d}\mathbf{r} \cdot \mathrm{d}\mathbf{r} = g_{ij}\mathrm{d}\theta^i \mathrm{d}\theta^j \tag{2.7}$$

where g_{ij} is the covariant metric tensor for the curvilinear coordinates, defined by

$$g_{ij} = \mathbf{g}_i \cdot \mathbf{g}_j = \frac{\partial x^k}{\partial \theta^i}\frac{\partial x^k}{\partial \theta^j} \tag{2.8}$$

Using the definitions of the basis vectors, an additional metric tensor may also be formed. In particular, the contravariant metric tensor g^{ij} is

$$g^{ij} = \mathbf{g}^i \cdot \mathbf{g}^j = \frac{\partial \theta^i}{\partial x^k}\frac{\partial \theta^j}{\partial x^k} \tag{2.9}$$

satisfying the property that $g^{ik}g_{kj} = \delta^i_j$. The contravariant metric tensor may be used to express the squared length in terms of covariant components as $\mathrm{d}\mathbf{r} \cdot \mathrm{d}\mathbf{r} = g^{ij}\mathrm{d}\theta_i \mathrm{d}\theta_j$

When the undeformed body $\mathscr{A}$ is deformed into the predeformed body $\mathscr{B}$, the differential line segment $\mathrm{d}\mathbf{r}$ located at $\mathbf{r}$ is transformed to the segment $\mathrm{d}\mathbf{R}$, located at $\mathbf{R}$. Following the same process that was carried out for the undeformed body, the differential segment in the predeformed body may be expressed in terms of the curvilinear components θ^i as

$$\mathrm{d}\mathbf{R} = \mathrm{d}\theta^i \mathbf{G}_i \tag{2.10}$$

where $\mathbf{G}_i$ are the covariant basis vectors for the deformed body, defined as

$$\mathbf{G}_i = \mathbf{R}_{,i} \tag{2.11}$$

Comparing Eqs. (2.2) and (2.10), it may be seen that the components $\mathrm{d}\theta^i$ of the differential segment do not change, although its position, length, and orientation may. Instead of these changes being captured through the components, they are captured through the basis vectors $\mathbf{g}_i$ and $\mathbf{G}_i$.

Similar to the undeformed body, contravariant basis vectors for the predeformed body may be defined from $\mathbf{G}_i \cdot \mathbf{G}^j = \delta_i^j$, yielding

$$\mathbf{G}^i = \frac{\partial \theta^i}{\partial X^j} \mathbf{i}_j \tag{2.12}$$

In terms of the curvilinear components, the squared length of the deformed line segment is then

$$\mathrm{d}\mathbf{R} \cdot \mathrm{d}\mathbf{R} = G_{ij} \mathrm{d}\theta^i \mathrm{d}\theta^j \tag{2.13}$$

which may also be written in terms of a contravariant metric tensor as $G^{ij}\mathrm{d}\theta_i \mathrm{d}\theta_j$. Covariant and contravariant metric tensors for the deformed body may then be defined, respectively, as

$$\begin{aligned} G_{ij} &= \mathbf{G}_i \cdot \mathbf{G}_j = \frac{\partial X^k}{\partial \theta^i} \frac{\partial X^k}{\partial \theta^j} \\ G^{ij} &= \mathbf{G}^i \cdot \mathbf{G}^j = \frac{\partial \theta^i}{\partial X^k} \frac{\partial \theta^j}{\partial X^k} \end{aligned} \tag{2.14}$$

Analogous to the undeformed body, it may be seen that these satisfy $G^{ik}G_{kj} = \delta_j^i$.

The strain tensor e_{ij} may now be introduced to describe the squared length change due to the predeformation as [68]

$$\mathrm{d}\mathbf{R} \cdot \mathrm{d}\mathbf{R} - \mathrm{d}\mathbf{r} \cdot \mathrm{d}\mathbf{r} = 2e_{ij} \mathrm{d}\theta^i \mathrm{d}\theta^j \tag{2.15}$$

where the covariant strain tensor e_{ij} is perhaps the most natural to use [70], and is defined from the above as

$$e_{ij} = \tfrac{1}{2}(G_{ij} - g_{ij}) \tag{2.16}$$

Furthermore, since this is the form used predominantly in this thesis, it will also be referred to simply as the *strain tensor*. Aside from the above expression in terms of

metric tensors, the strain tensor may also be written in terms of displacement. As seen in Fig. 2.1 the displacement vector for the predeformation is defined as

$$\mathbf{u} = \mathbf{R} - \mathbf{r} \tag{2.17}$$

Incorporating the above and following the definition of the metric tensors, the strain tensor may be written as

$$e_{ij} = \tfrac{1}{2}(\mathbf{g}_i \cdot \mathbf{u}_{,j} + \mathbf{g}_j \cdot \mathbf{u}_{,i} + \mathbf{u}_{,i} \cdot \mathbf{u}_{,j}) \tag{2.18}$$

To simplify the above, the displacement may be referenced to the undeformed body using either contravariant or covariant components as $\mathbf{u} = u^i \mathbf{g}_i$ or $u_i \mathbf{g}^i$. Moreover, the derivative of the displacement (or any other vector) may similarly be expressed in one of two ways,

$$\mathbf{u}_{,i} = u_j|_i \mathbf{g}^j = u^k|_i \mathbf{g}_k \tag{2.19}$$

where $\cdot|_i$ denotes covariant differentiation with respect to the undeformed body. Covariant differentiation accounts for the spatial variation of the curvilinear basis vectors. This is realized through the use of the Christoffel symbols γ_{ij}^k. For the undeformed body, in particular, the covariant derivative of the covariant components of a vector is

$$u_j|_i = u_{j,i} - \gamma_{ji}^k u_k \tag{2.20}$$

while the covariant derivative of the contravariant components of a vector is

$$u^j|_i = u^j_{,i} + \gamma_{ki}^j u^k \tag{2.21}$$

The Christoffel symbols may be expressed in terms of the metric tensor for the undeformed body as

$$\gamma_{ij}^{k} = \tfrac{1}{2} g^{kl}(g_{il,j} + g_{jl,i} - g_{ij,l}) \tag{2.22}$$

Appendix A.1. may be referenced for more information on Christoffel symbols. These multiple ways of expressing the derivative may be inserted strategically into Eq. (2.18) in order to exploit the relation $\mathbf{g}_i \cdot \mathbf{g}^j = \delta_i^j$. This yields†

$$e_{ij} = \tfrac{1}{2}(u_i|_j + u_j|_i + u^k|_i u_k|_j) \tag{2.25}$$

In an analogous way, the displacement may also be expressed in terms of the basis vectors for the predeformed body using either contravariant or covariant components, $\mathbf{u} = U^i \mathbf{G}_i$ or $U_i \mathbf{G}^i$. Additionally, the relation $\mathbf{g}_i = \mathbf{G}_i - \mathbf{u}_{,i}$ may be used to obtain the strain tensor referenced to the predeformed body,‡

$$e_{ij} = \tfrac{1}{2}(U_i||_j + U_j||_i - U^k||_i U_k||_j) \tag{2.28}$$

† To illustrate this strain tensor, let the curvilinear coordinates θ^i be the cartesian coordinates $x^i = x_i$ for the undeformed body. The Christoffel symbols then vanish and the strain tensor becomes the Lagrangian strain tensor (with $u^i = u_i$),

$$e_{ij} = \frac{1}{2}\left(\frac{\partial u_i}{\partial x_j} + \frac{\partial u_j}{\partial x_i} + \frac{\partial u_k}{\partial x_i}\frac{\partial u_k}{\partial x_j}\right) \tag{2.23}$$

In this case, the strain tensor then describes the squared length change as

$$\mathrm{d}\mathbf{R} \cdot \mathrm{d}\mathbf{R} - \mathrm{d}\mathbf{r} \cdot \mathrm{d}\mathbf{r} = 2e_{ij}\mathrm{d}x_i \mathrm{d}x_j \tag{2.24}$$

‡ To illustrate this strain tensor, let the curvilinear coordinates θ^i be the cartesian coordinates $X^i = X_i$ for the predeformed body. The strain tensor then becomes the Eulerian strain tensor (with $U^i = U_i$),

$$e_{ij} = \frac{1}{2}\left(\frac{\partial U_i}{\partial X_j} + \frac{\partial U_j}{\partial X_i} - \frac{\partial U_k}{\partial X_i}\frac{\partial U_k}{\partial X_j}\right) \tag{2.26}$$

In this case, the strain tensor then describes the squared length change as

$$\mathrm{d}\mathbf{R} \cdot \mathrm{d}\mathbf{R} - \mathrm{d}\mathbf{r} \cdot \mathrm{d}\mathbf{r} = 2e_{ij}\mathrm{d}X_i \mathrm{d}X_j \tag{2.27}$$

The strain tensor therefore naturally becomes either the Lagrangian or the Eulerian strain tensor, depending on whether the curvilinear coordinates are referenced to either the undeformed or the deformed body.

where $\cdot||_i$ denotes covariant differentiation with respect to the predeformed body. This is analogous to covariant differentiation for the undeformed body, where Christoffel symbols Γ^k_{ij} associated with the predeformed body are used instead,

$$\begin{aligned} U_j||_i &= U_{j,i} - \Gamma^k_{ji} U_k \\ U^j||_i &= U^j_{,i} + \Gamma^j_{ki} U^k \end{aligned} \tag{2.29}$$

The Christoffel symbols for the predeformed body may be expressed in terms of the metric tensors for that body as

$$\Gamma^k_{ij} = \tfrac{1}{2} G^{kl}(G_{il,j} + G_{jl,i} - G_{ij,l}) \tag{2.30}$$

5.1.1 Strain invariants

The covariant strain tensor is not the only one that will be of use in this thesis. For instance, the *mixed* strain tensor e^i_j is useful for constructing strain invariants. The term mixed implies that the tensor has a mix of covariant and contravariant indices. The mixed strain tensor may be formed by raising one of the indices on e_{ij},

$$e^i_j = g^{ik} e_{kj} = \tfrac{1}{2}(g^{ik} G_{kj} - \delta^i_j) \tag{2.31}$$

Although either one of the metric tensors g^{ij} or G^{ij} may be used for the purpose of raising indices on the strain tensor, the metric tensor for the undeformed body is chosen here following convention [68]. Appendix A.2. may be referenced for more information about raising indices on tensors. It is convenient to construct strain invariants from the mixed strain tensor e^i_j, since the components of this strain tensor are dimensionless in any coordinate system (unlike the covariant strain tensor). In particular, invariants may be constructed from the characteristic equation of the mixed strain tensor,

$$\det\{e^i_j + \Lambda\delta^i_j\} = \Lambda^3 + I\Lambda^2 + II\Lambda + III \tag{2.32}$$

where $\det\{\cdot\}$ denotes the determinant, and the coefficients I, II, III are strain invariants, defined

$$\begin{aligned} I &= e^i_i \\ II &= \tfrac{1}{2}(I^2 - e^i_j e^j_i) \\ III &= \det\{e^i_j\} \end{aligned} \tag{2.33}$$

It may be seen that these invariants are purely terms of first-, second-, and third-order in strain, respectively.

Aside from those defined above, there are other useful invariants that may be derived from the mixed strain tensor. In particular, the definition of the mixed strain tensor may be rearranged to express a new tensor $g^{ik}G_{kj}$, whose components are linear combinations of the mixed strain components. Additional strain invariants I_1, I_2, I_3 may then be derived from the characteristic equation for $g^{ik}G_{kj}$,

$$\det\{g^{ik}G_{kj} + \Lambda\delta^i_j\} = \Lambda^3 + I_1\Lambda^2 + I_2\Lambda + I_3 \tag{2.34}$$

where

$$\begin{aligned} I_1 &= g^{ij}G_{ji} \\ I_2 &= \tfrac{1}{2}(I_1^2 - g^{ik}g^{jl}G_{ij}G_{kl}) \\ I_3 &= \det\{g^{ik}G_{kj}\} = G/g \end{aligned} \tag{2.35}$$

Here, g and G are the determinants of the metric tensors g_{ij} and G_{ij}, respectively. It may be seen that these strain invariants include terms up to first-, second-, and third-order in strain, respectively. Also, it may be noted that the third invariant I_3

is closely related to the volume change due to predeformation (*i.e.*, the dilatation δ) as follows [68, p.149]:

$$\sqrt{I_3} = 1 + \delta \tag{2.36}$$

In order to compare the two sets of strain invariants, those expressed in Eq. (2.35) may be equivalently written in terms of the mixed strain tensor as

$$\begin{aligned} I_1 &= 3 + 2e_i^i \\ I_2 &= 3 + 4e_i^i + 2(e_i^i e_j^j - e_j^i e_i^j) \\ I_3 &= \det\{\delta_j^i + 2e_j^i\} \end{aligned} \tag{2.37}$$

It may then be seen that the above strain invariants are related to I, II, III as

$$I_1 = 3 + 2I \qquad I_2 = 3 + 4I + 4II \qquad I_3 = 1 + 2I + 4II + 8III \tag{2.38}$$

while the inverse relations of the above may be found as

$$I = \tfrac{1}{2}(I_1 - 3) \qquad II = \tfrac{1}{4}(I_2 - 2I_1 + 3) \qquad III = \tfrac{1}{8}(I_3 - I_2 + I_1 - 1) \tag{2.39}$$

5.2 Stress and the equation of motion

Stress describes the force acting over a given surface in a body. To describe the stress localized at a given point on a surface, define the stress vector $\mathbf{t}$ as the differential force vector $\mathrm{d}\mathbf{F}$ acting over a differential surface $\mathrm{d}\mathscr{S}$. Voluntarily working with a surface in the predeformed body, the stress vector is defined as [68]

$$\mathbf{t} = \frac{\mathrm{d}\mathbf{F}}{\mathrm{d}\mathscr{S}} \tag{2.40}$$

The stress vector must then satisfy the integral equation of motion over an arbitrary

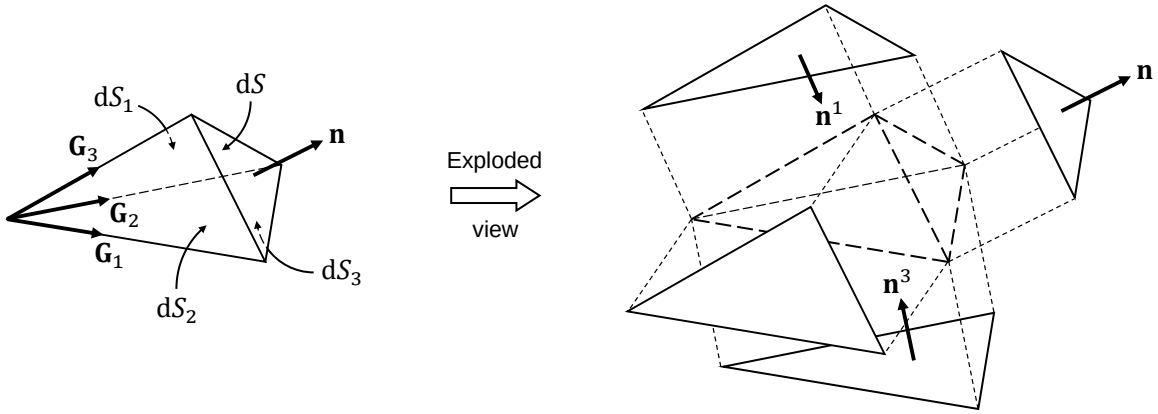

Fig. 2.3 Differential tetrahedron of volume $\mathscr{V}$ and surface $\mathrm{d}S \cup \mathrm{d}S_1 \cup \mathrm{d}S_2 \cup \mathrm{d}S_3$. Exploded view shows unit normal vectors to individual surfaces.

volume $\mathscr{V}$ (bounded by a surface $\mathscr{S}$) in the predeformed body,

$$\int_{\mathscr{S}} \mathbf{t} \mathrm{d}\mathscr{S} = \int_{\mathscr{V}} \varrho \ddot{\mathbf{u}} \mathrm{d}\mathscr{V} \tag{2.41}$$

where ϱ is the density of the predeformed body.

The classical approach to further investigating stress is to consider the above equation of motion applied to a tetrahedral differential element with surface $\mathscr{S} = \mathrm{d}S \cup \mathrm{d}S_1 \cup \mathrm{d}S_2 \cup \mathrm{d}S_3$ [68], as shown in Fig. 2.3. The areas over each surface may be expressed vectorially using the unit normal vectors to the surfaces as

$$\begin{aligned} \mathrm{d}\mathbf{S} &= \mathrm{d}S\mathbf{n} \\ \mathrm{d}\mathbf{S}_i &= \mathrm{d}S_i\mathbf{n}^i \end{aligned} \tag{2.42}$$

where $\mathbf{n}$ is the unit normal for the surface $\mathrm{d}S$, and $\mathbf{n}^i$ are the unit normals for the surfaces $\mathrm{d}S_i$. Since the surface vectors are expressed above in terms of dimensionless unit normals, the components $\mathrm{d}S$ and $\mathrm{d}S_i$ have units of area. From the orthogonality of the basis vectors, the unit normal for the i-th surface is found as

$$\mathbf{n}^i = \frac{\mathbf{G}_j \times \mathbf{G}_k}{||\mathbf{G}_j \times \mathbf{G}_k||_2} = \frac{\mathbf{G}^i}{\sqrt{G^{ii}}} \quad (i \neq j \neq k \neq i) \tag{2.43}$$

where $||\cdot||_2$ denotes the ℓ_2-norm. This justifies the notation of contravariant surface normals $\mathbf{n}^i$ and covariant surface components $\mathrm{d}S_i$. However, the subscript on $\mathrm{d}\mathbf{S}_i$ only has the meaning of an index, and not a covariant component. By representing the surface areas vectorially, the following relation must hold:

$$\mathrm{d}\mathbf{S} = \sum_{i=1}^{3} \mathrm{d}\mathbf{S}_i \tag{2.44}$$

or, equivalently, using Eq. (2.42)

$$\mathrm{d}S\mathbf{n} = \sum_{i=1}^{3} \mathrm{d}S_i \frac{\mathbf{G}^i}{\sqrt{G^{ii}}} \tag{2.45}$$

Expressing the unit normal in terms of covariant components as $\mathbf{n} = n_i\mathbf{G}^i$ allows these components to be found from the above as

$$n_i\sqrt{G^{ii}}\mathrm{d}S = \mathrm{d}S_i \tag{2.46}$$

At this point, let the stress vector over the surface $\mathrm{d}S$ be denoted $\mathbf{t}$, with $\mathbf{t}_i$ the stress vector over the i-th surface $\mathrm{d}S_i$. The integral equation of motion for the tetrahedron then becomes

$$\mathbf{t}\mathrm{d}S - \sum_{i=1}^{3} \mathbf{t}_i \mathrm{d}S_i = \varrho\ddot{\mathbf{u}}\mathrm{d}\mathscr{V} \tag{2.47}$$

where the negative sign is due to the negative orientation of the unit normals $\mathbf{n}^i$, as shown in Fig. 2.3. Since the differential volume on the righthand side is of a higher order of smallness for the differential surfaces on the lefthand side, the righthand side of the above may be taken as zero. A relation may then be formed between the stress vectors in the above as

$$\mathbf{t} = \sum_{i=1}^{3} n_i\sqrt{G^{ii}}\mathbf{t}_i \tag{2.48}$$

The terms n_i in the above may be treated as covariant components with respect to contravariant vectors $\sqrt{G^{ii}}\mathbf{t}_i$. These contravariant vectors may then be expressed in terms of the natural basis vectors for the deformed body as

$$\sqrt{G^{ii}}\mathbf{t}_i = \tau^{ij}\mathbf{G}_j \tag{2.49}$$

where τ^{ij} is defined as the contravariant stress tensor. However, since this is the predominantly used form here, it will often be simply referred to as the *stress tensor*. With this definition, the stress vector is related to the stress tensor as

$$\mathbf{t} = n_i\tau^{ij}\mathbf{G}_j \tag{2.50}$$

The differential force $\mathrm{d}\mathbf{F}$ acting over the differential surface $\mathrm{d}S$ can be expressed in terms of the stress tensor as

$$\mathrm{d}\mathbf{F} = \mathrm{d}A_i\tau^{ij}\mathbf{G}_j \tag{2.51}$$

where $\mathrm{d}A_i = \mathrm{d}S_i/\sqrt{G^{ii}}$ is the area of the i-th surface referenced to the curvilinear basis vector $\mathbf{G}^i$. Therefore, the force components acting over the surface $\mathrm{d}S$ are

$$\mathrm{d}F^j = \mathrm{d}A_i\tau^{ij} \tag{2.52}$$

The stress tensor may then be interpreted as follows: The component τ^{ij} relates to the force on the i-th surface acting in the j-th direction.[§] However, it should be noted

[§] Mixed and covariant stress tensors may also be constructed by expressing the differential force vector in two other forms:

$$\mathrm{d}\mathbf{F} = \mathrm{d}A_i\tau^i_j\mathbf{G}^j = \mathrm{d}A^i\tau_{ij}\mathbf{G}^j \tag{2.53}$$

It may then be seen from the above that the mixed and covariant stress tensors are related to the contravariant form by lowering the indices using the metric tensor for the predeformed body,

$$\begin{aligned}\tau^i_j &= G_{jk}\tau^{ik}\\ \tau_{ij} &= G_{ik}G_{jl}\tau^{kl}\end{aligned} \tag{2.54}$$

that the surfaces and directions are referenced to the predeformed body.

Having considered the stress tensor, the equation of motion may now be investigated more thoroughly. To directly compare the two integrals in Eq. (2.41), the surface integral may be transformed to a volume integral using the divergence theorem.¶ However, this requires that the integrand of the surface integral be in the form of a dot product with the unit normal vector of the surface. It is therefore convenient to introduce an alternative definition of the stress vector,

$$\mathbf{t} = n_i \frac{\mathbf{T}^i}{\sqrt{G}} \tag{2.56}$$

with a new vector $\mathbf{T}^{i\|}$ defined as

$$\mathbf{T}^i = \sqrt{G}\tau^{ij}\mathbf{G}_j \tag{2.58}$$

Equation (2.56) may then be substituted for $\mathbf{t}$ and the divergence theorem applied. Requiring the resulting integral to vanish identically requires the integrand itself to vanish, yielding the following equation of motion:

$$\frac{\mathbf{T}^i_{,i}}{\sqrt{G}} = \varrho\ddot{\mathbf{u}} \tag{2.59}$$

Substituting Eq. (2.58) into the above and expressing the acceleration in terms of

---

The need to use G_{ij} (as opposed to g_{ij}) to lower the indices reflects the fact that the stress tensor is referenced to the predeformed body.

¶ For an arbitrary vector $\mathbf{f} = f^i\mathbf{G}_i$, the divergence theorem may be expressed [68]

$$\int_{\mathscr{S}} n_i f^i \mathrm{d}\mathscr{S} = \int_{\mathscr{V}} \frac{(\sqrt{G}f^j)_{,j}}{\sqrt{G}} \mathrm{d}\mathscr{V} \tag{2.55}$$

‖ This vector also has a relation to the stress acting over a surface. For instance, consider a differential surface with normal vector $\mathbf{n}^i = \mathbf{G}^i/\sqrt{G^{ii}}$ and area $\mathrm{d}S_i = \sqrt{GG^{ii}}\mathrm{d}\theta^j\mathrm{d}\theta^k$ for i, j, k not equal. Then the use of $\mathbf{T}^i$ provides one manner of expressing the force over this surface, in terms of its differential length components $\mathrm{d}\theta^j, \mathrm{d}\theta^k$,

$$\mathbf{t}_i \mathrm{d}S_i = \mathbf{t}_i\sqrt{GG^{ii}}\mathrm{d}\theta^j\mathrm{d}\theta^k = \mathbf{T}^i\mathrm{d}\theta^j\mathrm{d}\theta^k \quad (i \neq j \neq k \neq i) \tag{2.57}$$

contravariant components as $\ddot{\mathbf{u}} = \ddot{U}^i \mathbf{G}_i$ yields

$$\tau^{ij}_{,i} \mathbf{G}_j + \tau^{ij} \mathbf{G}_{j,i} + \frac{(\sqrt{G})_{,i}}{\sqrt{G}} \tau^{ij} \mathbf{G}_j = \varrho \ddot{U}^j \mathbf{G}_j \tag{2.60}$$

Lastly, incorporating relations for the Christoffel symbols (see Appendix A.1.) reduces the above to

$$\tau^{ij}_{,i} + \Gamma^i_{ik} \tau^{kj} + \Gamma^j_{ik} \tau^{ik} = \varrho \ddot{U}^j \tag{2.61}$$

The lefthand side above may be compactly expressed by using the definition for the covariant derivative. Specifically, the covariant derivative of an arbitrary second-order tensor a^{ij} (referenced to the predeformed body) is [70]

$$a^{ij}||_k = a^{ij}_{,k} + \Gamma^i_{kl} a^{lj} + \Gamma^j_{kl} a^{il} \tag{2.62}$$

The equation of motion may then be written as

$$\tau^{ij}||_i = \varrho \ddot{U}^j \tag{2.63}$$

For the case of a static predeformation, this reduces to

$$\tau^{ij}||_i = 0 \tag{2.64}$$

5.3 Constitutive relation

Stress may be related to strain by considering the energy stored from deformation. The stress tensor τ^{ij} may then be related to the strain tensor e_{ij} through the strain energy function $\mathscr{U}$ as [68]

$$\begin{aligned} \tau^{ij} &= \frac{1}{\sqrt{I_3}} \frac{\partial \mathscr{U}}{\partial e_{ij}} \\ &= \frac{1}{\sqrt{I_3}} \frac{\partial \mathscr{U}}{\partial I_k} \frac{\partial I_k}{\partial e_{ij}} \end{aligned} \tag{2.65}$$

For an isotropic body, it is convenient to express the strain energy function in terms of strain invariants (as shown above), rather than the strain tensor itself. Here, $\mathscr{U}$ is taken as a function of the invariants I_1, I_2, I_3 following convention [68]. The derivatives of these invariants with respect to the strain tensor may be evaluated as

$$\begin{aligned} \frac{\partial I_1}{\partial e_{ij}} &= 2g^{ij} \\ \frac{\partial I_2}{\partial e_{ij}} &= 2B^{ij} \\ \frac{\partial I_3}{\partial e_{ij}} &= 2I_3 G^{ij} \end{aligned} \tag{2.66}$$

where a new tensor B^{ij} (termed the *strain derivative tensor* here) has been defined as

$$B^{ij} = I_1 g^{ij} - g^{ik} g^{jl} G_{kl} \tag{2.67}$$

Incorporating the derivatives of these strain invariants, the stress tensor can be written as follows:

$$\tau^{ij} = \Phi g^{ij} + \Psi B^{ij} + \Pi G^{ij} \tag{2.68}$$

where the coefficients Φ, Ψ, Π are defined in terms of the strain energy function as

$$\begin{aligned} \Phi &= \frac{2}{\sqrt{I_3}} \frac{\partial \mathscr{U}}{\partial I_1} \\ \Psi &= \frac{2}{\sqrt{I_3}} \frac{\partial \mathscr{U}}{\partial I_2} \\ \Pi &= 2\sqrt{I_3} \frac{\partial \mathscr{U}}{\partial I_3} \end{aligned} \tag{2.69}$$

Since the exact form of the strain energy function has not yet been specified, the above constitutive relation applies to any isotropic elastic material.

6 Wave Motion

This section analyzes the stage of small superposed motion, mapping the predeformed body $\mathscr{B}$ to the deformed body $\mathscr{C}$. It considers the strain and stress associated with the superposed motion, along with the corresponding equation of motion and boundary conditions. A small superposed displacement $\epsilon\mathbf{u}'$ is considered here, which maps a point $\mathbf{R}$ in the predeformed body to the point $\mathbf{R} + \epsilon\mathbf{u}'$ in the deformed body. This is visualized in Fig. 2.1. Since the superposed displacement is assumed to be small, only linear terms in ϵ are considered in the following analysis.

6.1 Strain

For an arbitrary predeformation, the strain tensor was defined in Sec. 5.1 as $e_{ij} = \frac{1}{2}(G_{ij} - g_{ij})$. To consider the strain tensor for the combined deformation of small-amplitude wave motion superposed on a predeformation (*i.e.*, for the deformed body), let the strain tensor for this body be $e_{ij} + \epsilon e'_{ij}$. With only linear terms in ϵ considered, this represents a small perturbation added to the predeformation strain tensor. The strain tensor e'_{ij} then corresponds to the incremental strain associated with the wave motion alone. In this thesis, a prime is used to denote an incremental quantity. With the covariant metric tensor for the deformed body similarly denoted as $G_{ij} + \epsilon G'_{ij}$, the strain tensor for this body is then

$$e_{ij} + \epsilon e'_{ij} = \tfrac{1}{2}(G_{ij} + \epsilon G'_{ij} - g_{ij}) \tag{2.70}$$

Raising one of the indices on the above using g^{ij} yields the mixed strain tensor,

$$e^i_j + \epsilon e'^i_j = \tfrac{1}{2}[g^{ik}(G_{kj} + \epsilon G'_{kj}) - \delta^i_j] \tag{2.71}$$

Following Eq. (2.34), strain invariants $I_1 + \epsilon I'_1, I_2 + \epsilon I'_2, I_3 + \epsilon I'_3$ may then be defined from the following characteristic equation:

$$\det\{g^{ik}(G_{kj}+\epsilon G'_{kj})+\Lambda\delta^i_j\}=\Lambda^3+\Lambda^2(I_1+\epsilon I'_1)+\Lambda(I_2+\epsilon I'_2)+(I_3+\epsilon I'_3) \quad (2.72)$$

The incremental strain invariants I'_1, I'_2, I'_3 are then, to first order in ϵ,

$$\begin{aligned} I'_1 &= g^{ij}G'_{ij} \\ I'_2 &= I_1 I'_1 - g^{ik}g^{jl}G_{ij}G'_{kl} \\ I'_3 &= I_3 G^{ij}G'_{ij} \end{aligned} \quad (2.73)$$

For the combined deformation, the strain derivative tensor becomes $B^{ij}+\epsilon B'^{ij}$. Using the definition of B^{ij} in Eq. (2.67), the incremental tensor then follows as (to first order in ϵ)

$$B'^{ij} = I'_1 g^{ij} - g^{ik}g^{jl}G'_{kl} \quad (2.74)$$

It may be seen that what is needed to obtain the incremental quantities outlined above is the incremental metric tensor G'_{ij}. Following the convention established in Sec. 5.1, the covariant basis vectors $\mathbf{G}_i+\epsilon\mathbf{G}'_i$ for the deformed body may be obtained as

$$\mathbf{G}_i + \epsilon\mathbf{G}'_i = \mathbf{R}_{,i} + \epsilon\mathbf{u}'_{,i} \quad (2.75)$$

It may be seen that they only deviate from the basis vectors for the predeformed body by the small perturbation $\epsilon\mathbf{u}'_{,i}$. The covariant incremental basis vectors are then

$$\mathbf{G}'_i = \mathbf{u}'_{,i} \quad (2.76)$$

The incremental displacement appearing above may voluntarily be expressed in terms of either contravariant or covariant components U'^i, U'_i referenced to the predeformed body,

$$\mathbf{u}' = U'^{i}\mathbf{G}_i = U'_j\mathbf{G}^j \tag{2.77}$$

Making use of the above allows the incremental basis vectors to be conveniently expressed in terms of those for the predeformed body as

$$\mathbf{G}'_i = U'^{j}||_i\mathbf{G}_j = U'_k||_i\mathbf{G}^k \tag{2.78}$$

As in Sec. 5.1, $\cdot||_i$ denotes covariant differentiation with respect to the coordinates θ^i in the predeformed body $\mathscr{B}$, as opposed to the deformed body $\mathscr{C}$. Following Eq. (2.14), the covariant metric tensor for the deformed body is

$$G_{ij} + \epsilon G'_{ij} = (\mathbf{G}_i + \epsilon\mathbf{G}'_i)\cdot(\mathbf{G}_j + \epsilon\mathbf{G}'_j) \tag{2.79}$$

Retaining only linear terms in ϵ from the above and making use of Eq. (2.78) yields an expression for the incremental covariant metric tensor,

$$G'_{ij} = U'_i||_j + U'_j||_i \tag{2.80}$$

The incremental contravariant metric tensor G'^{ij} may be found by considering two fundamental relations: the metric tensors for the predeformed and deformed bodies satisfy, respectively,

$$\begin{aligned} G_{ik}G^{kj} &= \delta^j_i \\ (G_{ik} + \epsilon G'_{ik})(G^{kj} + \epsilon G'^{kj}) &= \delta^j_i \end{aligned} \tag{2.81}$$

Combining the above two relations, the contravariant metric tensor G'^{ij} may be solved for as

$$G'^{ij} = -G^{ik}G^{jl}G'_{kl} \tag{2.82}$$

Lastly, let the determinant of the metric tensor $G_{ij} + \epsilon G'_{ij}$ be denoted $G + \epsilon G'$. The incremental determinant G' may then be found to first order as

$$G' = GG^{ij}G'_{ij} \tag{2.83}$$

6.2 Stress and the equation of motion

Let the stress tensor associated with the combined deformation be a small perturbation about the predeformation stress tensor as $\tau^{ij} + \epsilon\tau'^{ij}$. Similarly, let the stress coefficients in Eq. (2.68) for this deformation be $\Phi + \epsilon\Phi', \Psi + \epsilon\Psi', \Pi + \epsilon\Pi'$. The stress tensor may then be expressed as

$$\tau^{ij} + \epsilon\tau'^{ij} = (\Phi + \epsilon\Phi')g^{ij} + (\Psi + \epsilon\Psi')(B^{ij} + \epsilon B'^{ij}) + (\Pi + \epsilon\Pi')(G^{ij} + \epsilon G'^{ij}) \tag{2.84}$$

After expanding the above to first order in ϵ, the incremental stress tensor τ'^{ij} may be found as

$$\tau'^{ij} = \Phi' g^{ij} + \Psi B'^{ij} + \Psi' B^{ij} + \Pi G'^{ij} + \Pi' G^{ij} \tag{2.85}$$

From a first-order Taylor series expansion, the incremental coefficients Φ', Ψ', Π' may be expressed as

$$\begin{aligned}
\Phi' &= \Sigma_1 I'_1 + \Sigma_6 I'_2 + \Sigma_5 I'_3 - \frac{\Phi}{2I_3} I'_3 \\
\Psi' &= \Sigma_6 I'_1 + \Sigma_2 I'_2 + \Sigma_4 I'_3 - \frac{\Psi}{2I_3} I'_3 \\
\Pi' &= (\Sigma_5 I'_1 + \Sigma_4 I'_2 + \Sigma_3 I'_3) I_3 + \frac{\Pi}{2I_3} I'_3
\end{aligned} \tag{2.86}$$

where the following coefficients have been defined:

$$\Sigma_1 = \frac{2}{\sqrt{I_3}}\frac{\partial^2 \mathscr{U}}{\partial I_1^2} \qquad \Sigma_2 = \frac{2}{\sqrt{I_3}}\frac{\partial^2 \mathscr{U}}{\partial I_2^2} \qquad \Sigma_3 = \frac{2}{\sqrt{I_3}}\frac{\partial^2 \mathscr{U}}{\partial I_3^2}$$
$$\Sigma_4 = \frac{2}{\sqrt{I_3}}\frac{\partial^2 \mathscr{U}}{\partial I_2 \partial I_3} \qquad \Sigma_5 = \frac{2}{\sqrt{I_3}}\frac{\partial^2 \mathscr{U}}{\partial I_3 \partial I_1} \qquad \Sigma_6 = \frac{2}{\sqrt{I_3}}\frac{\partial^2 \mathscr{U}}{\partial I_1 \partial I_2} \tag{2.87}$$

For the combined deformation, the alternative stress vector from Eq. (2.58) becomes

$$\mathbf{T}^i + \epsilon \mathbf{T}'^i = \sqrt{G + \epsilon G'}(\tau^{ij} + \epsilon \tau'^{ij})(\mathbf{G}_j + \epsilon \mathbf{G}'_j) \tag{2.88}$$

To first order in ϵ, the incremental vector $\mathbf{T}'^i$ is then

$$\mathbf{T}'^i = \sqrt{G}\sigma'^{ij}\mathbf{G}_j \tag{2.89}$$

where Eqs. (2.80) and (2.83) have been applied, and a new stress tensor has been introduced:

$$\sigma'^{ij} = \tau'^{ij} + \tau^{ik}U'^{j}||_k + \tau^{ij}U'^{k}||_k \tag{2.90}$$

Unlike τ'^{ij}, it may be seen that this tensor is not symmetric. When applying boundary conditions, it will be useful to define the stress vector (referenced to the predeformed body) as $\mathbf{t} + \epsilon \mathbf{t}'$. Making use of Eq. (2.56), this vector may be written

$$\mathbf{t} + \epsilon \mathbf{t}' = \frac{n_i}{\sqrt{G}}(\mathbf{T}^i + \epsilon \mathbf{T}'^i) \tag{2.91}$$

Therefore, to first order, the incremental stress vector $\mathbf{t}'$ is

$$\mathbf{t}' = n_i \sigma'^{ij}\mathbf{G}_j \tag{2.92}$$

Here, when the stress vector $\mathbf{t}'$ is prescribed on a surface in the predeformed body, boundary conditions governing σ'^{ij} on that surface may be then formed.

Lastly, the equation of motion for the combined deformation becomes

$$(\tau^{ij}+\epsilon\tau'^{ij})_{,i}+(\Gamma^{j}_{ik}+\epsilon\Gamma'^{j}_{ik})(\tau^{ik}+\epsilon\tau'^{ik})+(\Gamma^{k}_{ik}+\epsilon\Gamma'^{k}_{ik})(\tau^{ij}+\epsilon\tau'^{ij})=(\varrho+\epsilon\varrho')(\ddot{U}^{j}+\epsilon\ddot{U}'^{j}) \tag{2.93}$$

where (to first order) the incremental Christoffel symbols Γ'^{k}_{ij} are

$$\Gamma'^{k}_{ij}=\tfrac{1}{2}G^{kl}(G'_{li,j}+G'_{lj,i}-G'_{ij,l})+\tfrac{1}{2}G'^{kl}(G_{li,j}+G_{lj,i}-G_{ij,l}) \tag{2.94}$$

Expanding Eq. (2.93) and enforcing a static predeformation, the equation of motion for the incremental deformation may be found as

$$\tau'^{ij}||_{i}+\Gamma'^{j}_{ik}\tau^{ik}+\Gamma'^{k}_{ik}\tau^{ij}=\varrho\ddot{U}'^{j} \tag{2.95}$$

7 Second-Order Elasticity and Linearization

Experimental studies have established that linear elasticity is not sufficient for describing the effect of stress on wave propagation (*i.e.*, the acoustoelastic effect) in relatively stiff materials (such as steel) [71]. Instead, second-order elasticity is required. This section therefore adapts the acoustoelastic theory from the previous sections to a second-order elasticity framework. Following acoustoelastic convention [72], the results are also linearized in strain.

Under linear (first-order) elasticity, stress is a function of first-order terms in strain, with the strain energy function containing second-order terms. Therefore, under second-order elasticity, the strain energy function is expanded up to third-order terms in strain. This expansion is carried out here following Murnaghan's approach [73] as[**]

[**] It should be noted that this is not the only possible third-order expansion of a strain energy function. Other notable formulations have been presented by Rivlin [74], Thurston and Brugger [75], Toupin and Bernstein [76], Landau and Lifschitz [77], and Eringen and Suhubi [78].

$$\mathscr{U} = \tfrac{1}{2}(\lambda + 2\mu)I^2 - 2\mu II + \tfrac{1}{3}(l + 2m)I^3 - 2mI\,II + n\,III \tag{2.96}$$

where λ and μ are the Lamé elastic constants, and l, m, and n are the Murnaghan elastic constants. This formulation is convenient, since the terms I^2 and II are purely second-order quantities in strain, while I^3, $I\,II$, and III are purely third-order quantities in strain. For this reason, the Lamé and Murnaghan constants are also referred to as second- and third-order elastic constants, respectively.

It should be noted that Murnaghan has defined the constants l, m, n in two alternative manners: Lagrangian [73] and Eulerian [81]. The acoustoelastic analysis presented here allows for either a Lagrangian or Eulerian framework for the curvilinear coordinates (and therefore the strain tensor e_{ij}, see pp. 24-24). However, the strain invariants I, II, III remain unchanged between the two frameworks, since they are constructed from a mixed strain tensor defined as $e^i_j = g^{ik}e_{kj}$. With the metric tensor for the undeformed body g^{ij} used in this construction, these strain invariants should be treated as Lagrangian strain invariants. Therefore, the Murnaghan constants used here correspond to the Lagrangian form defined in [73].

In the previous section, the constitutive terms are defined via derivatives of the strain energy function. These derivatives may be evaluated to first-order in strain using the chain rule between the two sets of invariants (I_1, I_2, I_3 and I, II, III), yielding

$$\begin{aligned}
\frac{\partial \mathscr{U}}{\partial I_1} &= \tfrac{1}{8}(8\mu + n) + \tfrac{1}{2}(\lambda + 2\mu + 2m)\delta \\
\frac{\partial \mathscr{U}}{\partial I_2} &= -\tfrac{1}{8}(4\mu + n) - \tfrac{1}{2}m\delta \\
\frac{\partial \mathscr{U}}{\partial I_3} &= \tfrac{1}{8}n \\
\frac{\partial^2 \mathscr{U}}{\partial I_1^2} &= \tfrac{1}{4}(\lambda + 2\mu + 4m) + \tfrac{1}{2}(l + 2m)\delta \\
\frac{\partial^2 \mathscr{U}}{\partial I_1 \partial I_2} &= -\tfrac{1}{4}m
\end{aligned} \tag{2.97}$$

Relations between the Murnaghan third-order constants and those defined by these authors may be found in [79, 80].

with all other $\partial^2 \mathscr{U} / \partial I_i \partial I_j = 0$. Here, the strain invariants have been expressed to first-order as

$$I = \delta \tag{2.98}$$

where $II = III = 0$. The strain invariants I_1, I_2, I_3 may similarly be expressed to first-order solely using the dilatation as

$$\begin{aligned} I_1 &= 3 + 2\delta \\ I_2 &= 3 + 4\delta \\ I_3 &= 1 + 2\delta \end{aligned} \tag{2.99}$$

With the dilatation representing the volume change during a deformation, the density of the predeformed body may be reduced to the following linear relation:

$$\varrho = (1 - \delta)\rho \tag{2.100}$$

In addition, the predeformation stress coefficients may also be expressed to first-order using the dilatation as

$$\begin{aligned} \Phi &= \tfrac{1}{4}(8\mu + n) + \tfrac{1}{4}(4\lambda + 8m - n)\delta \\ \Psi &= -\tfrac{1}{4}(4\mu + n) + \tfrac{1}{4}(4\mu - 4m + n)\delta \\ \Pi &= \tfrac{1}{4}n(1 + \delta) \end{aligned} \tag{2.101}$$

This leads to the predeformation stress tensor becoming, to first-order in strain,

$$\tau^{ij} = \lambda\delta g^{ij} + 2\mu e^{ij} \tag{2.102}$$

with the contravariant strain tensor expressed to first-order as [70]

$$e^{ij} = \tfrac{1}{2}(g^{ij} - G^{ij}) \tag{2.103}$$

It may be seen that Eq. (2.102) is the same expression found in linear elasticity, since there the stress is also expressed to first-order in strain. Therefore, the addition of higher-order terms in the strain energy function does not impact the linear stress-strain relation for small predeformations.

The constitutive relation in Eq. (2.102) becomes the most simple in terms of mixed stress and strain tensors, $\tau^i_j = G_{jk}\tau^{ik}$ and $e^i_j = g_{jk}e^{ik}$, since the particular geometry of the space is nullified. Multiplying this equation by $G_{ij} = g_{ij} + 2e_{ij}$ and neglecting higher-order terms yields

$$\tau^i_j = \lambda\delta\delta^i_j + 2\mu e^i_j \tag{2.104}$$

This equation may be inverted to express the strain in terms of stress using the Young's modulus E and Poisson ratio ν [82],

$$e^i_j = \frac{1+\nu}{E}\tau^i_j - \frac{\nu}{E}\tau^k_k\delta^i_j \tag{2.105}$$

According to this operation, the Young's modulus and Poisson ratio are related to the Lamé constants as

$$E = \frac{\mu(3\lambda + 2\mu)}{\lambda + \mu} \qquad \nu = \frac{\lambda}{2(\lambda + \mu)} \tag{2.106}$$

The metric tensors may also be used to raise and lower indices in order to express Eq. (2.105) as the inverse of Eq. (2.102)

$$e_{ij} = \frac{1+\nu}{E}G_{ik}G_{jl}\tau^{kl} - \frac{\nu}{E}G_{ij}G_{kl}\tau^{kl} \tag{2.107}$$

In this way, the covariant strain tensor may be obtained when the contravariant stress tensor is specified.

To obtain the incremental stress tensor, the stress coefficients Φ', Ψ', Π' from Eq. (2.86) must be obtained. To this aim, the coefficients $\Sigma_1, \ldots, \Sigma_6$ appearing in this equation may be found to first-order as

$$\begin{aligned} \Sigma_1 &= \Upsilon = \tfrac{1}{2}(\lambda + 2\mu + 4m) - \tfrac{1}{2}(\lambda + 2\mu - 2l)\delta \\ \Sigma_6 &= \Sigma = -\tfrac{1}{2}m(1 - \delta) \end{aligned} \tag{2.108}$$

with all other $\Sigma_i = 0$. The coefficients Φ', Ψ', Π' may then be found as

$$\begin{aligned} \Phi' &= \Upsilon I_1' + \Sigma I_2' - \frac{\Phi}{2I_3} I_3' \\ \Psi' &= \Sigma I_1' - \frac{\Psi}{2I_3} I_3' \\ \Pi' &= \frac{\Pi}{2I_3} I_3' \end{aligned} \tag{2.109}$$

The above analysis demonstrates the necessity of the second-order elasticity framework. Specifically, it may be seen that third-order elastic constants are coupled to the linearized results. This is in addition to the coupling of second-order constants. Since third-order constants are often considerably larger in magnitude than their second-order counterparts [83, p. 274], omitting the former from the linearized solution would introduce significant error.

7.1 Static analysis of strands

The first of two applications in this thesis regards stress monitoring in seven-wire steel strands. As such, the stress state within a strand under a typical loading condition is considered. In addition, stress monitoring within the elastic regime is targeted, so that a first-order analysis in strain may be presented.

The typical state of loading considered is a strand under tensile force between two anchorage points, so that the strand ends are restricted from rotating. Due to such loading and rotation restrictions, a variety of forces develop in the peripheral wires. These include axial, bending, and twisting forces. However, the core wire only

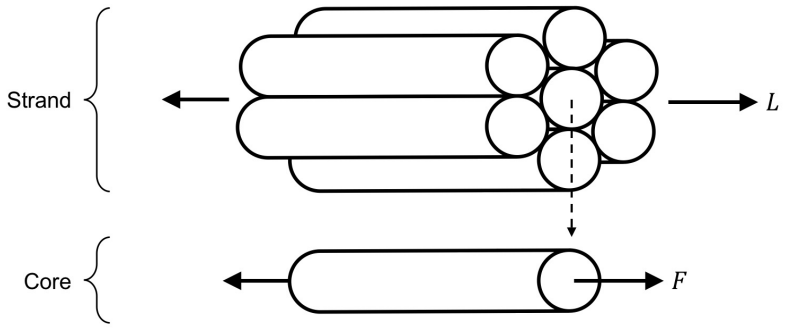

Fig. 2.4 Global force condition in the core wire of a strand under an axial load L.

experiences an axial force F [84], as shown in Fig. 2.4. For some axial force L in the strand, the correspond force in the core wire may be found to first-order as [84]

$$F = \frac{A_{\text{core}}}{A_{\text{core}} + 6A_{\text{per}}} L \tag{2.110}$$

where A_{core} and A_{per} are the cross-sectional areas of the core and peripheral wires, respectively, and the lay angle of the peripheral wires is assumed to be small.

Aside from the global conditions, it should be noted that highly localized radial stresses exist at the contact points between the core and peripheral wires [84]. These stresses are caused by interwire contact forces and are visualized in Fig. 2.5. They may be considered radial by assuming that frictional forces between wires can be neglected [84]. Such interwire stresses can be seen in a number of numerical studies [38, 85, 86]. Using Hertzian contact theory, Bartoli [85] found that these stresses are localized within an area spanning roughly $3\ell_{\text{arc}}$ in length, with ℓ_{arc} the half-length of the contact arc (shown in Fig. 2.5). The contact arc length is proportional to the square root of the interwire contact force, which at 70% UTS yields $\ell_{\text{arc}} = 73$ μm in a typical 5.2-mm-diameter core wire [85]. Therefore, at this large level of load, the contact stresses are localized in an area roughly $3\ell_{\text{arc}} = 0.2$ mm in length, equal to roughly 4% of the core wire diameter.

The existence of contact forces complicates the stress state within the core wire. However, along with the fact that the contact stresses may be neglected when con-

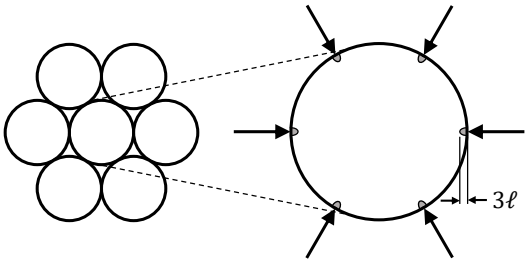

Fig. 2.5 Illustration of interwire contact forces in the core wire of an axially loaded strand. Shaded areas indicate localized stress regions due to contact forces.

sidering the global deformation of the core wire [84], it is possible that they may also be neglected when focusing on a special class of wave motion in the core wire. From work on the effect of nonuniform stress profiles on wave motion [87], motion localized near the core of a wire will be minimally affected by stresses localized near the surface. Concerning such motion, the stress state in a core wire is therefore taken as uniaxial at some value τ. To first-order, this may be expressed as

$$\tau = \frac{F}{A_{\text{core}}} \tag{2.111}$$

8 Bulk Waves

To investigate wave motion in the core wire of a strand, it will prove useful to first consider the simpler case of bulk wave motion in an unbounded body. A bulk wave is perhaps the simplest solution to the equation of motion, and provides a reference point for the analysis of GWs. In this section, the bodies $\mathscr{A}, \mathscr{B}, \mathscr{C}$ are therefore taken as extending to infinity, in the sense that reflections from the edges of a finite body are not considered. Plane bulk waves (*i.e.*, those with straight-crested, or planar, wavefronts) are considered, which may be described using cartesian coordinates.

Therefore, an adaptation of the general theory from Secs. 5 and 6 to cartesian coordinates is presented first. This is then followed by the analysis of bulk wave motion under some uniaxial stress τ.

8.1 Cartesian coordinate adaptation

For simplicity, let the curvilinear coordinates θ^i be the cartesian coordinates $X^1 = X, X^2 = Y, X^3 = Z$ of the predeformed body,

$$\theta^1 = X \qquad \theta^2 = Y \qquad \theta^3 = Z \tag{2.112}$$

Since the covariant and contravariant cartesian components are identical for the predeformed body, the covariant curvilinear coordinates are equivalent to the contravariant components. A number of simplifications to the equations throughout Secs. 5 and 6 then result. In particular, the metric tensors for the predeformed body reduce to Kronecker deltas,

$$G_{ij} = G^{ij} = \delta_{ij} \tag{2.113}$$

Furthermore, the Christoffel symbols for the predeformed body vanish,

$$\Gamma^k_{ij} = 0 \tag{2.114}$$

Therefore, there is no distinction between covariant differentiation and partial differentiation for this body (*i.e.*, $\cdot||_i = \cdot_{,i}$).

Consider a predeformation under a uniform uniaxial stress τ along the Z coordinate. The predeformation stress tensor is then

$$\tau^{33} = \tau \tag{2.115}$$

with all other $\tau^{ij} = 0$. To first-order, the strain tensor from Eq. (2.107) is then

expressed in terms of an axial strain $e = \tau/E$ as

$$\begin{aligned} e_{11} &= e_{22} = -\nu e \\ e_{33} &= e \end{aligned} \tag{2.116}$$

with all other $e_{ij} = 0$. With the principal axes of predeformation oriented along the cartesian axes, define the principal stretches along the X, Y, Z coordinates as $\lambda_{\mathrm{x}}, \lambda_{\mathrm{y}}, \lambda_{\mathrm{z}}$. The cartesian coordinates $x^1 = x, x^2 = y, x^3 = z$ in the undeformed body are then related to the curvilinear coordinates as

$$x^1 = \frac{\theta^1}{\lambda_{\mathrm{x}}} \qquad x^2 = \frac{\theta^2}{\lambda_{\mathrm{y}}} \qquad x^3 = \frac{\theta^3}{\lambda_{\mathrm{z}}} \tag{2.117}$$

From Eqs. (2.8) and (2.9), the metric tensors for the undeformed body may then be expressed in terms of the stretches as

$$\begin{aligned} g_{11} &= \frac{1}{g^{11}} = \frac{1}{\lambda_{\mathrm{x}}^2} \\ g_{22} &= \frac{1}{g^{22}} = \frac{1}{\lambda_{\mathrm{y}}^2} \\ g_{33} &= \frac{1}{g^{33}} = \frac{1}{\lambda_{\mathrm{z}}^2} \end{aligned} \tag{2.118}$$

From Eq. (2.16), the strain tensor may then be related to the stretches (to first order) as

$$\begin{aligned} \lambda_{\mathrm{x}} &= 1 + e_{11} = \xi \\ \lambda_{\mathrm{y}} &= 1 + e_{22} = \xi \\ \lambda_{\mathrm{z}} &= 1 + e_{33} = \eta \end{aligned} \tag{2.119}$$

where the X and Y coordinate stretches take on the same value based on the equivalent strain components $e_{11} = e_{22}$. The terms ξ and η defined above may be interpreted as the stretches in directions perpendicular and parallel to the uniaxial stress, respec-

tively. Substituting the above stretches into Eq. (2.118), it may be seen that (to first order) there is no difference between the covariant, contravariant, and mixed strain tensors. The dilatation from Eq. (2.98) is then

$$\delta = (1 - 2\nu)e \tag{2.120}$$

Following from the metric tensors, the strain invariants I_1, I_2, I_3 are

$$\begin{aligned} I_1 &= 2\xi^2 + \eta^2 \\ I_2 &= (\xi^2 + 2\eta^2)\xi^2 \\ I_3 &= \xi^4\eta^2 \end{aligned} \tag{2.121}$$

To first order, these invariants may also be found from the dilatation using Eq. (2.99). Lastly, the strain derivative tensor from Eq. (2.67) is

$$\begin{aligned} B^{11} &= B^{22} = (\xi^2 + \eta^2)\xi^2 \\ B^{33} &= 2\xi^2\eta^2 \end{aligned} \tag{2.122}$$

with all other $B^{ij} = 0$.

8.2 Bulk wave motion

To satisfy the incremental equation of motion (see Eq. (2.95)), consider a harmonic bulk wave propagating along the direction of the applied stress (*i.e.*, the Z coordinate in the predeformed body). This is the bulk wave analog of a GW propagating along a stressed core wire of a strand. With the spatial and time periodicity of the wave described by a wavenumber K and angular frequency ω, the displacement components may be expressed as

$$
\begin{aligned}
U'^1 = u &= U\exp[\mathrm{i}(KZ - \omega t)] \\
U'^2 = v &= V\exp[\mathrm{i}(KZ - \omega t)] \\
U'^3 = w &= W\exp[\mathrm{i}(KZ - \omega t)]
\end{aligned}
\tag{2.123}
$$

where U, V, W are the amplitude components of the wave. Since the predeformation is uniform, the amplitude components are constant and do not vary in space. Furthermore, since the wave displacements are referenced to cartesian coordinates, there is no difference between the covariant and contravariant components, $U'_i = U'^i$. From Eqs. (2.80) and (2.82), the incremental metric tensors are

$$
\begin{aligned}
G'_{33} &= -G'^{33} = 2\frac{\partial w}{\partial Z} \\
G'_{13} = G'_{31} &= -G'^{13} = -G'^{31} = \frac{\partial u}{\partial Z} \\
G'_{23} = G'_{32} &= -G'^{23} = -G'^{32} = \frac{\partial v}{\partial Z}
\end{aligned}
\tag{2.124}
$$

with all other $G'_{ij} = 0$ and $G'^{ij} = 0$. Consequently, the incremental strain invariants are

$$
\begin{aligned}
I'_1 &= 2\eta^2\frac{\partial w}{\partial Z} \\
I'_2 &= 4\xi^2\eta^2\frac{\partial w}{\partial Z} \\
I'_3 &= 2I_3\frac{\partial w}{\partial Z}
\end{aligned}
\tag{2.125}
$$

The incremental strain derivative tensor is then

$$
\begin{aligned}
B'^{11} = B'^{22} &= 2\xi^2\eta^2\frac{\partial w}{\partial Z} \\
B'^{13} = B'^{31} &= -\xi^2\eta^2\frac{\partial u}{\partial Z} \\
B'^{23} = B'^{32} &= -\xi^2\eta^2\frac{\partial v}{\partial Z}
\end{aligned}
\tag{2.126}
$$

with all other $B'^{ij} = 0$. In addition, the incremental Christoffel symbols are

$$\Gamma'^{1}_{33} = \frac{\partial^2 u}{\partial Z^2} \qquad \Gamma'^{2}_{33} = \frac{\partial^2 v}{\partial Z^2} \qquad \Gamma'^{3}_{33} = \frac{\partial^2 w}{\partial Z^2} \tag{2.127}$$

with all other $\Gamma'^{k}_{ij} = 0$. The stress coefficients Σ and Υ may be found to first-order from the dilatation using Eq. (2.108). The incremental coefficients Φ', Ψ', Π' then follow from Eq. (2.109) as

$$\begin{aligned} \Phi' &= (2\eta^2\Upsilon + 4\xi^2\eta^2\Sigma - \Phi)\frac{\partial w}{\partial Z} \\ \Psi' &= (2\eta^2\Sigma - \Psi)\frac{\partial w}{\partial Z} \\ \Pi' &= \Pi\frac{\partial w}{\partial Z} \end{aligned} \tag{2.128}$$

For the bulk wave motion considered here, the incremental stress tensor from Eq. (2.85) reduces to

$$\begin{aligned} \tau'^{11} &= \tau'^{22} = \alpha_1\frac{\partial w}{\partial Z} \\ \tau'^{33} &= \alpha_2\frac{\partial w}{\partial Z} \\ \tau'^{13} &= \tau'^{31} = \alpha_3\frac{\partial u}{\partial Z} \\ \tau'^{23} &= \tau'^{32} = \alpha_3\frac{\partial v}{\partial Z} \end{aligned} \tag{2.129}$$

with all other $\tau'^{ij} = 0$, and the coefficients $\alpha_1, \alpha_2, \alpha_3$ defined as

$$\begin{aligned} \alpha_1 &= 2\xi^2\eta^2\Upsilon + 2(3\xi^2 + \eta^2)\xi^2\eta^2\Sigma - 2\alpha_3 \\ \alpha_2 &= 2\eta^4\Upsilon + 8\xi^2\eta^4\Sigma - \tau \\ \alpha_3 &= \xi^2(\Phi + \xi^2\Psi) \end{aligned} \tag{2.130}$$

Due to the above Christoffel symbols, the equations of motion governing the bulk wave reduce to

$$\begin{aligned}
\frac{\partial \tau'^{13}}{\partial Z} + \tau \frac{\partial^2 u}{\partial Z^2} &= \varrho \ddot{u} \\
\frac{\partial \tau'^{23}}{\partial Z} + \tau \frac{\partial^2 v}{\partial Z^2} &= \varrho \ddot{v} \\
\frac{\partial \tau'^{33}}{\partial Z} + 2\tau \frac{\partial^2 w}{\partial Z^2} &= \varrho \ddot{w}
\end{aligned} \tag{2.131}$$

Substituting the considered displacements yields the following:

$$\begin{aligned}
(\alpha_3 + \tau)U &= \varrho C^2 U \\
(\alpha_3 + \tau)V &= \varrho C^2 V \\
(\alpha_2 + 2\tau)W &= \varrho C^2 W
\end{aligned} \tag{2.132}$$

where the wave velocity referenced to the predeformed body is defined as $C = \omega/K$. To first-order, the two solutions $C_\mathrm{s}, C_\mathrm{l}$ for the above velocity may be expressed in terms of the predeformation strain as

$$\begin{aligned}
\varrho C_\mathrm{s}^2 &= \alpha_3 + \tau = \mu + [(1-2\nu)\lambda + 3\mu + (1-2\nu)m + \tfrac{1}{2}\nu n]e \\
\varrho C_\mathrm{l}^2 &= \alpha_2 + 2\tau = \lambda + 2\mu + [4\lambda + 4(2+\nu)\mu + 2(1-2\nu)l + 4m]e
\end{aligned} \tag{2.133}$$

which correspond to two types of bulk waves. The first corresponds to shear motion, which is polarized in either one of the perpendicular directions X and Y, respectively. The second corresponds to longitudinal motion polarized along the direction of propagation Z. Interestingly, it may be seen that the longitudinal wave does not depend on the third Murnaghan constant n, while the shear wave does not depend on the first Murnaghan constant l. The two forms of wave motion are visualized in Fig. 2.6.

To describe the bulk waves in terms of the undeformed body, the predeformed density ϱ may be expressed in terms of the undeformed density ρ using Eq. (2.100). Further, a change of coordinates may be introduced using $Z = \eta z$,

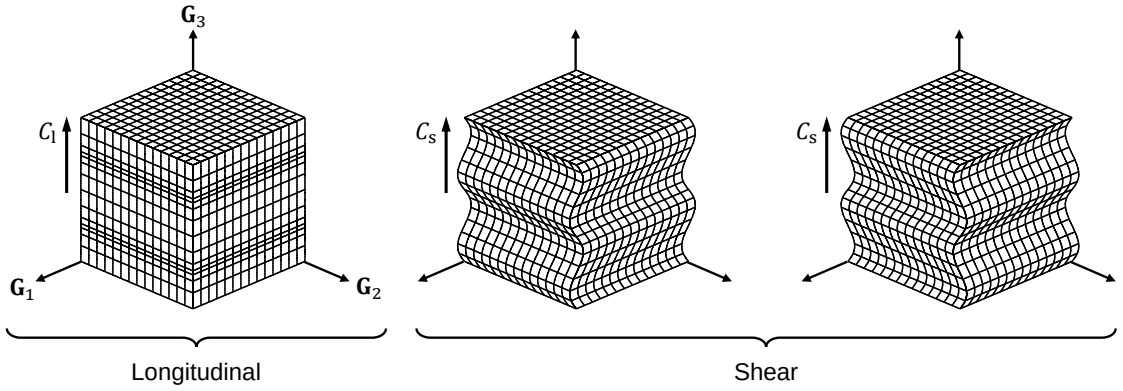

Fig. 2.6 Longitudinal and shear bulk wave motion in a cubic section of the predeformed body. Velocities for each illustrated.

$$\begin{aligned} u &= U\exp[\mathrm{i}(kz-\omega t)] \\ v &= V\exp[\mathrm{i}(kz-\omega t)] \\ w &= W\exp[\mathrm{i}(kz-\omega t)] \end{aligned} \tag{2.134}$$

where the wavenumber referenced to the undeformed body is defined as $k = \eta K$. Furthermore, the velocity referenced to this body may be obtained as $c = \omega/k$. The bulk velocities referenced to the undeformed body may then be found by retaining only first-order strain terms,

$$\begin{aligned} \rho c_{\mathrm{s}}^2 &= \mu + [(1-2\nu)\lambda + 2(1-\nu)\mu + (1-2\nu)m + \tfrac{1}{2}\nu n]e \\ \rho c_{\mathrm{l}}^2 &= \lambda + 2\mu + [(3-2\nu)\lambda + 6\mu + 2(1-2\nu)l + 4m]e \end{aligned} \tag{2.135}$$

Lastly, it may be seen that for the special case of zero stress the above velocities for the longitudinal and shear motions reduce to the classical longitudinal and shear wave velocities, defined respectively as

$$\begin{aligned} \rho c_{\mathrm{s0}}^2 &= \mu \\ \rho c_{\mathrm{l0}}^2 &= \lambda + 2\mu \end{aligned} \tag{2.136}$$

where the subscript 0 indicates the reference value at zero stress. Since the acous-

toelastic effect is relatively small, it is useful to consider the change in velocity with respect to a reference state. Using the above reference velocities for the case of zero stress, the change in velocity for longitudinal and shear waves may be expressed in the linear form

$$\begin{aligned} \Delta c_{\mathrm{s}} &= c_{\mathrm{s}} - c_{\mathrm{s}0} = \kappa_{\mathrm{s}} \Delta\tau \\ \Delta c_{\mathrm{l}} &= c_{\mathrm{l}} - c_{\mathrm{l}0} = \kappa_{\mathrm{l}} \Delta\tau \end{aligned} \tag{2.137}$$

where $\Delta\tau$ is the stress change from the reference state, and the coefficients κ_{l} and κ_{s} are known as acoustoelastic constants, defined respectively as

$$\begin{aligned} \kappa_{\mathrm{s}} &= \frac{2(1-2\nu)\lambda + 4(1-\nu)\mu + 2(1-2\nu)m + \nu n}{4\mu} \frac{c_{\mathrm{s}0}}{E} \\ \kappa_{\mathrm{l}} &= \frac{(3-2\nu)\lambda + 6\mu + 2(1-2\nu)l + 4m}{2(\lambda+2\mu)} \frac{c_{\mathrm{l}0}}{E} \end{aligned} \tag{2.138}$$

9 Guided Waves

This section builds upon the previous, considering GW motion in an axially stressed rod. Here, the rod is taken to idealize the core wire of a seven-wire strand. Since the rod is naturally described in cylindrical coordinates, the general formulation in Secs. 5 and 6 is first adapted to this case. Afterward, the study of GWs is performed using the cylindrical coordinate description. Although various families of GW modes exist in a rod (including longitudinal, torsional, and flexural) [35], this thesis only focuses on the more practical longitudinal modes.

The problem of longitudinal GW motion in an axially stressed rod was perhaps first considered by Suhubi [69], where an arbitrary hyperelastic rod was considered. This section expands upon Suhubi's work within the second-order elasticity framework presented in Sec. 7, while considering the small predeformations applicable to strands.

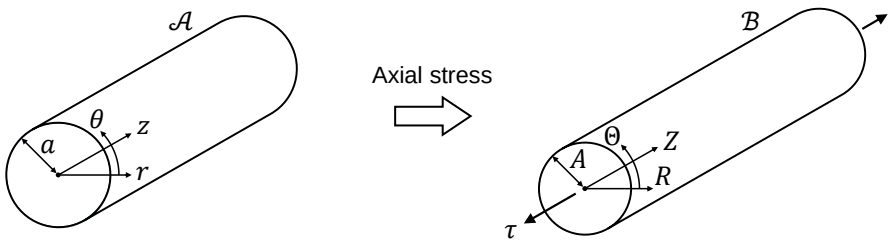

Fig. 2.7 Rod idealization of core wire in an axially stressed strand. Undeformed $\mathscr{A}$ and predeformed $\mathscr{B}$ bodies shown, with radii of a and A, respectively. Cylindrical coordinates associated with each body are overlain. (Note: rods extend to infinity.)

In addition, the modeshapes are derived and studied in detail, and the behavior of higher-order modes is investigated.

9.1 Cylindrical coordinate adaptation

To describe GWs in a predeformed rod, let the curvilinear coordinates be taken as the cylindrical coordinates R, Θ, Z of the predeformed body,

$$\theta^1 = R \qquad \theta^2 = \Theta \qquad \theta^3 = Z \tag{2.139}$$

As shown in Fig. 2.7, the predeformed body $\mathscr{B}$ is taken as a rod with radius A, whose length extends to infinity. Unlike in Sec. 8, there is now a distinction between the covariant θ_i and contravariant θ^i components. With the curvilinear coordinates being cylindrical, they are related to the cartesian coordinates of the predeformed body as

$$\begin{aligned} X^1 &= \theta^1 \cos(\theta^2) \\ X^2 &= \theta^1 \sin(\theta^2) \\ X^3 &= \theta^3 \end{aligned} \tag{2.140}$$

Following this choice of coordinates, the metric tensors for the predeformed body are

$$
\begin{aligned}
G_{11} &= G^{11} = 1 \\
G_{22} &= \frac{1}{G^{22}} = R^2 \\
G_{33} &= G^{33} = 1
\end{aligned}
\tag{2.141}
$$

with all other $G_{ij} = 0$ and $G^{ij} = 0$. In addition, the Christoffel symbols for this body are

$$
\Gamma^1_{22} = -R \qquad \Gamma^2_{12} = \Gamma^2_{21} = \frac{1}{R}
\tag{2.142}
$$

with all other $\Gamma^k_{ij} = 0$.

Consider a predeformation under a uniform stress τ along the Z coordinate, as illustrated in Fig. 2.7. This represents the axial stress in the core wire of an axially loaded strand. The predeformation stress tensor τ^{ij} is then the same as in Eq. (2.115). The predeformation strain tensor may then be found in terms of the axial strain e as

$$
\begin{aligned}
e_{11} &= -\nu e \\
R^2 e_{22} &= -\nu e \\
e_{33} &= e
\end{aligned}
\tag{2.143}
$$

with all other $e_{ij} = 0$. With the principal axes of predeformation oriented along the radial and axial coordinates, define the principal stretches along these coordinates as λ_{r} and λ_{z}, respectively. Further, the predeformation is axisymmetric, so that the cylindrical coordinates of the predeformed body are related to those of the undeformed body as

$$
\begin{aligned}
R &= \lambda_{\mathrm{r}} r \\
\Theta &= \theta \\
Z &= \lambda_{\mathrm{z}} z
\end{aligned}
\tag{2.144}
$$

Here, the angular stretch is unity (*i.e.*, $\lambda_\theta = 1$), and is for simplicity not shown above. The cartesian coordinates in the undeformed body are then related to the curvilinear coordinates as

$$\begin{aligned} x^1 &= \frac{\theta^1}{\lambda_\mathrm{r}} \cos(\theta^2) \\ x^2 &= \frac{\theta^1}{\lambda_\mathrm{r}} \sin(\theta^2) \\ x^3 &= \frac{\theta^3}{\lambda_\mathrm{z}} \end{aligned} \tag{2.145}$$

The metric tensors for the undeformed body may then be found as

$$\begin{aligned} g_{11} &= \frac{1}{g^{11}} = \frac{1}{\lambda_\mathrm{r}^2} \\ g_{22} &= \frac{1}{g^{22}} = \frac{R^2}{\lambda_\mathrm{r}^2} \\ g_{33} &= \frac{1}{g^{33}} = \frac{1}{\lambda_\mathrm{z}^2} \end{aligned} \tag{2.146}$$

with all other $g_{ij} = 0$ and $g^{ij} = 0$. Subsequently, the stretches may be found to first order as

$$\begin{aligned} \lambda_\mathrm{r} &= 1 + e_{11} = \xi \\ \lambda_\mathrm{z} &= 1 + e_{33} = \eta \end{aligned} \tag{2.147}$$

The terms ξ and η represent the stretches in directions perpendicular and parallel to the axial stress, respectively (as in Sec. 8). To first order, the mixed strain tensor is then

$$\begin{aligned} e_1^1 &= e_2^2 = e_{11} \\ e_3^3 &= e_{33} \end{aligned} \tag{2.148}$$

with all other $e_j^i = 0$. These are the same mixed strain tensor components found in the

previous section, since the mixed tensor removes the effects of the curved cylindrical space. In terms of the axial strain, the dilatation δ then reduces to same value as in Sec. 8. In addition, the strain invariants I_1, I_2, I_3 and stress coefficients Φ, Ψ, Π take on the same values as in Sec. 8. However, the strain derivative tensor becomes

$$\begin{aligned} B^{11} &= (\xi^2 + \eta^2)\xi^2 \\ R^2 B^{22} &= (\xi^2 + \eta^2)\xi^2 \\ B^{33} &= 2\xi^2\eta^2 \end{aligned} \tag{2.149}$$

with all other $B^{ij} = 0$.

9.2 Longitudinal wave motion

This thesis focuses on the longitudinal family of GW motion, in which there is no angular displacement (*i.e.*, $U'^2 = U'_2 = 0$). Therefore, let the nonzero contravariant displacement components associated with the wave motion be

$$U'^1 = u \qquad U'^3 = w \tag{2.150}$$

From the metric tensors, it may be seen that there is no difference between the covariant and contravariant components for radial and axial displacement, and therefore $U'_i = U'^i$. Based on this type of motion, the incremental metric tensors are

$$\begin{aligned} G'_{11} &= -G'^{11} = 2\frac{\partial u}{\partial R} \\ G'_{22} &= -R^4 G'^{22} = 2Ru \\ G'_{33} &= -G'^{33} = 2\frac{\partial w}{\partial Z} \\ G'_{13} &= G'_{31} = -G'^{13} = -G'^{31} = \frac{\partial u}{\partial Z} + \frac{\partial w}{\partial R} \end{aligned} \tag{2.151}$$

with all other G'_{ij} and G'^{ij} equal to zero. Additionally, the incremental strain deriva-

tive tensor B'^{ij} is

$$\begin{aligned} B'^{11} &= 2\xi^2\left(\xi^2\frac{u}{R}+\eta^2\frac{\partial w}{\partial Z}\right) \\ R^2B'^{22} &= 2\xi^2\left(\xi^2\frac{\partial u}{\partial R}+\eta^2\frac{\partial w}{\partial Z}\right) \\ B'^{33} &= 2\xi^2\eta^2\left(\frac{\partial u}{\partial R}+\frac{u}{R}\right) \\ B'^{13} &= B'^{31} = -\xi^2\eta^2\left(\frac{\partial u}{\partial Z}+\frac{\partial w}{\partial R}\right) \end{aligned} \tag{2.152}$$

with all other $B'^{ij}=0$. The incremental strain invariants are then

$$\begin{aligned} I_1' &= 2\xi^2\left(\frac{\partial u}{\partial R}+\frac{u}{R}\right)+2\eta^2\frac{\partial w}{\partial Z} \\ I_2' &= 2\xi^2(\xi^2+\eta^2)\left(\frac{\partial u}{\partial R}+\frac{u}{R}\right)+4\xi^2\eta^2\frac{\partial w}{\partial Z} \\ I_3' &= 2I_3\left(\frac{\partial u}{\partial R}+\frac{u}{R}+\frac{\partial w}{\partial Z}\right) \end{aligned} \tag{2.153}$$

and the incremental Christoffel symbols are

$$\Gamma'^1_{31}=\frac{\partial^2 u}{\partial R\partial Z} \qquad \Gamma'^2_{32}=\frac{1}{R}\frac{\partial u}{\partial Z} \qquad \Gamma'^1_{33}=\frac{\partial^2 u}{\partial Z^2} \qquad \Gamma'^3_{33}=\frac{\partial^2 w}{\partial Z^2} \tag{2.154}$$

with all other $\Gamma'^k_{ij}=0$. Consequently, the incremental stress tensor may be found as

$$\begin{aligned} \tau'^{11} &= \alpha_4\frac{\partial u}{\partial R}+(\alpha_4+2\xi^4\Psi+2\Pi)\frac{u}{R}+\alpha_1\frac{\partial w}{\partial Z} \\ R^2\tau'^{22} &= \alpha_4\frac{u}{R}+(\alpha_4+2\xi^4\Psi+2\Pi)\frac{\partial u}{\partial R}+\alpha_1\frac{\partial w}{\partial Z} \\ \tau'^{33} &= (\alpha_1-\tau)\left(\frac{\partial u}{\partial R}+\frac{u}{R}\right)+\alpha_2\frac{\partial w}{\partial Z} \\ \tau'^{13} &= \tau'^{31} = \alpha_3\left(\frac{\partial u}{\partial Z}+\frac{\partial w}{\partial R}\right) \end{aligned} \tag{2.155}$$

with all other $\tau'^{ij}=0$. The coefficients $\alpha_1,\alpha_2,\alpha_3$ are the same as those defined in Sec. 8, while the new coefficient α_4 is defined as

$$\alpha_4 = 2\xi^4\Upsilon + 4\xi^4(\xi^2+\eta^2)\Sigma \tag{2.156}$$

Combining the relations for the stress components and the Christoffel symbols yields the displacement equations of motion,

$$\begin{aligned} \alpha_4\left(\frac{\partial^2 u}{\partial R^2}+\frac{1}{R}\frac{\partial u}{\partial R}-\frac{u}{R^2}\right)+(\alpha_3+\tau)\frac{\partial^2 u}{\partial Z^2}+(\alpha_1+\alpha_3)\frac{\partial^2 w}{\partial R\partial Z} &= \varrho\ddot{u} \\ (\alpha_1+\alpha_3)\left(\frac{\partial^2 u}{\partial R\partial Z}+\frac{1}{R}\frac{\partial u}{\partial Z}\right)+\alpha_3\left(\frac{\partial^2 w}{\partial R^2}+\frac{1}{R}\frac{\partial w}{\partial R}\right)+(\alpha_2+2\tau)\frac{\partial^2 w}{\partial Z^2} &= \varrho\ddot{w} \end{aligned} \tag{2.157}$$

At this point, the assumption of harmonic longitudinal GWs in an infinite rod is applied. Practically, the rod is infinite in the sense that reflection from the ends of a finite-length rod are not modeled. Displacement components for the harmonic GWs may be expressed in terms of unknown modeshapes U, W in the radial direction as [69]

$$\begin{aligned} u &= U(R)\exp[\mathrm{i}(KZ-\omega t)] \\ w &= W(R)\exp[\mathrm{i}(KZ-\omega t)] \end{aligned} \tag{2.158}$$

where emphasis is placed on the fact that the modeshapes are only functions of the radial coordinate. From the above forms, the displacement equations of motion are reduced to ordinary differential equations in R,

$$\begin{aligned} \frac{\mathrm{d}^2 U}{\mathrm{d}R^2}+\frac{1}{R}\frac{\mathrm{d}U}{\mathrm{d}R}+\left(\chi_1^2-\frac{1}{R^2}\right)U+\beta_1\frac{\mathrm{d}W}{\mathrm{d}R} &= 0 \\ \beta_2\left(\frac{\mathrm{d}U}{\mathrm{d}R}+\frac{U}{R}\right)+\frac{\mathrm{d}^2 W}{\mathrm{d}R^2}+\frac{1}{R}\frac{\mathrm{d}W}{\mathrm{d}R}+\chi_2^2 W &= 0 \end{aligned} \tag{2.159}$$

Here, χ_1, χ_2 are wavenumber-like terms defined as

$$\begin{aligned}\chi_1^2 &= (\omega^2 - C_{\mathrm{s}}^2 K^2)\frac{\varrho}{\alpha_4} \\ \chi_2^2 &= (\omega^2 - C_{\mathrm{l}}^2 K^2)\frac{\varrho}{\alpha_3}\end{aligned} \tag{2.160}$$

In addition, the wavenumber-like terms β_1, β_2 are defined as

$$\begin{aligned}\beta_1 &= \mathrm{i}K\frac{\alpha_1 + \alpha_3}{\alpha_4} \\ \beta_2 &= \mathrm{i}K\frac{\alpha_1 + \alpha_3}{\alpha_3}\end{aligned} \tag{2.161}$$

Based on the form of the ordinary differential equations, modeshape solutions are assumed in the following form [69]:

$$\begin{aligned}U &= J_1(\Gamma R) \\ W &= \Xi J_0(\Gamma R)\end{aligned} \tag{2.162}$$

where Ξ is a scaling factor, and Γ is a wavenumber-like term in the R coordinate. Substitution of the above modeshapes yields the pair of solutions Ξ_1, Ξ_2 for the factor Ξ,

$$\begin{aligned}\Xi_1 &= \frac{\chi_1^2 - \Gamma_1^2}{\beta_1 \Gamma_1} \\ \Xi_2 &= \frac{\chi_1^2 - \Gamma_2^2}{\beta_1 \Gamma_2}\end{aligned} \tag{2.163}$$

with the solutions Γ_1, Γ_2 for the wavenumber-like term Γ expressed as

$$\begin{aligned}\Gamma_1^2 &= \tfrac{1}{2}(\chi_1^2 + \chi_2^2 - \beta_1\beta_2) + \tfrac{1}{2}\sqrt{(\beta_1\beta_2 - \chi_1^2 - \chi_2^2)^2 - 4\chi_1^2\chi_2^2} \\ \Gamma_2^2 &= \tfrac{1}{2}(\chi_1^2 + \chi_2^2 - \beta_1\beta_2) - \tfrac{1}{2}\sqrt{(\beta_1\beta_2 - \chi_1^2 - \chi_2^2)^2 - 4\chi_1^2\chi_2^2}\end{aligned} \tag{2.164}$$

The general modeshape solutions may then be expressed in terms of two arbitrary scaling factors B_1, B_2,

$$
\begin{aligned}
U &= B_1 J_1(\Gamma_1 R) + B_2 J_1(\Gamma_2 R) \\
W &= \Xi_1 B_1 J_0(\Gamma_1 R) + \Xi_2 B_2 J_0(\Gamma_2 R)
\end{aligned}
\tag{2.165}
$$

9.2.1 Boundary conditions

The boundary conditions for the rod are stress-free surfaces. That is, the incremental stress vector $\mathbf{t}'$ must vanish at the rod surface, located at $\mathbf{R} = A\mathbf{G}_1$ in the predeformed body. Using Eq. (2.92), this condition may be written in terms of the stress tensor σ'^{ij} as

$$
\Big[n_i \sigma'^{ij} \Big]_{R=A} = 0 \tag{2.166}
$$

The surface of the rod has unit normal $\mathbf{n} = \mathbf{G}^1$, and therefore $n_i = \delta_{i1}$. It may be seen that for the considered type of motion $\sigma'^{1i} = \tau'^{1i}$. These conditions then yield ordinary differential equations in R for the modeshapes U, W,

$$
\begin{aligned}
\left[\alpha_4 \frac{\mathrm{d}U}{\mathrm{d}R} + (\alpha_4 + 2\xi^4 \Psi + 2\Pi) \frac{U}{R} + \mathrm{i} K \alpha_1 W \right]_{R=A} &= 0 \\
\left[\mathrm{i} K U + \frac{\mathrm{d}W}{\mathrm{d}R} \right]_{R=A} &= 0
\end{aligned}
\tag{2.167}
$$

Substituting the modeshape forms from Eq. (2.165) into the above yields a system of equations in the following form:

$$
\begin{bmatrix} M_{11} & M_{12} \\ M_{21} & M_{22} \end{bmatrix} \begin{bmatrix} B_1 \\ B_2 \end{bmatrix} = \begin{bmatrix} 0 \\ 0 \end{bmatrix} \tag{2.168}
$$

where the matrix components $M_{11}, M_{12}, M_{21}, M_{22}$ are defined as

$$
\begin{aligned}
M_{11} &= (\alpha_4\Gamma_1 + \mathrm{i}K\alpha_1\Xi_1)J_0(\Gamma_1 A) + \frac{2}{A}(\xi^4\Psi + \Pi)J_1(\Gamma_1 A) \\
M_{12} &= (\alpha_4\Gamma_2 + \mathrm{i}K\alpha_1\Xi_2)J_0(\Gamma_2 A) + \frac{2}{A}(\xi^4\Psi + \Pi)J_1(\Gamma_2 A) \\
M_{21} &= (\mathrm{i}K - \Gamma_1\Xi_1)J_1(\Gamma_1 A) \\
M_{22} &= (\mathrm{i}K - \Gamma_2\Xi_2)J_1(\Gamma_2 A)
\end{aligned}
\tag{2.169}
$$

For nontrivial coefficients B_1, B_2, the determinant of the matrix must vanish. Enforcing this condition yields the dispersion equation for longitudinal GWs in an axially stressed rod,

$$
\begin{aligned}
&(\mathrm{i}K - \Gamma_2\Xi_2)(\alpha_4\Gamma_1 + \mathrm{i}K\alpha_1\Xi_1)J_0(\Gamma_1 A)J_1(\Gamma_2 A) \\
-&(\mathrm{i}K - \Gamma_1\Xi_1)(\alpha_4\Gamma_2 + \mathrm{i}K\alpha_1\Xi_2)J_1(\Gamma_1 A)J_0(\Gamma_2 A) \\
+&\frac{2}{A}(\xi^4\Psi + \Pi)(\Gamma_1\Xi_1 - \Gamma_2\Xi_2)J_1(\Gamma_1 A)J_1(\Gamma_2 A) = 0
\end{aligned}
\tag{2.170}
$$

It may be seen that the above form is similar to the Pochhammer-Chree dispersion equation for longitudinal GWs in an undeformed rod [88]. This equation may be satisfied by certain pairs of angular frequency ω and wavenumber K. However, solving such a dispersion equation for (ω, K) pairs requires implementing an algorithm such as the root-finding approach [89]. Alternatively, a numerical approach based on spectral methods was presented by the author in [63].[††] This achieves fast and accurate solutions, with spectral methods possessing the fastest convergence rate among numerical methods [90].

Having solved for solutions in frequency-wavenumber space, the phase and group velocity of the longitudinal modes referenced to the predeformed body may be obtained as

$$
C_\mathrm{p} = \frac{\omega}{K} \qquad C_\mathrm{g} = \frac{\mathrm{d}\omega}{\mathrm{d}K} \tag{2.171}
$$

[††] There is a typo in the appendix of this conference proceeding. The term β_2 appearing the equations for γ_3, γ_4, and η_2 should be replaced with β_3.

Unlike the bulk waves studied in Sec. 8, the velocity of GWs is frequency dependent, necessitating the distinction between phase and group velocity. The phase velocity describes speed of a wavefront, while the group velocity describes the speed of the energy carried by a wave [91].

In addition to the phase and group velocities, the modeshape coefficients B_1, B_2 may also be found from the (ω, K) solutions. However, since these coefficients are components of an eigenvector, they can only be found up to an arbitrary scale factor. Therefore, in order to avoid possible issues of dividing by zero, the first coefficient B_1 is voluntarily taken as

$$B_1 = \beta_1\Gamma_1\Gamma_2(\mathrm{i}K\beta_1 - \chi_1^2 - \Gamma_2^2)J_1(\Gamma_2 A) \tag{2.172}$$

For the second coefficient, this construction yields

$$B_2 = -\beta_1\Gamma_1\Gamma_2(\mathrm{i}K\beta_1 - \chi_1^2 - \Gamma_1^2)J_1(\Gamma_1 A) \tag{2.173}$$

These coefficients lead to the following modeshapes:

$$\begin{aligned} U = {} & \beta_1\Gamma_1\Gamma_2(\mathrm{i}K\beta_1 - \chi_1^2 - \Gamma_2^2)J_1(\Gamma_2 A)J_1(\Gamma_1 R) \\ & - \beta_1\Gamma_1\Gamma_2(\mathrm{i}K\beta_1 - \chi_1^2 - \Gamma_1^2)J_1(\Gamma_1 A)J_1(\Gamma_2 R) \\ W = {} & \Gamma_2(\chi_1^2 - \Gamma_1^2)(\mathrm{i}K\beta_1 - \chi_1^2 - \Gamma_2^2)J_1(\Gamma_2 A)J_0(\Gamma_1 R) \\ & - \Gamma_1(\chi_1^2 - \Gamma_2^2)(\mathrm{i}K\beta_1 - \chi_1^2 - \Gamma_1^2)J_1(\Gamma_1 A)J_0(\Gamma_2 R) \end{aligned} \tag{2.174}$$

For convenience, the GWs may also be described in terms of the undeformed body. To this end, a change of coordinates in the radial and axial directions may be introduced using $R = \xi r$ and $Z = \eta z$. Defining the wavenumber referenced to the undeformed body as

$$k = \eta K \tag{2.175}$$

the incremental displacements may then be written as

$$\begin{aligned} u &= U(r)\exp[\mathrm{i}(kz-\omega t)] \\ w &= W(r)\exp[\mathrm{i}(kz-\omega t)] \end{aligned} \tag{2.176}$$

where the dependence on the undeformed radial coordinate is emphasized, and the modeshapes are now

$$\begin{aligned} U(r) &= \beta_1\Gamma_1\Gamma_2(\mathrm{i}K\beta_1-\chi_1^2-\Gamma_2^2)J_1(\gamma_2 a)J_1(\gamma_1 r) \\ &\quad -\beta_1\Gamma_1\Gamma_2(\mathrm{i}K\beta_1-\chi_1^2-\Gamma_1^2)J_1(\gamma_1 a)J_1(\gamma_2 r) \\ W(r) &= \Gamma_2(\chi_1^2-\Gamma_1^2)(\mathrm{i}K\beta_1-\chi_1^2-\Gamma_2^2)J_1(\gamma_2 a)J_0(\gamma_1 r) \\ &\quad -\Gamma_1(\chi_1^2-\Gamma_2^2)(\mathrm{i}K\beta_1-\chi_1^2-\Gamma_1^2)J_1(\gamma_1 a)J_0(\gamma_2 r) \end{aligned} \tag{2.177}$$

with $\gamma_1 = \xi\Gamma_1$ and $\gamma_2 = \xi\Gamma_2$, and $a = A/\xi$ denoting the undeformed radius of the rod. The phase and group velocity referenced to the undeformed body may also be obtained through the change of coordinates as

$$c_\mathrm{p} = \frac{\omega}{k} \qquad c_\mathrm{g} = \frac{\mathrm{d}\omega}{\mathrm{d}k} \tag{2.178}$$

To first-order, these are related to the velocities referenced to the predeformed body as $C_\mathrm{p} = \eta c_\mathrm{p}$ and $C_\mathrm{g} = \eta c_\mathrm{g}$, respectively.

9.3 Longitudinal guided wave modes

Figure 2.8 shows the angular frequency and wavenumber solutions to the longitudinal mode dispersion equation. In particular, solutions are shown for the special case of zero axial stress ($\tau = 0$) in a steel rod (representative of the core wire of a strand). The particular steel alloy is taken as Hecla 17, since it has a similar Carbon content to the alloy used in strands, as well as the fact that its second- and third-order elastic constants are available in the literature [92] (see Table 2.1). For convenience, the

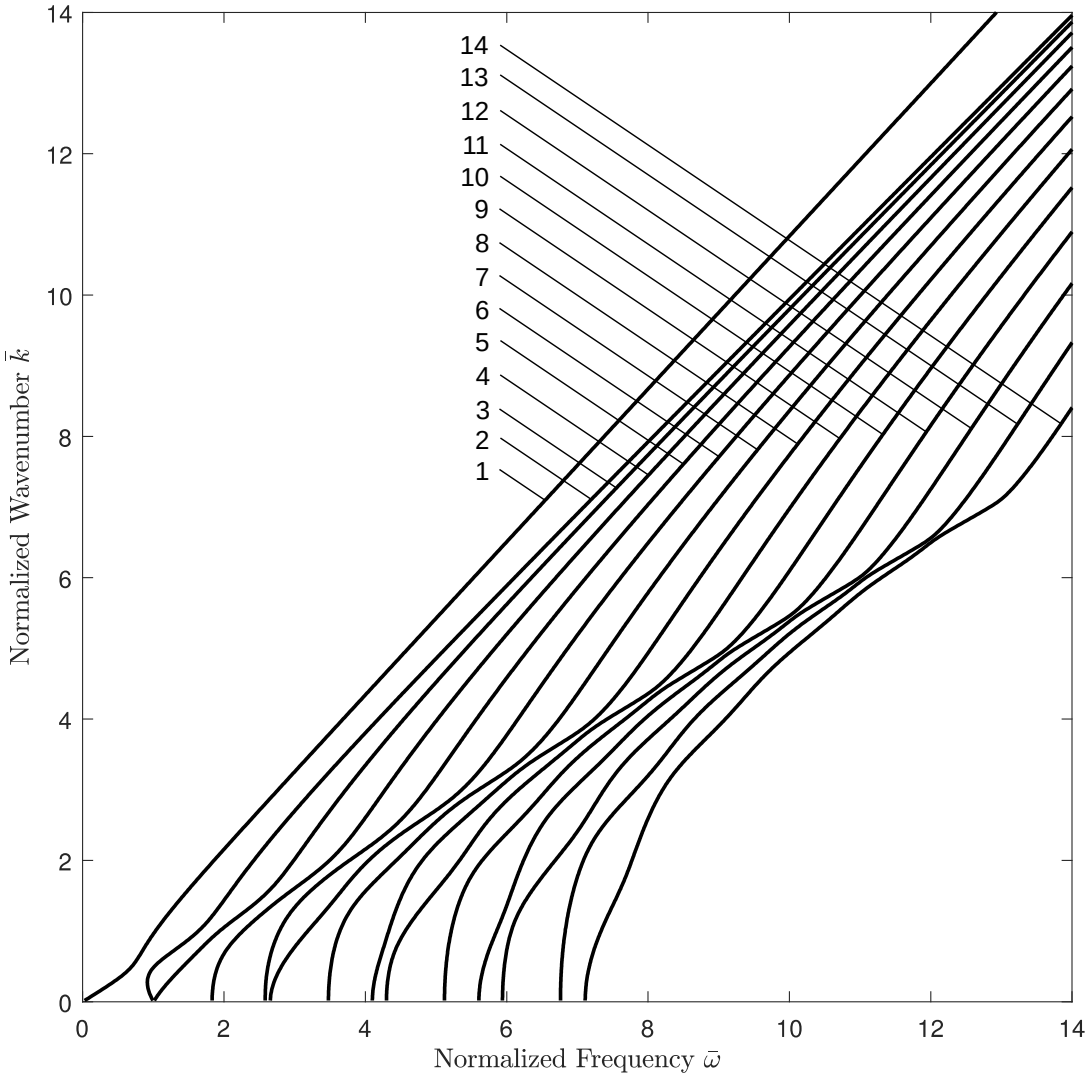

Fig. 2.8 Frequency-wavenumber dispersion curves for longitudinal guided wave modes $\mathrm{L}(0, m)$ in an unstressed steel rod with radius a, with mode numbers m indicated.

Table 2.1 Material properties for steel.

Parameter	Value
ρ	7825 kg/m^3
λ	110.5 GPa
μ	82.0 GPa
l	-328 GPa
m	-595 GPa
n	-668 GPa

solutions are plotted against a normalized frequency and wavenumber. The solutions may then apply to a Hecla 17 steel rod of arbitrary radius. The normalization is performed here along the lines of [93], as $\bar{k} = ka/\zeta$ and $\bar{\omega} = \omega a/\zeta c_{\mathrm{s}0}$, where $\zeta = 3.832\ldots$ is the first nonzero root of $J_1(\cdot)$. This normalized frequency is related to the commonly-used frequency-diameter (fd) as $fd = \zeta c_{\mathrm{s}0}\bar{\omega}/\pi$.

It may be seen from Fig. 2.8 that the solutions exist as a series of modes, with the angular frequency and wavenumber solutions of an individual mode represented by one of the curves shown in the figure. For this reason, the solutions are referred to as *dispersion curves*. Following convention [94], the longitudinal GW modes are indicated by their mode number m as L$(0, m)$. The zero here indicates that these modes are axisymmetric, with a circumferential order of zero. For simplicity, the figure under consideration shows dispersion curves for all modes up to L(0,14). The fundamental mode L(0,1) is the only mode which exists for all frequencies. Each of the higher-order modes L(0,1), L(0,2), ... have a cutoff frequency, which is defined as the frequency at which their wavenumber tends to zero. Due to the adopted normalization, the normalized cutoff frequency for the L(0,1) mode is unity.

Aside from the wavenumber, it also useful to visualize GW modes in terms of phase and group velocity. Along these lines, Fig. 2.9 shows the normalized phase and group velocity dispersion curves for an unstressed steel rod. Here, the velocities are normalized against the bulk longitudinal velocity as $\bar{c}_{\mathrm{p}} = c_{\mathrm{p}}/c_{\mathrm{l}0}$ and $\bar{c}_{\mathrm{g}} = c_{\mathrm{g}}/c_{\mathrm{l}0}$. For low frequencies, it may be seen that the fundamental mode becomes non-dispersive, with phase and group velocity tending to the *bar* velocity $c_{\mathrm{b}0}$ of [88, p. 472]

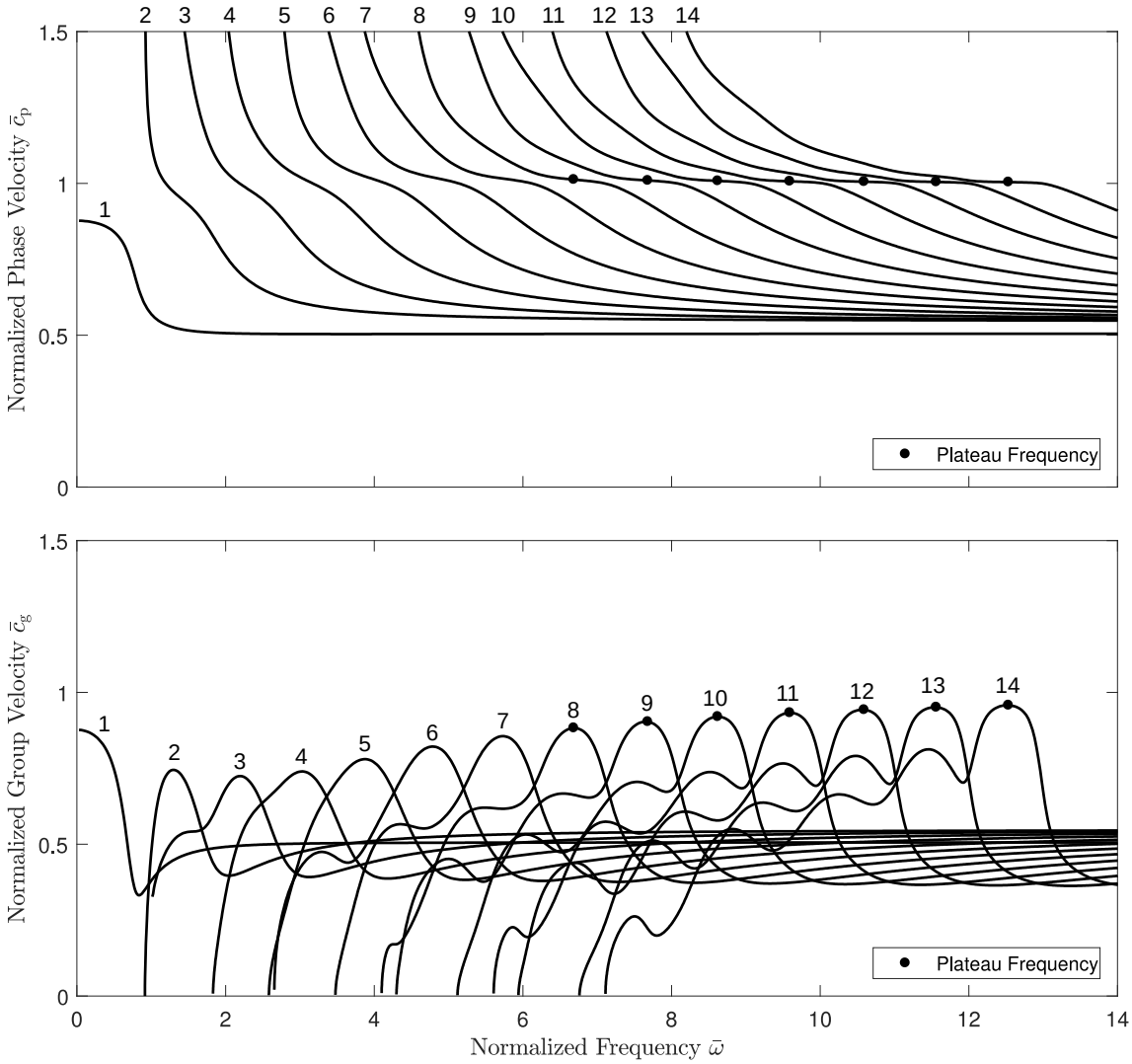

Fig. 2.9 Phase and group velocity dispersion curves for longitudinal guided wave modes in an undeformed steel rod with radius a.

$$\rho c_{\mathrm{b0}}^2 = E \tag{2.179}$$

The fundamental mode also becomes non-dispersive for large frequencies. In this limit the motion concentrates toward the surface, and the phase and group velocity tend to the Rayleigh velocity c_{r0} [88, p. 326]

$$c_{\mathrm{r0}} \approx \frac{0.87 + 1.12\nu}{1 + \nu} c_{\mathrm{s0}} \tag{2.180}$$

Higher-order modes, on the other hand, become highly dispersive toward their low-frequency limits. This causes their phase velocity to tend to infinity, while their group velocity tends to zero. On the contrary, for large frequencies they become non-dispersive, with their phase and group velocity tending to the bulk shear velocity. Interestingly, there is an intermediate frequency at which sufficiently high order modes (roughly L(0,8) and above) become relatively non-dispersive. Inspecting Fig. 2.9(a), it may be seen that this occurs when the phase velocity approaches the bulk longitudinal velocity, yielding a non-dispersive plateauing behavior. This behavior is the same as that which was observed by Mindlin [95] and Tolstoy and Usdin [96]. For this reason, such frequencies are termed *plateau frequencies* [62]. It may also be seen from Fig. 2.9(b) that the group velocity of a higher-order mode reaches its maximum at the plateau frequency. As the mode number increases, the phase and group velocity at the plateau frequency tend to the bulk longitudinal velocity. The asymptote is approached faster for the phase velocity, where less than 1% deviation is reached by L(0,9); the group velocity asymptote only achieves less than 5% deviation by L(0,14). Aside from the beneficial properties of low dispersion and maximal group velocity, it has also been found that the higher-order modes reach their respective attenuation minima at their plateau frequency [97]. This applies when attenuation sources include material damping and energy leakage, such as when a rod is surrounded by another medium (*e.g.*, peripheral strand wires or concrete). In this case,

Table 2.2 Plateau frequencies for various higher-order modes in terms of frequency-diameter *fd* [MHz-mm] and normalized frequency $\bar{\omega}$.

Mode	*fd*	$\bar{\omega}$
L(0,7)	22.6	5.73
L(0,8)	26.4	6.69
L(0,9)	30.2	7.65
L(0,10)	34.0	8.62
L(0,11)	37.9	9.59
L(0,12)	41.7	10.6
L(0,13)	45.6	11.5
L(0,14)	49.4	12.5

the higher-order modes minimize energy leakage at the plateau frequencies due to the core-seeking nature of their modeshapes. For reference, the plateau frequencies for various higher-order modes are listed in Table. 2.2.

Fig. 2.10 shows the modeshapes of various longitudinal modes, including L(0,1), L(0,7), and L(0,13) at $\bar{\omega} = 0.177$, 5.73, and 11.6 (0.70, 4.33, and 8.80 MHz-mm), respectively. These correspond to the low-frequency region of the fundamental mode and the plateau frequencies of L(0,7) and L(0,13). Here, the modeshapes are visualized in terms of the displacement field across the rod axis and diameter, as well as the kinetic energy density across the diameter. The time-averaged kinetic energy density modeshape $\mathscr{K}$ may be obtained from the displacement modeshapes as [98]

$$\mathscr{K} = \tfrac{1}{4}\rho\omega^2(UU^* + WW^*) \tag{2.181}$$

where a superscript $*$ denotes the complex conjugate. The displacement field allows the motion of each mode to be visualized, while the kinetic energy density provides a representation of the energy distribution. Indeed, neglecting attenuation, the kinetic energy density is related to the total energy $\mathscr{E}$ according to $\mathscr{E} = 2\mathscr{K}$ [82].

It may be seen that the modeshape for the fundamental mode L(0,1) is relatively global compared to those for the higher-order modes. The fundamental mode will therefore interact with the peripheral wires of a strand and complicate wave mo-

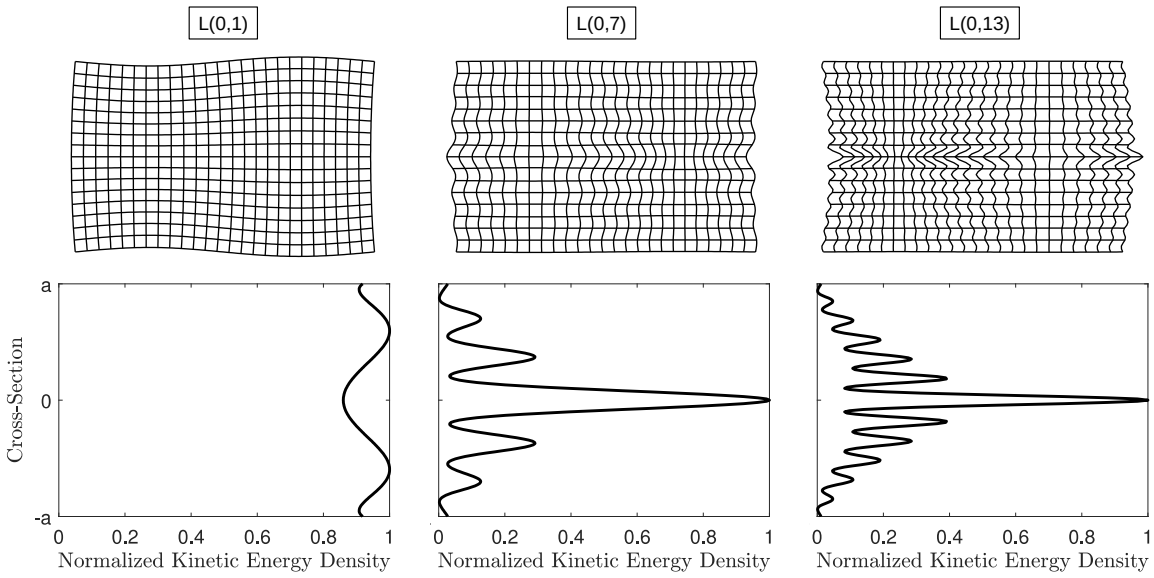

Fig. 2.10 Displacement field and kinetic energy density (KED) modeshapes for selected longitudinal modes in an unstressed steel rod with radius a. Displacement field shown over cross-section and one wavelength for each mode. Results shown for L(0,1), L(0,7), and L(0,13) at $\bar{\omega} = 0.177$, 5.73, and 11.6, respectively.

tion [27]. Regarding the interwire contact stresses described in Sec. 7.1, it is plausible that the more global nature of the fundamental mode also causes these to have a substantial effect on wave propagation [87]. This may partially explain the complicated nonmonotonic stress dependence of this mode, as discussed in the introduction. The higher-order modes L(0,8), L(0,9), ..., however, remain localized near the rod core at their plateau frequencies. These modes therefore have the potential to remain isolated within the core wire of a strand and achieve the idealization of a rod waveguide. In addition, the concentration of wave energy away from the localized contact stresses suggests that nonlinear stress dependence may be suppressed (demonstrated by the author in [61, 62]).

9.3.1 Stress dependence

Since the effect of stress of wave propagation is a relatively small effect, it is convenient to visualize it in terms of the velocity change with respect to an unstressed state. Accordingly, Fig. 2.11 shows the normalized phase and group velocity change

for longitudinal GW modes in a steel rod under an axial stress change $\Delta\tau$. The normalization is taken against the bulk longitudinal velocity change as $\Delta\bar{c}_{\mathrm{p}} = \Delta c_{\mathrm{p}}/\Delta c_{\mathrm{l}}$ and $\Delta\bar{c}_{\mathrm{g}} = \Delta c_{\mathrm{g}}/\Delta c_{\mathrm{l}}$. Since all velocity changes are linear with respect to stress change, the phase and group velocity change may be written in terms of acoustoelastic constants as $\Delta c_{\mathrm{p}} = \kappa_{\mathrm{p}}\Delta\tau$ and $\Delta c_{\mathrm{g}} = \kappa_{\mathrm{g}}\Delta\tau$, as was done for the bulk waves in Sec. 8.2. Therefore, the normalized phase and group velocity changes may also be interpreted as normalized acoustoelastic constants, $\kappa_{\mathrm{p}}/\kappa_{\mathrm{l}}$ and $\kappa_{\mathrm{g}}/\kappa_{\mathrm{l}}$, respectively.

It may be seen that the phase velocity change in Fig. 2.11(a) largely resembles the phase velocity itself. In particular, the areas of relatively low dispersion in Fig. 2.9(a) equate to areas of relatively stable velocity change across frequency in Fig. 2.11(a). This is true at the plateau frequencies of higher-order modes, which are indicated in the figure. Here, the phase velocity change is stable across mode and frequency, as it asymptotes at the phase velocity change for a bulk longitudinal wave. It may also be seen in Fig. 2.11(b) that the group velocity change asymptotes toward the same value at the plateau frequency. When compared to phase velocity, however, this velocity change is less stable within a small neighborhood around the plateau frequency. These results suggest that measuring phase velocity change at the plateau frequency may be a reliable method for determining stress change. Since the velocities considered here are referenced to the undeformed body, the velocity changes account for the elongation effects of the axial stress, in addition to the nonlinear material effects described by the second-order elasticity framework.

With stress change related to phase velocity change, a relation may be formed between stress change and the phase time change Δt in a GW mode. Assuming the phase velocity change is small compared to the reference value c_{p0}, it may be expressed in terms of the phase time change over a propagation length ℓ as [99]

$$\Delta c_{\mathrm{p}} = -\frac{c_{\mathrm{p0}}^2}{\ell}\Delta t \tag{2.182}$$

where the length is referenced to the undeformed body. The stress change may then

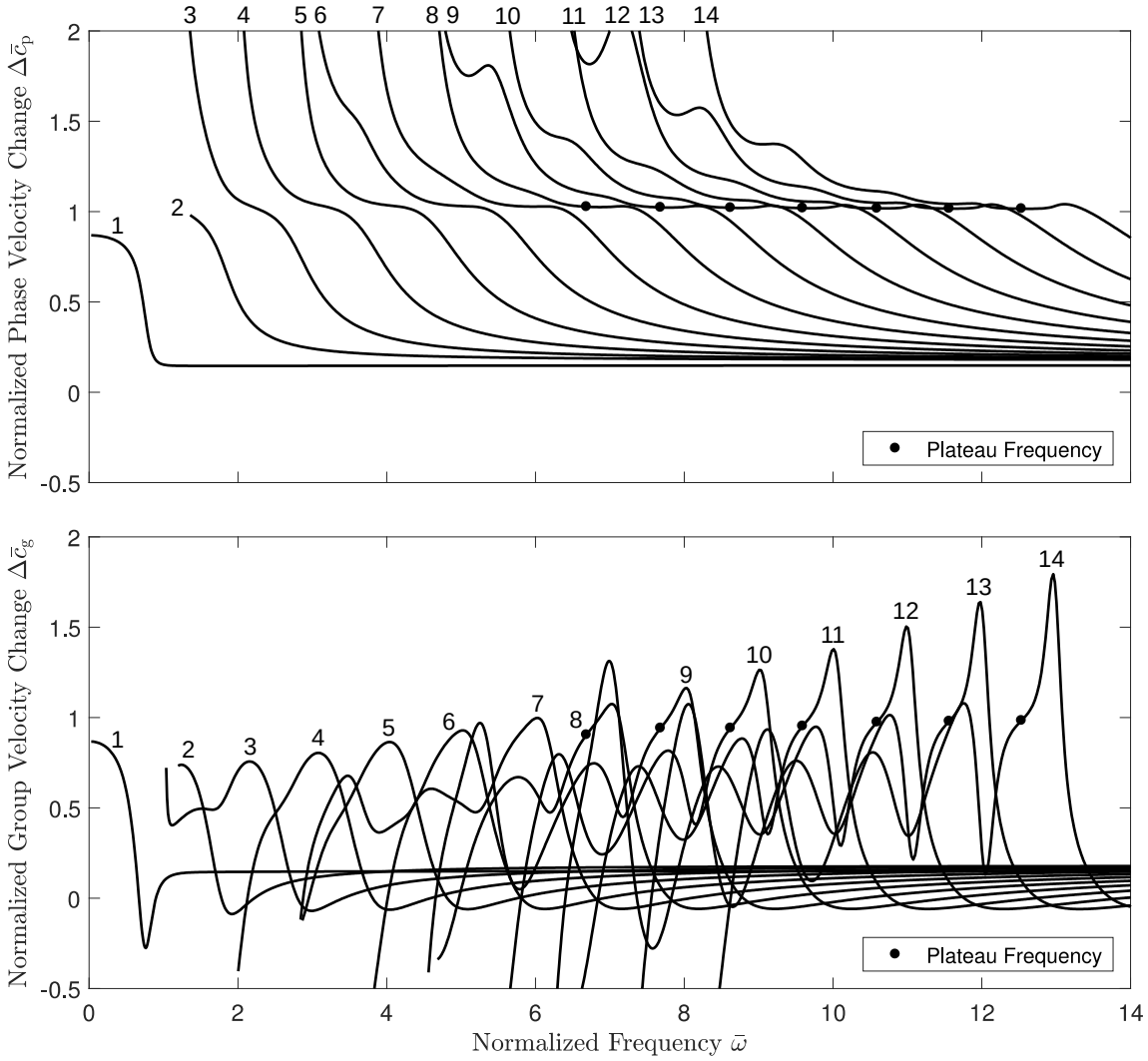

Fig. 2.11 Normalized phase and group velocity changes, $\Delta\bar{c}_p$ and $\Delta\bar{c}_g$, for longitudinal guided wave modes in a steel rod under an axial stress τ.

be expressed as

$$\Delta\tau = -\frac{c_{\mathrm{p}0}^2}{\kappa_{\mathrm{p}}\ell}\Delta t \tag{2.183}$$

CHAPTER 3

Data Processing

Various techniques in the broad area of data processing are described in this chapter.* Those applied to guided waves (GWs) in strands include the wavelet transform, modal modulation, and data fusion. Those applied to acoustic emission (AE) in concrete include the sections on AE feature extraction, topological data analysis (TDA), and hidden Markov models (HMMs).

10 Wavelet Transform

The energy content of GW modes may be visualized through the wavelet transform. It is a time-frequency transform, whose peaks correspond to the arrival times of the energy from various modes in a signal. These arrival times are therefore associated with the group velocities of the modes.

The wavelet transform $\mathcal{W}\{\cdot\}$ is computed through the convolution of a signal s and a mother wavelet ψ as [100]

$$\mathcal{W}\{s\} = \tilde{s}(p,q) = \frac{1}{\sqrt{p}} \int_{-\infty}^{\infty} s(t)\psi^* \left(\frac{t-q}{p} \right) \mathrm{d}t \tag{3.1}$$

where $\tilde{s}$ denotes the wavelet transform of a signal s, p and q are scale and shift parameters, and a superscript $*$ denotes complex conjugate. The Gabor mother

* This chapter is derived in part from the author's work in [62, 64–67].

wavelet is adopted here, since it achieves the greatest time-frequency resolution [100]. It may be described in terms of two user-specified parameters ϖ, ς as [101]

$$\psi(t) = \left(\frac{\varpi^2}{\pi\varsigma^2}\right)^{1/4} \exp\left(\mathrm{i}\varpi t - \frac{\varpi^2}{\varsigma^2}\frac{t^2}{2}\right) \tag{3.2}$$

The center frequency parameter ϖ is related to the scale parameter as $p = \varpi/\omega$. For simplicity, ϖ may be set to 2π, in order for $1/p$ to reduce to the frequency [101]. The selection of the ς parameter involves a trade-off between time and frequency resolution, with higher and lower values increasing the resolution in time and frequency, respectively. However, it is important to choose $\varsigma^2 \gg 1$ in order to ensure that the mother wavelet is nearly analytic [100]. Using the Gabor mother wavelet, the wavelet transform may be written as a function of time and angular frequency as

$$\tilde{s}(t,\omega) = \sqrt{\frac{\omega}{\varpi}} \int_{-\infty}^{\infty} s(\tau)\psi^*\left(\frac{\tau - t}{\varpi/\omega}\right)\mathrm{d}\tau \tag{3.3}$$

where τ is a dummy variable.

The time-frequency resolution may be further studied by considering the energy spread of the mother wavelet. The spread may be characterized in t-ω space for the Gabor mother wavelet through the following variance-like terms [100]:

$$\begin{aligned} \sigma_{\mathrm{t}}^2 &= \frac{\varpi^2}{\omega^2} \int_{-\infty}^{\infty} t^2 |\psi(t)|^2 \mathrm{d}t \\ \sigma_{\omega}^2 &= \frac{\omega^2}{2\pi\varpi^2} \int_{-\infty}^{\infty} (u - \varpi)^2 |\hat{\psi}(u)|^2 \mathrm{d}u \end{aligned} \tag{3.4}$$

where u is a dummy variable, and $\hat{\psi} = \mathcal{F}\{\psi\}$ is the Fourier transform of the mother wavelet, with the Fourier transform of some signal s defined as

$$\mathcal{F}\{s\} = \hat{s}(\omega) = \int_{-\infty}^{\infty} s(t)\mathrm{e}^{-\mathrm{i}\omega t}\mathrm{d}t \tag{3.5}$$

Since the mother wavelet is centered in time, the time integrand for σ_{t} does not

require a mean substraction. This is in contrast to the mean subtraction using the center frequency ϖ in the frequency integrand. From these definitions, higher values of σ_{t} or σ_{ω}, respectively, correspond to larger energy spread in time or frequency. The above integration may be performed to yield

$$\sigma_{\mathrm{t}} = \frac{1}{\sqrt{2}} \frac{\varsigma}{\omega} \qquad \sigma_{\omega} = \frac{1}{\sqrt{2}} \frac{\omega}{\varsigma} \tag{3.6}$$

It may be seen that the time and frequency resolutions are only a function of one of the wavelet parameters, namely ς. The parameter ς may therefore be selected by specifying either the desired time or frequency resolution at a given angular frequency ω. Lastly, it may be seen that $\sigma_{\mathrm{t}}\sigma_{\omega} = \frac{1}{2}$. This is greatest resolution achievable [100], and supports the use of the Gabor mother wavelet.

Aside from visualizing guided wave arrivals, the wavelet transform may also be used as a narrowband filter. The signal filtered at a given center frequency $f_{\mathrm{c}} = \omega_{\mathrm{c}}/2\pi$ may be obtained from the real part of the wavelet transform at that frequency,

$$s_{\mathrm{c}}(t) = \Re\{\tilde{s}(t, \omega_{\mathrm{c}})\} \tag{3.7}$$

where $\Re\{\cdot\}$ denotes the real part.

11 Modal Modulation

A practical difficulty of implementing higher-order modes for stress monitoring is that the measurement of phase velocity is sensitive to artificial phase shifts. Such shifts may be due to sensor reattachment or replacement, for instance. In order to eliminate such sensitivity, a technique called modal modulation is proposed. The main idea is to form a modulated wave through the superposition of two higher-order modes, thus canceling out any phase shift.

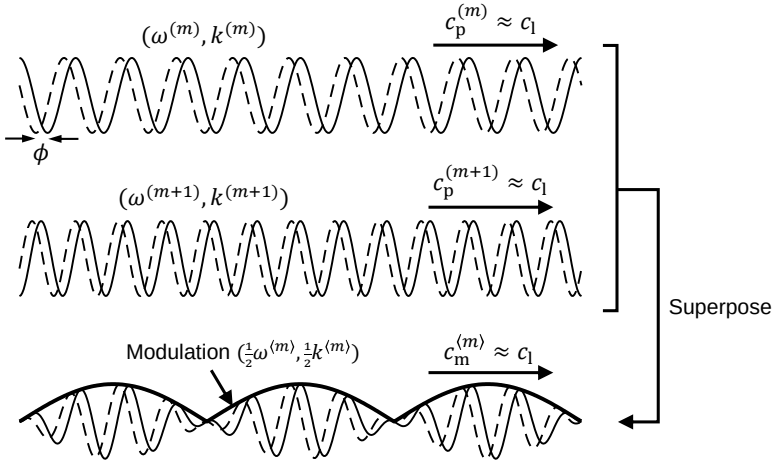

Fig. 3.1 Superposition of two harmonic higher-order modes L(0,m) and L(0,$m+1$) to form a modulated wave. Phase velocities $c^{(m)}, c^{(m+1)}$ overlain, along with modulation velocity $c^{\langle m \rangle}$. Cases overlain for no phase shift (solid) and phase shift (dashed), showing no influence from phase shift on modulation.

Let the displacements $u^{(m)}$ and $u^{(m+1)}$ of two consecutive higher-order modes recorded by a sensor at an axial position z be

$$\begin{aligned} u^{(m)} &= \exp[\mathrm{i}(k^{(m)}z - \omega^{(m)}t + \phi)] \\ u^{(m+1)} &= \exp[\mathrm{i}(k^{(m+1)}z - \omega^{(m+1)}t + \phi)] \end{aligned} \tag{3.8}$$

where $\omega^{(m)}$ and $k^{(m)}$ are the angular frequency and wavenumber of the m-th longitudinal GW mode at its plateau frequency, and ϕ is the artificial phase shift to be eliminated. Without loss of generality, the above displacements may be taken as either the radial or axial components. However, for simplicity, it is assumed that each component has been normalized to a unit amplitude. If the phase shift varies while stress is also changing (*e.g.*, due to sensor replacement during the course of monitoring), error will be introduced into the time change measurement. However, this error may be eliminated by superposing the two modes in the manner which follows.

First, denote the angular frequency and wavenumber differences between two adjacent modes as $\omega^{\langle m \rangle} = \omega^{(m+1)} - \omega^{(m)}$ and $k^{\langle m \rangle} = k^{(m+1)} - k^{(m)}$. Here, the index m within angled brackets $\langle \cdot \rangle$ corresponds to the m-th mode pair m-($m+1$). The

superposition of the two modes in Eq. (3.8) then yields

$$u^{(m)}+u^{(m+1)} = 2\underbrace{\cos\left(\frac{k^{\langle m\rangle}}{2}z-\frac{\omega^{\langle m\rangle}}{2}t\right)}_{\text{modulation}}\underbrace{\exp\left[\mathrm{i}\left(\frac{k^{(m)}+k^{(m+1)}}{2}z-\frac{\omega^{(m)}+\omega^{(m+1)}}{2}t+\phi\right)\right]}_{\text{phase}} \tag{3.9}$$

which is composed of a modulation (cosine) and a phase (exponential) term. As opposed to the phase term, it may be seen that the modulation is not influenced by the phase shift ϕ. The modulation term may be extracted by obtaining the envelope of the above as

$$\left|\cos\left(\frac{k^{\langle m\rangle}}{2}z-\frac{\omega^{\langle m\rangle}}{2}t\right)\right| = \tfrac{1}{2}\mathcal{E}\{u^{(m)}+u^{(m+1)}\} \tag{3.10}$$

where $\mathcal{E}\{\cdot\}$ computes the envelope of a wave according to

$$\mathcal{E}\{\cdot\} = |\cdot+\mathrm{i}\mathcal{H}\{\cdot\}| \tag{3.11}$$

with $\mathcal{H}\{\cdot\}$ denoting the Hilbert transform, defined as

$$\mathcal{H}\{s\} = \frac{1}{\pi}\int_{-\infty}^{\infty}\frac{s(\tau)}{t-\tau}\mathrm{d}\tau \tag{3.12}$$

where τ is a dummy variable. Figure 3.1 illustrates the extraction of the modulation term from the superposition of two harmonic waves, demonstrating the insensitivity to phase shift.

Since higher-order modes asymptote to the bulk longitudinal velocity at the plateau frequencies, the modulated wave propagates at a (unstressed) velocity $c_{\mathrm{m}0}^{\langle m\rangle}$ of

$$c_{\mathrm{m}0}^{\langle m\rangle} = \frac{\omega_0^{\langle m\rangle}}{k_0^{\langle m\rangle}} \approx c_{\mathrm{l}0} \tag{3.13}$$

where a subscript "m" denotes modulation. The change in modulation velocity $\Delta c_{\mathrm{m}}^{\langle m\rangle} = c_{\mathrm{m}}^{\langle m\rangle} - c_{\mathrm{m}0}^{\langle m\rangle}$ due to stress then approximates the bulk velocity change,

$$\Delta c_{\mathrm{m}}^{\langle m \rangle} \approx \kappa_{\mathrm{l}} \Delta\tau \tag{3.14}$$

For L(0,8) and above, the approximations in Eqs. (3.13) and (3.14) are accurate to within 1% error [66]. Therefore, the stress change may be estimated by measuring $\Delta c_{\mathrm{m}}^{\langle m \rangle}$, while using the same acoustoelastic constant κ_{l} as is used for the phase velocity. This involves applying Eq. (2.183), where Δt is measured from the modulation wave of a higher-order mode pair.

12 Data Fusion

The fact that multiple estimations of stress change may be obtained from multiple mode pairs presents the opportunity for combining their information and obtaining more robust estimations. To accomplish this, a data fusion approach is used here to combine the redundant information from various mode pairs into a single stress change estimate. Since the data is commensurate, the fused data may be formed as a weighted combination of the original data. This is an intermediate level of data fusion, known as *feature-level* fusion [102].

Denote the estimate of stress change from the m-th mode pair by $\Delta\tau^{\langle m \rangle}$. Considering the fusion of P pairs, the fused data $\Delta\tau$ is expressed as a weighted combination of the estimates from each pair,

$$\Delta\tau = \sum_{p=m}^{m+P-1} w^{\langle p \rangle} \Delta\tau^{\langle p \rangle} \tag{3.15}$$

where L(0,m) is the lowest-order mode considered, and $w^{\langle m \rangle} \in [0, 1]$ is the weight of the m-th pair. The collection of weights satisfies $\sum_{p=m}^{m+P-1} w^{\langle p \rangle} = 1$, and a two step process is carried out to assign them: (1) assign an initial weight based on the amplitude of the pair; (2) detect outlier pairs and set their weight to zero. Step

1 is based on the assumption that mode pairs with higher amplitude have greater reliability for feature extraction (*i.e.*, stress change estimation). On the other hand, Step 2 involves outlier analysis, where the weight is set to zero for pairs that are classified as outliers.

Outlier classification is performed on the deviation statistic $z^{\langle m \rangle}$ for a given mode pair, defined as [60]

$$z^{\langle m \rangle} = \frac{\Delta\tau^{\langle m \rangle} - \mu^{\langle m \rangle}}{\sigma^{\langle m \rangle}} \tag{3.16}$$

where $\mu^{\langle m \rangle}$ and $\sigma^{\langle m \rangle}$ are the mean and standard deviation of the dataset (specific to the m-th mode pair). These statistics are computed using an exclusive formulation, where data for the m-th pair is excluded (*i.e.*, $\mu^{\langle m \rangle}$ and $\sigma^{\langle m \rangle}$ are found from the data $\Delta\tau^{\langle p \rangle}$ for $p \neq m$). This ensures that the statistics are not influenced by including data for the pair under consideration. A pair is then classified as an outlier if its deviation statistic is larger than two standard deviations,

$$\begin{aligned} |z^{\langle m \rangle}| &\leq 2\sigma^{\langle m \rangle} \quad \text{(non-outlier)} \\ |z^{\langle m \rangle}| &> 2\sigma^{\langle m \rangle} \quad \text{(outlier)} \end{aligned} \tag{3.17}$$

Combining Steps 1 and 2 yields the weight assignment for a given mode pair in terms of the amplitude $A^{\langle m \rangle}$ for that pair,

$$w^{\langle m \rangle} = \begin{cases} \dfrac{A^{\langle m \rangle}}{\sum_{p=m}^{m+P-1} A^{\langle p \rangle}} & \text{(non-outlier)} \\ 0 & \text{(outlier)} \end{cases} \tag{3.18}$$

where $A^{\langle m \rangle} = A^{(m)} + A^{(m+1)}$ is defined as the sum of the two constituent mode amplitudes within the pair. If the pair is detected as an outlier, then $A^{\langle m \rangle}$ is set to zero.

12.1 Uncertainty quantification

One of the primary purposes of data fusion is to decrease uncertainty in the estimated values [102]. This thesis considers estimating stress change over the course of corrosion, with estimates being made at a series of corrosion levels. Therefore, the stress change estimate over the course of corrosion is treated as a normally distributed stochastic process (specifically, a gaussian process). As such, its uncertainty may be quantified using gaussian process regression (GPR) [103]. GPR is a non-parametric regression method which captures the trend and uncertainty in the data by providing a regression (mean) function along with a standard deviation function. The mean function $\mu_{\text{gpr}}(c)$ denotes the stress change at an arbitrary corrosion level c, which has a corresponding uncertainty defined by the standard deviation function $\sigma_{\text{gpr}}(c)$.

Let the stress change data $\Delta\tau_1, \Delta\tau_2, \ldots$ at a series of corrosion levels $c_1, c_2, \ldots$ be denoted by

$$\boldsymbol{\tau} = \begin{bmatrix} \Delta\tau_1 & \Delta\tau_2 & \cdots \end{bmatrix}^{\mathrm{T}} \tag{3.19}$$

where a superscript T denotes transpose. The mean μ_{gpr} and standard deviation σ_{gpr} for the GPR may be computed from the data as follows:

$$\begin{aligned} \mu_{\text{gpr}} &= \boldsymbol{\kappa}^{\mathrm{T}} \mathbf{Q}^{-1} \boldsymbol{\tau} \\ \sigma_{\text{gpr}} &= Q - \boldsymbol{\kappa}^{\mathrm{T}} \mathbf{Q}^{-1} \boldsymbol{\kappa} \end{aligned} \tag{3.20}$$

where $\mathbf{Q}$ is a covariance matrix, Q is the covariance at corrosion level c, and $\boldsymbol{\kappa}$ is a kernel vector measured between the corrosion levels $c_1, c_2, \ldots$ and c. To accommodate noisy measurements, the covariance matrix is defined in terms of a kernel matrix $\mathbf{K}$ and a noise hyperparameter h_{n} as

$$\mathbf{Q} = \mathbf{K} + h_{\text{n}}^2 \mathbf{I} \tag{3.21}$$

The elements $K_{11}, K_{12}, \ldots$ of the kernel matrix are defined from a kernel function κ, which is based on two hyperparameters h_f and h_l,

$$K_{ij} = \kappa(c_i, c_j) = h_\mathrm{f}^2 \exp[-\tfrac{1}{2} h_\mathrm{l}^2 (c_i - c_j)^2] \tag{3.22}$$

The covariance at corrosion level c is then

$$Q = \kappa(c, c) + h_\mathrm{n}^2 \tag{3.23}$$

and the elements of the kernel vector $\boldsymbol{\kappa} = [\kappa_1 \ \kappa_2 \ \cdots]^\mathrm{T}$ are $\kappa_i = \kappa(c_i, c)$.

GPR relies on numerically tuning the hyper-parameters $h_\mathrm{f}, h_\mathrm{l}, h_\mathrm{n}$ in order to maximize the probability of observing the data $\boldsymbol{\tau}$ [103]. The numerical solution is performed here using in-house code based on the simulated annealing optimization algorithm [104].

13 Acoustic Emission Features

To allow for real-time monitoring, AE signals are typically converted to a feature-space representation as they are recorded. This facilitates reduced storage load on a data acquisition (DAQ) system and fast analysis of the signals (otherwise known as hits). Some of the commonly-used AE features are defined below.

Four main AE features are considered in this thesis: (1) AE activity; (2) peak frequency; (3) risetime/amplitude; and (4) average frequency. AE activity and peak frequency are two of the most widely used features for corrosion monitoring. On the other hand, risetime/amplitude and average frequency are widely used in crack monitoring, under the collective term RA/AF analysis [105, 106]. Detailed descriptions of these features are collected below.

- *AE activity.* AE activity is used as a general term for the amount of AE

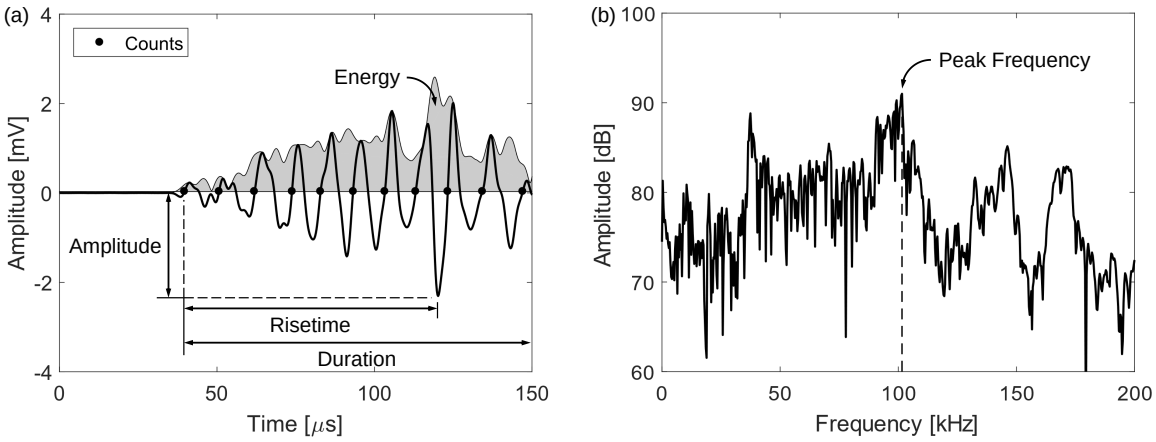

Fig. 3.2 Visualization of features derived from the (a) time history and (b) frequency spectrum of an acoustic emission waveform.

recorded. In this thesis, AE energy and the number of hits are used as two metrics for quantifying activity. In this case, the energy feature is a measure of the area under the envelope of an AE signal, as visualized in Fig. 3.2(a).

- *Peak frequency.* The peak frequency feature, denoted *PF*, is defined as the frequency with the maximum amplitude in a signal, as seen in Fig. 3.2(b). In other words, it may be expressed for an arbitrary signal s as

$$PF = \arg\max_f \{\hat{s}(f)\} \tag{3.24}$$

  This feature is usually expressed in kHz.

- *Risetime/amplitude.* The ratio of risetime and amplitude features is referred to as the risetime/amplitude (*RA*) feature. Here, the risetime *RT* is the length of time between the first threshold crossing and the peak amplitude point in a signal, while the amplitude $AM = \max\{|s|\}$ is the peak amplitude. These may each be seen in Fig. 3.2(a). Accordingly,

$$RA = \frac{RT}{AM} \tag{3.25}$$

  which is often expressed in units of ms/V. In addition, the amplitude is often expressed in decibels, as opposed to linear voltage units. The decibel units are

found with respect to a reference voltage of 1 μV as [107]

$$AM[\text{dB}] = 20\log_{10}\left(\frac{AM[\mu\text{V}]}{1\ \mu\text{V}}\right) - A_{\text{daq}} \tag{3.26}$$

where A_{daq} is the amplification of the DAQ system (expressed in dB).

- *Average frequency.* The average frequency feature, denoted *AF*, is defined as the ratio of two other AE features: counts and duration. Counts (*CO*) is defined as the number of times the signal crossed the threshold, while duration (*DU*) is the length of time that the signal remains above the threshold (see Fig. 3.2(a)). Formally, the average frequency is then defined as the frequency-like quantity

$$AF = \frac{CO}{DU} \tag{3.27}$$

often measured in kHz.

14 Topological Data Analysis

The main idea motivating TDA is that a collection of data points (*i.e.*, a datacloud) has shape, and its shape has meaning [56]. The concept of data having shape (*i.e.*, topology) is illustrated in Fig. 3.3(a) for a 2D datacloud with the topology of an annulus. Indeed, in this example the datacloud consists of 25 points randomly sampled from the annulus outlined in Fig. 3.3(a). It should be noted that a datacloud itself does not directly disclose its topology, since topology is associated with continuous objects (*e.g.*, the outlined annulus). What is therefore required is a sophisticated method of analyzing the datacloud in order to extract its underlying topology.

TDA is designed to meet this purpose by transforming the datacloud into a topological object, from which topological characteristics may be measured. The topological object is constructed by first "viewing" the datacloud at a given scale and then measuring the connectivity between data points at that scale. In TDA, this

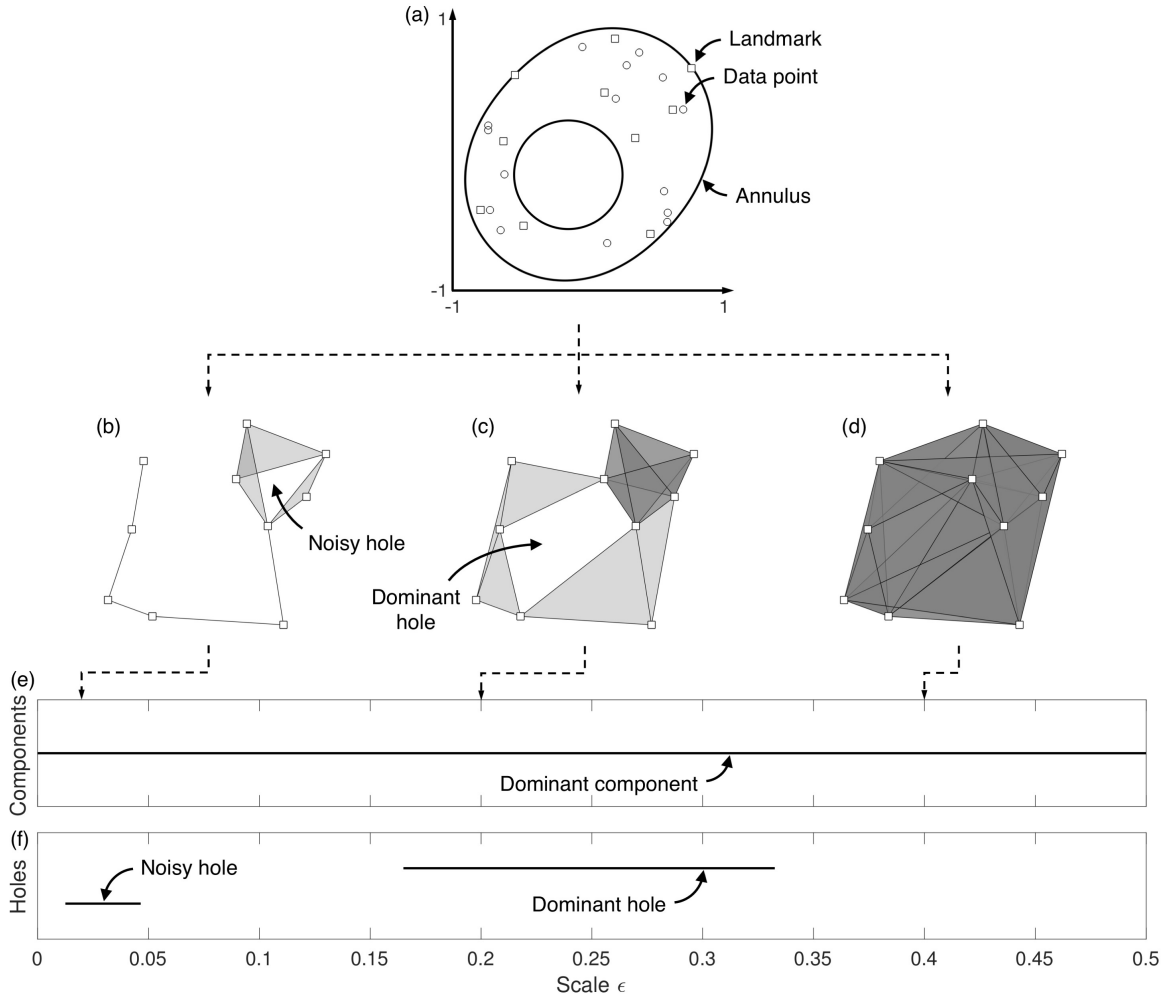

Fig. 3.3 Example of topological data analysis for (a) randomly sampled datacloud from a 2D annulus (one component, one hole) with landmarks indicated by squares. (b)-(d) Witness complexes constructed from landmarks, corresponding to three values of ε (0.02, 0.20, 0.40). Barcodes for number of (e) components and (f) holes, revealing one component and one hole (the true topology of the annulus).

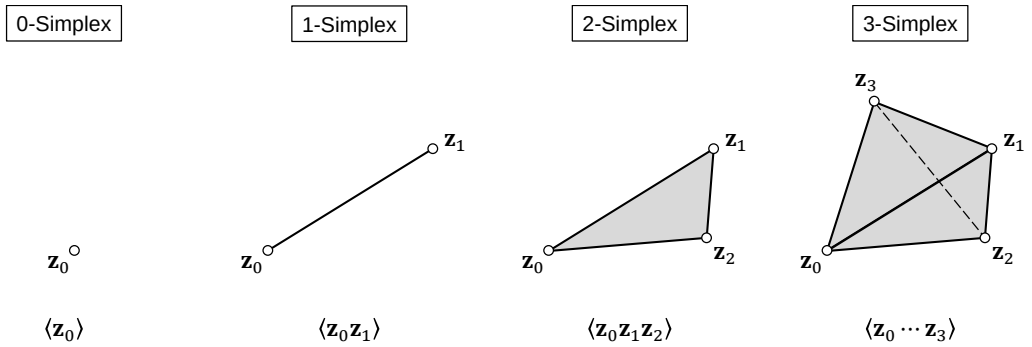

Fig. 3.4 Illustrations of 0-, ..., 3-simplices constructed from arbitrary data points $\mathbf{z}_0, \ldots, \mathbf{z}_3$. Notations for each simplex using angled brackets $\langle \cdot \rangle$ shown underneath.

object comprises a collection of simplices, termed a simplicial complex. Here, an n-D simplex (otherwise known as an n-simplex) is defined as the convex hull of $n+1$ data points [108]. For instance, a 0-simplex is a point, a 1-simplex is a line, a 2-simplex is a triangle, and a 3-simplex is a tetrahedron, with the data points forming the vertices of the simplex in each case. These examples are visualized in Fig. 3.4. Different forms of simplicial complexes may be adopted, such as the Čech and Rips complexes [109]. However, these particular complexes may become computationally expensive for large dataclouds. In such cases, the witness complex serves as a computationally efficient alternative [110].

The witness complex achieves computational efficiency by being constructed on only a small subset of data points, known as *landmarks*. Given a selection of landmarks from a datacloud, a given p-simplex of the witness complex is defined as follows: let the position vectors for a subset of the landmarks be denoted $\mathbf{l}_0, \ldots, \mathbf{l}_p$, and an arbitrary (witness) point in the datacloud be $\mathbf{z}$. Further, denote the distance from the $(p+1)$-th nearest landmark to $\mathbf{z}$ as $d_p(\mathbf{z})$. For a given scale ε, the p-simplex constructed from $\mathbf{l}_0, \ldots, \mathbf{l}_p$ (denoted $\langle \mathbf{l}_0 \cdots \mathbf{l}_p \rangle$) belongs to the witness complex W if there exists a witness point $\mathbf{z}$ satisfying

$$||\mathbf{l}_i - \mathbf{z}||_2 \leq d_p(\mathbf{z}) + \varepsilon \quad \text{for } i = 0, \ \ldots, \ p \tag{3.28}$$

as well as if each of the $(p-1)$-simplices $\langle \mathbf{l}_0 \cdots \breve{\mathbf{l}}_i \cdots \mathbf{l}_p \rangle$, $i = 0, \ldots, p$ belong to W

[111], with a breve $\breve{\cdot}$ indicating that the data point is absent from the simplex. For the special case of $p = 0$, the 0-simplices are the landmarks themselves. Examples of the witness complex applied to the datacloud in Fig. 3.3(a) may be seen in Fig. 3.3(b)-(d), corresponding to three values of ε. For illustration, ten landmarks are selected from the datacloud and are indicated by squares.

It has been suggested that the landmarks be selected using the *maxmin* algorithm [110]. This is opposed to a random selection, which may only retain large-density clusters within the original datacloud. The maxmin algorithm operates as follows [110]: Select the first landmark $\mathbf{l}_0$ at random from the collection of data points $\mathscr{Z}$. Select each subsequent landmark $\mathbf{l}_i$ as that data point which is furthest from the current collection of landmarks $\{\mathbf{l}_0, \ldots, \mathbf{l}_{i-1}\}$. Here, *furthest* is used in the sense that the new landmark is the data point which maximizes the distance to the closest existing landmark. More specifically, select the landmark $\mathbf{l}_i$ according to

$$\mathbf{l}_i = \arg\max_{\mathbf{z}} \Big\{ \min\{||\mathbf{l}_0 - \mathbf{z}||_2, \ldots, ||\mathbf{l}_{i-1} - \mathbf{z}||_2\} \Big\} \qquad \text{for } \mathbf{z} \in \mathscr{Z} \setminus \{\mathbf{l}_0, \ldots, \mathbf{l}_{i-1}\} \quad (3.29)$$

where the notation $\mathscr{X} \setminus \mathscr{Y}$ denotes all those elements in $\mathscr{X}$ which are not in $\mathscr{Y}$. The above process is repeated until the desired number of landmarks is reached. However, it should be noted that the number of landmarks is a user-specified parameter, and there is no definitive optimal value for a given datacloud. In this thesis, an approach for determining this number is proposed based on converging topology of the witness complex.

The witness complexes shown in Fig. 3.3(b)-(d) each provide a topological description of the datacloud at a particular scale ε. However, since there is no single best value of ε, a holistic representation of the datacloud's topology may be obtained by studying the witness complex's topology from small to large scale [112]. Thus, "true" topological characteristics are identified as those that exist over a wide range of scale. Conversely, those which only appear over a brief range of scale may be treated as noise [56]. In the case of an n-D simplicial complex, the relevant topolog-

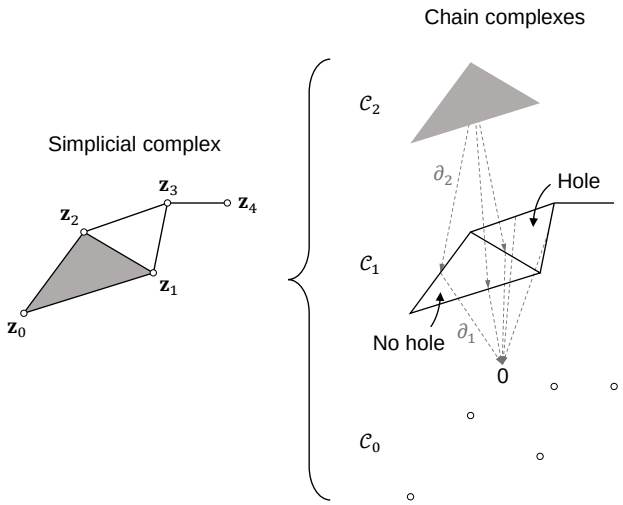

Fig. 3.5 Determining the number of holes (first Betti number) in a simplicial complex using its associated chain complexes $\mathsf{C}_0, \mathsf{C}_1, \mathsf{C}_2$. Certain mappings of the boundary operators ∂_1, ∂_2 are shown as dashed arrows. Only one of the cycles in C_1 has a hole, since the other is "filled in" in C_2.

ical characteristics are the Betti numbers, denoted $\beta_0, \ldots, \beta_{n-1}$, where β_i represents the number of i-D holes in the complex. As special cases, β_0 and β_1 are also termed, respectively, the number of connected components (termed components here) and the number of loops (termed holes here) [56]. For instance, the 2D annulus considered in Fig. 3.3(a) has one component and one hole, as indicated.

Determining the Betti numbers of a simplicial complex (*e.g.*, a witness complex W) involves breaking it up into a series of simpler complexes [108], as visualized in Fig. 3.5. These are termed *chain complexes*, denoted $\mathsf{C}_0, \ldots, \mathsf{C}_n$. These are constructed so that C_i contains only the i-simplices in W. The chain complexes then have boundary operators $\partial_0, \ldots, \partial_n$, which map elements in one complex to those in the next lowest dimension. This mapping operates as follows: for a given i-simplex $\langle \mathbf{z}_0 \cdots \mathbf{z}_i \rangle$ in C_i, the boundary operator ∂_i yields a linear combination of $(i-1)$-simplices in C_{i-1} [108],

$$\partial_i \langle \mathbf{z}_0 \cdots \mathbf{z}_i \rangle = \sum_{j=0}^{i} (-1)^j \langle \mathbf{z}_0 \cdots \breve{\mathbf{z}}_j \cdots \mathbf{z}_i \rangle \tag{3.30}$$

Examples are shown in Fig. 3.5 of the boundary operator mapping between chain complexes. It may be seen that the simplicial complex W in this figure has one

hole, which may be determined by studying the boundary operators. For instance, the 2-simplex $\langle \mathbf{z}_0\mathbf{z}_1\mathbf{z}_2 \rangle$ is mapped using ∂_2 to the element $\langle \mathbf{z}_1\mathbf{z}_2 \rangle - \langle \mathbf{z}_0\mathbf{z}_2 \rangle + \langle \mathbf{z}_0\mathbf{z}_1 \rangle$ (see Eq. (3.30)). In other words, this element is in the image of ∂_2, and is termed a *boundary* [108]. It may be seen from Fig. 3.5 that this element appears to have a hole, along with the element $\langle \mathbf{z}_2\mathbf{z}_3 \rangle - \langle \mathbf{z}_1\mathbf{z}_3 \rangle + \langle \mathbf{z}_1\mathbf{z}_2 \rangle$, both of which are mapped to 0 using ∂_1. These elements are thus in the kernel of ∂_1, and are therefore termed *cycles* [108]. The holes in C_1 are then those cycles which are not also boundaries (*i.e.*, those cycles which are not "filled in" in C_2 [113]). Therefore, only the cycle $\langle \mathbf{z}_2\mathbf{z}_3 \rangle - \langle \mathbf{z}_1\mathbf{z}_3 \rangle + \langle \mathbf{z}_1\mathbf{z}_2 \rangle$ has a hole, and there is then one hole in the original simplicial complex. This procedure generalizes to an arbitrary dimension: the i-D holes in C_i are those cycles which are not also boundaries from C_{i+1}. The Betti number β_i, counting the number of independent i-D holes, is then [112]

$$\beta_i = \text{rank}\{\ker\{\partial_i\}\} - \text{rank}\{\text{img}\{\partial_{i+1}\}\} \tag{3.31}$$

where rank$\{\cdot\}$, ker$\{\cdot\}$, and img$\{\cdot\}$ denote the rank, kernel, and image, respectively.

The evolution of the Betti numbers over a range of ε provides a holistic topological representation of a datacloud. This representation is commonly visualized in the form of a *barcode* [56, 109], as shown in Fig. 3.3(e) and (f) for components and holes, respectively. Here, the barcode represents each component (or hole) as a line extending over the range of ε for which it exists. This example illustrates that those which are truly characteristic of the datacloud have longer lines (*i.e.*, exist longer) than those which may be noise. For this example, the Betti number computation is performed using the opensource Matlab software javaPlex [111]. Here, one component and two holes are identified in the barcodes. However, the barcode for one of the holes is significantly shorter than the other (roughly one-quarter of the length), suggesting that it may be noise. The observation of one dominant component and one dominant hole captures the true topology of the annulus from which the datacloud was sampled. Analyzing the barcodes therefore allows the topology of a datacloud to

be measured.

15 Hidden Markov Modeling

Hidden Markov modeling is a probabilistic approach to determining an underlying process through indirect observations. Of interest in this thesis is the situation of observing AE features and inferring an underlying corrosion process.

In a HMM, the adjective "hidden Markov" implies that the underlying process is Markovian, but that it is also not directly observable. Instead, information about the process can only be gained indirectly through related observations. A Markovian process is one which transitions between a set of states $1, \ldots, N$ at discrete time steps, for instance $t = 1, \ldots, T$. Secondly, it is one in which the transition to the next state only depends on the current state. In other words, its memory only goes back one unit in time. Within an HMM, a state-dependent observation is then made at each time step. Often the observations are discrete, in the sense that only one of M possible outcomes may be observed. An example of a 3-state HMM with $M = 2$ possible observations is visualized in Fig. 3.6.

At this point, consider a generic N-state HMM with M possible observations. Further, denote a state sequence as $S_1, \ldots, S_T$ and an observation sequence as $O_1, \ldots, O_T$, spanning time steps $t = 1, \ldots, T$. From these definitions, a HMM is then parameterized by three quantities: (1) an initial state distribution $\boldsymbol{\pi} = [\pi_1 \ \cdots \ \pi_N]$ describing the probability of the starting state, where $\pi_i = \mathbb{P}\{S_1 = i\}$ and $\mathbb{P}\{\cdot\}$ denotes the probability; (2) a transition probability matrix $\mathbf{A}_{N\times N}$ describing the probability of transitioning from one state to another, where the matrix elements are $A_{ij} = \mathbb{P}\{S_{t+1} = j | S_t = i\}$; and (3) an observation probability matrix $\mathbf{B}_{N\times M}$ describing the probability of observations within each state, where $B_{ij} = \mathbb{P}\{O_t = j | S_t = i\}$ for $t = 1, \ldots, T$.

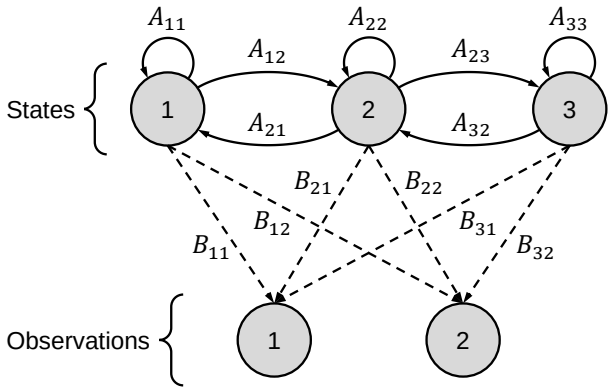

Fig. 3.6 Example hidden Markov model with $N = 3$ states and $M = 2$ observations. Nonzero transition and observation probabilities indicated by solid and dashed lines, respectively.

15.1 Model training

The technique for training a HMM is an iterative procedure known as the Baum-Welch algorithm. It takes an initial estimate for the parameters $\boldsymbol{\pi}^0, \mathbf{A}^0, \mathbf{B}^0$ and trains them to a point which better explains the training data. Here, a superscript 0 is used to denote an initial estimate. Since there are many possible local maxima in training [114], it is important to provide a good initial estimate for the parameters. Methods for generating estimates are described below.

If it is known which state a process starts in, then the initial state probabilities may be initialized accordingly. For instance, if it is known that the process starts in state j, then $\pi_i^0 = \delta_{ij}$. Otherwise, without any knowledge it is reasonable to assume a uniform initial distribution across the states, $\boldsymbol{\pi}^0 = [1/N \ \cdots \ 1/N]$.

A relation between the transition probabilities and the expected duration in each state can be leveraged to initialize the transition probability matrix. A geometric distribution describes the probabilistic nature of the duration T_i in state i. The expected duration is then related to the self-transition probability A_{ii} as $\mathbb{E}\{T_i\} = 1/(1-A_{ii})$, where $\mathbb{E}\{\cdot\}$ denotes the expected value. Therefore, if the expected duration is estimated, then the self-transition probability for a state can be estimated as [114]

$$A^0_{ii} = \frac{\mathbb{E}\{T_i\} - 1}{\mathbb{E}\{T_i\}} \tag{3.32}$$

For the special case of a *left-right* model with no state-skipping (*i.e.*, where $A_{ij} = 0$ for $i < j$ and $j > i + 1$), the remaining probabilities can also be determined,

$$A^0_{i(i+1)} = \frac{1}{\mathbb{E}\{T_i\}} \qquad \text{for } i < N \tag{3.33}$$

Lastly, the observation probabilities can be estimated by assuming independent identically distributed observations [115]. The estimations are then made from the relative frequencies of each observation recorded at each state,

$$B^0_{ij} = \sum_{t=1}^{T} \delta_{jO_t}\delta_{iS_t} \Big/ \sum_{t=1}^{T} \delta_{iS_t} \tag{3.34}$$

With the parameters estimated, efficient training of an HMM involves constructing *forward* and *backward* probabilities $\alpha_t(i) = \mathbb{P}\{O_1 \cdots O_t | S_t = i\}$ and $\beta_t(i) = \mathbb{P}\{O_{t+1} \cdots O_T | S_t = i\}$, respectively. These may be initialized as [114]

$$\begin{aligned} \alpha_1(i) &= \pi_i B_{iO_1} \\ \beta_T(i) &= 1 \end{aligned} \tag{3.35}$$

and then recursively computed as

$$\begin{aligned} \alpha_{t+1}(i) &= B_{iO_{t+1}} \sum_{j=1}^{N} \alpha_t(j) A_{ji} \\ \beta_{t-1}(i) &= \sum_{j=1}^{N} A_{ij} B_{jO_t} \beta_t(j) \end{aligned} \tag{3.36}$$

From these can be formed the probability of being in state i at time t, and the probability of transitioning from state i to j at time t, denoted $\gamma_t(i)$ and $\xi_t(i, j)$,

respectively. Specifically,

$$\begin{aligned}\gamma_t(i) &= \frac{\alpha_t(i)\beta_t(i)}{\sum_{j=1}^{N}\alpha_t(j)\beta_t(j)} \\ \xi_t(i,j) &= \frac{\alpha_t(i)A_{ij}B_{jO_{t+1}}\beta_{t+1}(j)}{\sum_{k=1}^{N}\sum_{l=1}^{N}\alpha_t(k)A_{kl}B_{lO_{t+1}}\beta_{t+1}(l)}\end{aligned} \tag{3.37}$$

The parameters of the HMM are then iteratively trained as

$$\begin{aligned}\pi_i^{k+1} &= \gamma_1^k(i) \\ A_{ij}^{k+1} &= \sum_{t=1}^{T-1}\xi_t^k(i,j)\Big/\sum_{t=1}^{T-1}\gamma_t^k(i) \\ B_{ij}^{k+1} &= \sum_{t=1}^{T}\gamma_t^k(i)\delta_{jO_t}\Big/\sum_{t=1}^{T}\gamma_t^k(i)\end{aligned} \tag{3.38}$$

where a superscript index is used to denote the training iteration. The training is then terminated at some number of iterations K, setting the trained parameters as $\boldsymbol{\pi} = \boldsymbol{\pi}^K$, $\mathbf{A} = \mathbf{A}^K$, and $\mathbf{B} = \mathbf{B}^K$. It should be noted (and may be seen from the above) that any parameters that are initially set to zero will remain so throughout the entirety of the training procedure.

15.2 State sequence decoding

From a trained HMM, the Viterbi algorithm may be used to decode the most likely state sequence $S_1 \cdots S_T$ which gave rise to a recorded observation sequence $O_1 \cdots O_T$ [114]. This involves maximizing the joint probability of the state and observation sequences $\mathbb{P}\{S_1 \cdots S_T, O_1 \cdots O_T\}$. The algorithm achieves this by recursively computing the highest probability of a partial state sequence (ending in state i at time t) while keeping track of the states which maximize the probability at each time step. Denoting this partial-sequence probability as $p_t(i)$,

$$p_t(i) = \max_{S_1 \cdots S_{t-1}} \Big\{\mathbb{P}\{S_1 \cdots S_{t-1}, S_t = i, O_1 \cdots O_t\}\Big\} \tag{3.39}$$

it may be computed recursively as

$$\begin{aligned} p_1(j) &= \pi_j B_{jO_t} \\ p_{t+1}(j) &= \max_i \{p_t(i) A_{ij}\} B_{jO_{t+1}} \end{aligned} \tag{3.40}$$

The optimal state sequence $S_1 \cdots S_T$ may then be decoded by backtracking through the maximizing arguments in the above. In particular, defining an argument tracker $\psi_t(j)$ as

$$\psi_t(j) = \arg\max_i \{p_t(i) A_{ij}\} \tag{3.41}$$

the state sequence may be found in reverse order as

$$\begin{aligned} S_T &= \arg\max_i \{p_T(i)\} \\ S_{t-1} &= \psi_{t-1}(S_t) \end{aligned} \tag{3.42}$$

In this thesis, the Baum-Welch and Viterbi algorithms are implemented in R using the HMM package [116].

15.3 Time discretization

One of the main obstacles in adapting a HMM for AE monitoring is transitioning to the required uniform-interval discrete time. This is because an AE DAQ continuously monitors for hits triggering the system. These hits are therefore recorded at nonuniform intervals in time, whereas a HMM requires observation data to be recorded at uniform intervals.

A natural approach to making this transition is binning the AE hits according to a uniform subdivision of the continuous time axis. This is visualized in Fig. 3.7 for an arbitrary bin width b. The discretized time axis then ranges from $t = 1, \ldots, T$, with units of b. An aggregate observation at each time step is then recorded from the collection of hits within the corresponding bin.

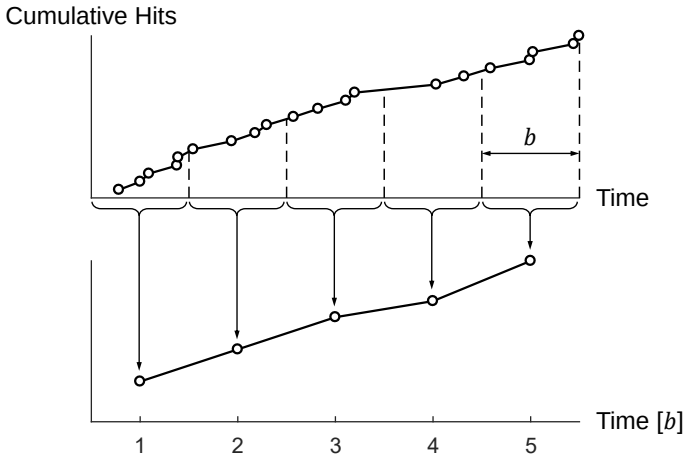

Fig. 3.7 Binning of hits to construct uniform-interval discrete time axis with units of the bin width b.

CHAPTER 4

Stress Monitoring in Corroding Strands

This chapter* presents a validation of higher-order modes for characterizing corrosion-induced stress change in steel strands. It is used to demonstrate the research statement that simplifying complexities in guided wave (GW) data enhances corrosion monitoring. Further, the value in this area of the wavelet transform, modal modulation, and data fusion are shown.

16 Experiment

16.1 Test specimen

A loading frame was constructed to house an accelerated corrosion test for a pre-stressed seven-wire strand, as shown in Fig. 4.1. The frame consisted of a steel bed, an arm, and two threaded rods. Tension was applied through the frame by turning the two rods with a torque wrench, which then moved the arm and deformed the strand (connected to the arm through anchors). The bed and arm were built from square sections (AISC HSS4 $\times 4 \times \frac{1}{4}$), composed of A500 Grade B steel. The threaded rods were composed of corrosion-resistant 316 stainless steel. In addition, to protect the frame from the corrosive environment, a two layer coating was applied to the bed and the arm. This consisted of a rust preventative primer and a corrosion-resistant top coat.

* This chapter is derived in part from the author's work in [61, 62, 65, 66].

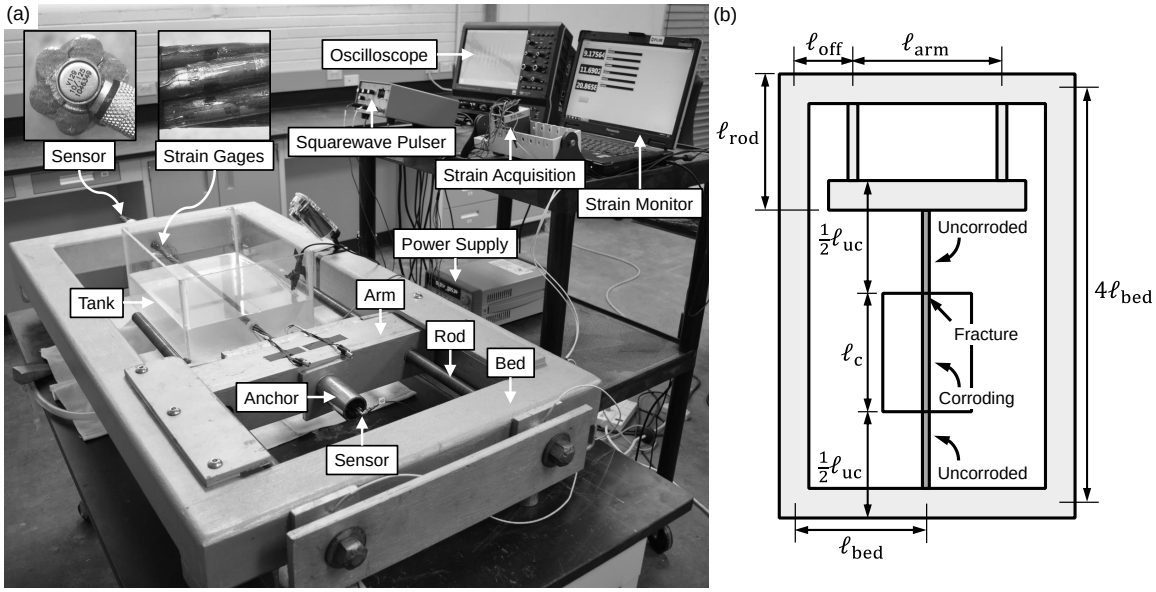

Fig. 4.1 (a) Experimental setup and data acquisition system for guided wave and strain monitoring of prestressed strand under accelerated corrosion. Corrosion applied by impressing current in saltwater tank using power supply. (b) Schematic of loading frame, indicating relevant dimensions. Eventual peripheral wire fracture point near the tank edge shown.

Table 4.1 Relevant dimensions for various elements of the loading frame and strand.

Dimension	Metric	Imperial
ℓ_{uc}	0.72 m	28.3 in.
ℓ_{c}	0.38 m	15.0 in.
ℓ_{arm}	0.41 m	16.0 in.
ℓ_{bed}	1.32 m	52.0 in.
ℓ_{rod}	0.49 m	19.2 in.
ℓ_{off}	0.13 m	5.0 in.
A_{uc}	143 mm^2	0.222 in.^2
A_{bed}	21.7 cm^2	3.37 in.^2
A_{rod}	3.87 cm^2	0.601 in.^2
I_{arm}	1170 cm^4	28.1 in.^4
I_{bed}	325 cm^4	7.80 in.^4

The prestressing strand was composed of Grade 270 steel (1860 MPa ultimate tensile strength, or UTS), with a nominal diameter of 15.2 mm (0.6 in.), and a lay angle of 7.9°. The strand complied with ASTM A416 [117], which dictates a yield strength of at least 90% UTS (1670 MPa). To obtain precise dimension measurements, a second strand from the same spool was disassembled, allowing the core and peripheral wire diameters to be measured at 5.22 and 5.08 mm, respectively. Within the anchors, the strand was composed of uncorroded and corroding segments. The strand lengths within these segments are denoted ℓ_{uc} and ℓ_{c}, respectively. The length of the strand within the anchors (*i.e.*, under stress) was then $\ell_{\mathrm{uc}} + \ell_{\mathrm{c}}$. The dimensions of the frame and strand are depicted in Fig. 4.1(b) and collected in Table 4.1.

To record the strand deformation, six strain gages (Micro Measurements C2A-06-250LW-350) were installed on the peripheral wires in the uncorroded segment, as shown in Fig. 4.1(a). The six strain readings were then used to obtain the average axial strain e in the peripheral wires. It may be noted that, for a 7.9° lay angle, the peripheral and core wire strains only differ by roughly 2% [30]. Therefore, the strain e was taken to describe the axial strain in the strand cross-section as a whole. The strand was initially loaded up to $\tau_0 = 480$ MPa (69.7 ksi), or roughly 25% UTS, yielding an initial (reference) strain value of $e_0 = 2.28 \times 10^{-3}$.

16.2 Accelerated corrosion testing

Accelerated corrosion was carried out with the impressed current technique [118], as shown in Fig. 4.1(a). In particular, a galvanic cell was constructed in a saltwater tank, through which DC current was applied. The cell was formed by submerging a segment (*i.e.*, corroding segment) of the strand along with a copper mesh in a 5% NaCl saltwater solution within the tank. Current was applied and recorded with a DC power supply (Keysight E3633A) and ranged from 1.5-3.0 A.

The current was applied in cycles, ranging from 2-5 hours in duration. A total of 29 corrosion cycles were carried out over a period of 115 days, resulting in 94 total

hours of accelerated corrosion. After each cycle, the tank was drained and the strand was allowed to dry for 24 hours with no applied current. Corrosion products were allowed to build up on the surface of the strand, in order to closely simulate naturally accumulating corrosion. Due to the strong sensitivity of corrosion rate to temperature [119], the temperature of the specimen was controlled at 23 ± 1 °C (74 ± 2 °F). The accelerated corrosion was terminated when a fracture occurred simultaneously in three adjacent peripheral wires. The fracture point is indicated in Fig. 4.1(b), located roughly 2 cm (0.8 in.) from one end of the tank.

16.3 Guided wave sensing

Higher-order modes were generated and received by piezoelectric transducers (Olympus V129-RM) installed on either end of the strand, as shown in Fig. 4.1(a). The transducers were 5 mm (0.2 in.) in diameter, and selected to be nearly identical to the core wire diameter (5.22 mm). The modes were generated in the core wire by installing the transducers (using hot glue) over its cross-section. The transducers were excited by a wideband squarewave pulse using a squarewave pulser-receiver (Olympus 5077PR). The excitation was tuned to 7.5 MHz, which was used to target modes L(0,8)-L(0,14) from 5-10 MHz (25-50 MHz-mm). High and low pass analog filters at 1 MHz and 10 MHz, respectively, were used to further suppress frequencies outside the target range. The modes were recorded on an oscilloscope (LeCroy HDO6104), while sampling at 250 MHz and averaging 500 times.

An initial collection of higher-order mode signals was performed before corrosion (*i.e.*, at cycle 0). Subsequently, signals were recorded after each corrosion cycle, following the 24 hour drying period. The modes were recorded after this period in order to remove the effect of water immersion on wave propagation. To investigate the performance of the proposed modal modulation technique, the transducers were reattached before each corrosion cycle, which introduced artificial phase shifts into the waveforms.

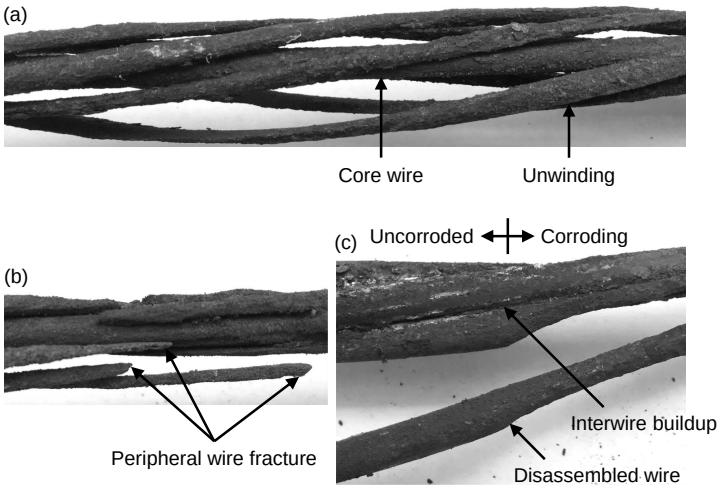

Fig. 4.2 Post-corrosion inspection of unloaded strand: (a) unwinding of peripheral wires, (b) fractured wires, and (c) interwire buildup of corrosion products near fracture point. Core wire diameter (5.20 mm) found to be nearly the same as before corrosion (5.22 mm).

17 Corrosion Progression and Benchmark Assessment

17.1 Visual inspection

The corrosion process in the strand was observed visually after each corrosion cycle. It was found that corrosion products gradually built up on the surface of the strand as the test progressed and continued until the simultaneous three-wire fracture occurred at cycle 29. The strand was then unloaded and removed from the loading frame for further visual inspection, as shown in Fig. 4.2. Due to unloading, the fractured wires further unwound within the corroding segment, as shown in Fig. 4.2(a). However, it should be noted that the peripheral wires did not unwind in the uncorroded segment, as seen in Fig. 4.2(c). Furthermore, near the edges of the corroding segment, corrosion products built up between the fractured wires and the core wire, which increased interwire friction. It was found that the core wire had a minor amount of corrosion products on its surface. This appears to have been predominantly suffered when the fractured wires unwound and directly exposed the core wire to saltwater. The core wire diameter was measured at 30 locations within the corroding segment, yielding an average value of 5.20 mm and a standard deviation of 0.09 mm. This is nearly the

same as its uncorroded value (5.22 mm). In contrast, the peripheral wires suffered diameter losses of roughly 23 mm. This demonstrates that the large majority of mass loss took place in the peripheral wires, which is in agreement with [8–10].

17.2 Mass loss measurement

Faraday's law was used to convert the impressed current i_{cor} in each corrosion cycle to cumulative strand mass loss M_{loss}. With the strand composed primarily of Iron, the cumulative mass loss up to cycle c may be found as [17]

$$M_{\text{loss}}(c) = \frac{M_{\text{Fe}}}{Z_{\text{Fe}} F_{\text{far}}} \sum_{j=1}^{c} i_{\text{cor}}(j) t_{\text{cor}}(j) \tag{4.1}$$

where $M_{\text{Fe}} = 55.8$ g/mol is the molar mass of Iron, $Z_{\text{Fe}} = 2$ is the ionic charge of Iron (*i.e.*, the number of valence electrons), $F_{\text{far}} = 96,500$ A·s/mol is Faraday's constant, and $t_{\text{cor}}(j)$ is the duration of the j-th cycle. The percentage mass loss in the corroding segment may be calculated as $M_{\text{loss}}/M_{\text{c}}$, with M_{c} the original mass of the corroding segment. It may be noted that the mass loss nearly reached 50% by the completion of the experiment.

17.3 Benchmark stress measurement

Linear-elastic structural analysis was carried out in order to obtain a ground-truth measurement of stress in the strand. The aim was to convert the strain in the uncorroded segment to stress in the corroding segment. This was required since strain gages could not be installed in the corroding segment. To this end, the structural system formed by the strand (*i.e.*, uncorroded and corroding segments) and the loading frame was studied. This analysis may be found in Appendix B.

Figure 4.3 shows the resulting measured stress in the strand over the corrosion process. The stress is shown here for the uncorroded and corroding segments of the strand, denoted $\tau_{\text{uc}} = \tau_0 + \Delta\tau_{\text{uc}}$ and $\tau_{\text{c}} = \tau_0 + \Delta\tau_{\text{c}}$, respectively. Here, the yield stress

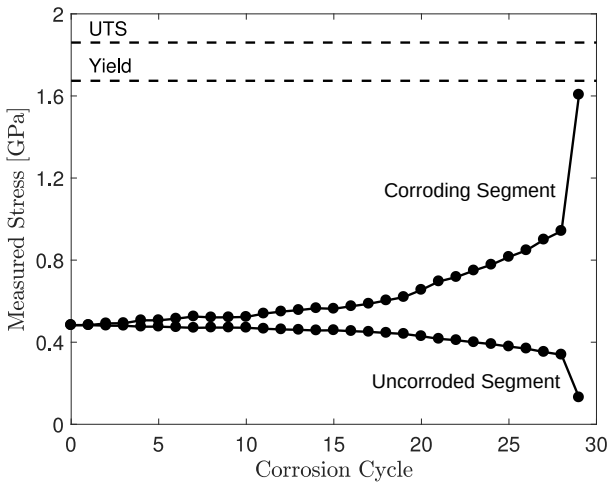

Fig. 4.3 Benchmark measured stresses in the uncorroded and corroding segments of the strand, τ_{uc} and τ_{c}, respectively.

and ultimate tensile strength are overlain as dashed lines. It may be seen that the stresses in the two segments began at the same value. Subsequently, a stress increase formed in the corroding segment, while the stress gradually relaxed in the uncorroded segment. The stress in the corroding segment closely approached the yield point in cycle 29, but did not exceed it. The fact that there was a peripheral wire fracture in the corroding segment at subyield stress may be due to corrosion-induced hydrogen embrittlement [120].

17.4 Guided wave mode processing

The generation and reception of higher-order modes was confirmed by applying the wavelet transform. This was carried out for the signals obtained at each corrosion cycle, denoted $s_0, \ldots, s_{29}$, so that the wavelet transforms from Eq. (3.1) are denoted $\tilde{s}_0, \ldots, \tilde{s}_{29}$. The Gabor mother wavelet parameter ς was set to 80 in order to resolve the plateau frequencies of higher-order modes from 5-10 MHz (while satisfying $\varsigma \gg 1$).

To compare the experimental waves to theory, it is also useful to express the wavelet transforms in terms of the group velocity as $\tilde{s}_0(c_{\mathrm{g}}, \omega), \ldots, \tilde{s}_{29}(c_{\mathrm{g}}, \omega)$. This may be done by inverting the time axis and scaling by the propagation distance to

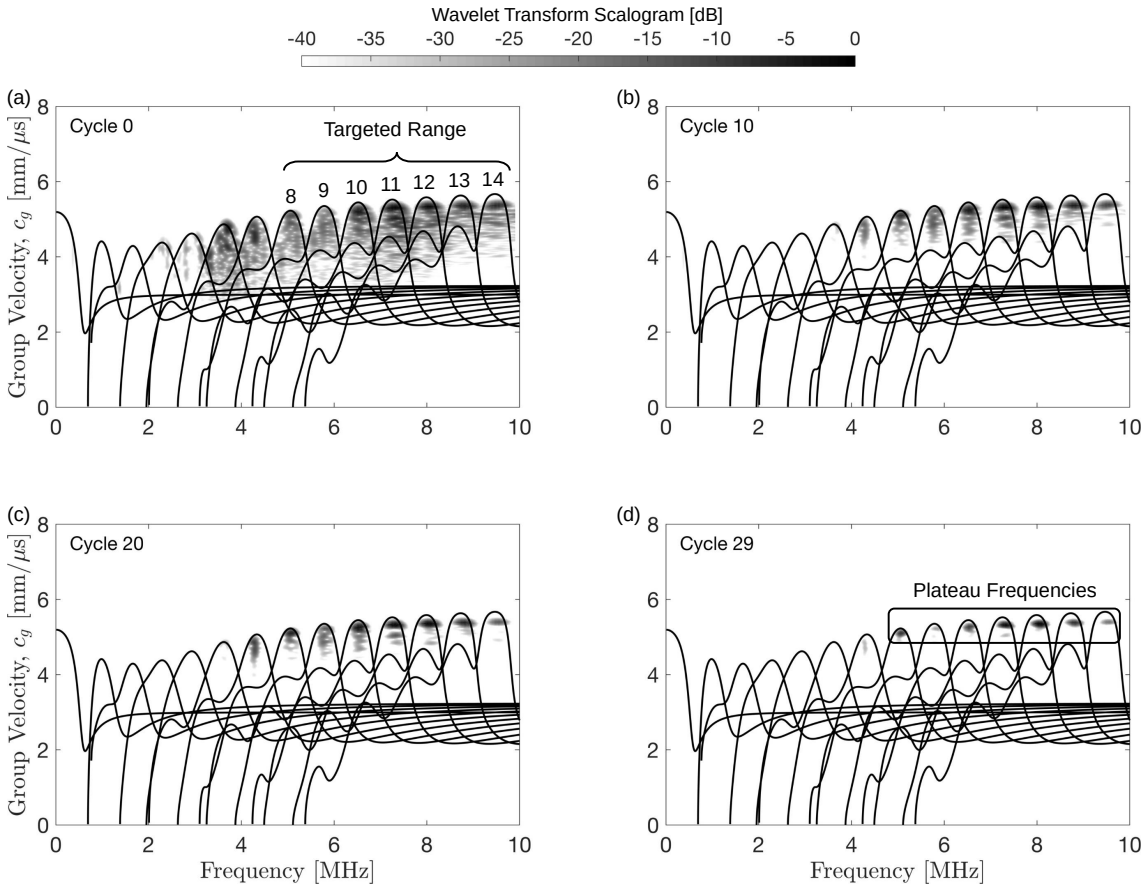

Fig. 4.4 Wavelet transform scalogram (-40 to 0 dB) in group velocity-frequency space at four corrosion cycles, $|\tilde{s}_0|^2, |\tilde{s}_{10}|^2, |\tilde{s}_{20}|^2, |\tilde{s}_{29}|^2$. Dispersion curves for longitudinal modes in 5.22-mm-diameter steel rod overlain. Higher-order modes $\mathrm{L}(0,m)$, $m = 8, \ldots, 14$ generated in frequency range 5-10 MHz are indicated. Due to increasing attenuation, only the plateau frequencies of higher-order modes remain by cycle 29.

obtain a group velocity axis. Figure 4.4 shows the scalogram $|\tilde{s}_c|^2$ of the wavelet transform at four corrosion cycles $c = 0$, 10, 20, and 29, as plotted against frequency and group velocity. Seven higher-order modes were generated within the targeted frequency range (5-10 MHz), as highlighted in the figure. These modes were L(0,8)-L(0,14), whose plateau frequencies are 5.05, 5.80, 6.50, 7.25, 8.00, 8.80, and 9.50 MHz, respectively. For comparison with theory, the group velocity dispersion curves for longitudinal modes are overlain in the figure. As corrosion increased, the only regions of the dispersion spectra that were not significantly attenuated were near the plateau frequencies. This may be seen from Fig. 4.4(b)-(d), where only the plateau frequencies remain by cycle 29 (*i.e.*, at fracture).

With the reception of higher-order modes confirmed, signals for each mode at their respective plateau frequencies were obtained by using the wavelet transform as a narrowband filter. Specifically, the signal for the m-th mode at the c-th corrosion cycle was obtained following Eq. (3.7) as

$$s_c^{(m)}(t) = \Re\tilde{s}_c(t, \omega^{(m)}) \tag{4.2}$$

18 Higher-Order Mode Analysis

18.1 Modal modulation

The modal modulation technique described in Sec. 11 was carried out experimentally as follows: first, consecutive higher-order modes L$(0, m)$ and L$(0, m+1)$ were grouped into pairs. Their respective signals $s_c^{(m)}$ and $s_c^{(m+1)}$ at each corrosion cycle were then normalized to give each a unit maximum amplitude. Afterward, the signals for each were superposed. The modulation wave was then obtained through the envelope of the superposition, using Eq. (3.10). The entire modulation process is visualized in Fig. 4.5.

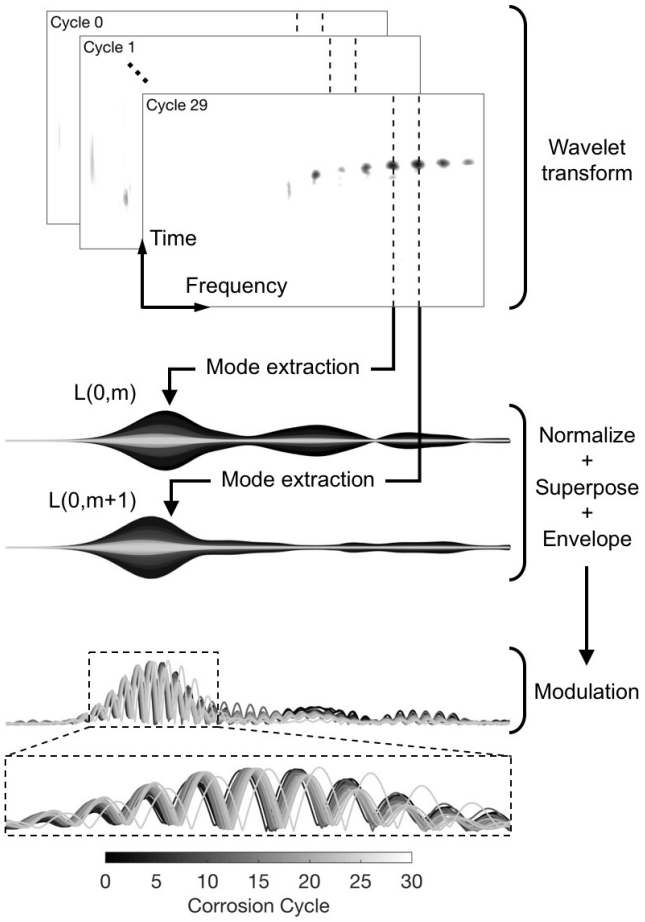

Fig. 4.5 Extraction of modulation waves used for stress measurement. Consecutive higher-order modes $\mathrm{L}(0, m)$ and $\mathrm{L}(0, m+1)$ extracted in pairs and superposed to form modulations.

Once the modulation waves were obtained, their time change over the range of corrosion cycles was measured. This was performed by tracking a peak in the modulations follows: first, the peak in the cycle 0 modulation wave was obtained, which served as the reference value. The change in this peak was then tracked in the modulation waves for subsequent cycles, from which the time change was measured. Here, the acoustoelasticity framework was adopted, with the "undeformed" body taken as the stressed strand at cycle 0. The time change at a given cycle was then converted to a stress change estimate using Eq. (2.183) to yield

$$\Delta\tau_c^{(p)} = -\frac{c_{l0}^2}{\kappa_l \ell}\Delta t_c^{(p)} \tag{4.3}$$

It should be noted that the strand began under a stress of $\tau_0 = 480$ MPa in cycle 0, and therefore the use of c_{l0} as the reference velocity in the above may appear strange. However, since the true velocity at this stress level only differs from $c_{l0} = 5923$ m/s by the relatively small amount $\kappa_l \tau_0 = 46.6$ m/s (or less than 1%), using the velocity c_{l0} is appropriate under the linearized framework discussed in Sec. 7.

With the propagation path containing both uncorroded and corroding segments, the linearity of the acoustoelastic effect implies that the stress change in Eq. (4.3) estimates the average stress change along the strand. In order to compare this to the measured stress values, the average stress change $\Delta\tau$ over the course of corrosion was obtained from the benchmark changes in the uncorroded and corroding segments as

$$\Delta\tau = \frac{\ell_{\mathrm{uc}}}{\ell}\Delta\tau_{\mathrm{uc}} + \frac{\ell_{\mathrm{c}}}{\ell}\Delta\tau_{\mathrm{c}} \tag{4.4}$$

Figure 4.6 shows the stress change estimates using Eq. (4.3) for six higher-order mode pairs 8-9,9-10,. . . ,13-14, with the benchmark measured change from Eq. (4.4) overlain. It may be seen that the estimation of stress change using higher-order modes shows good agreement with the measured values. The initial slow rate in stress change up to cycle 20 may be seen in the estimates, as well as the subsequent increasing rate

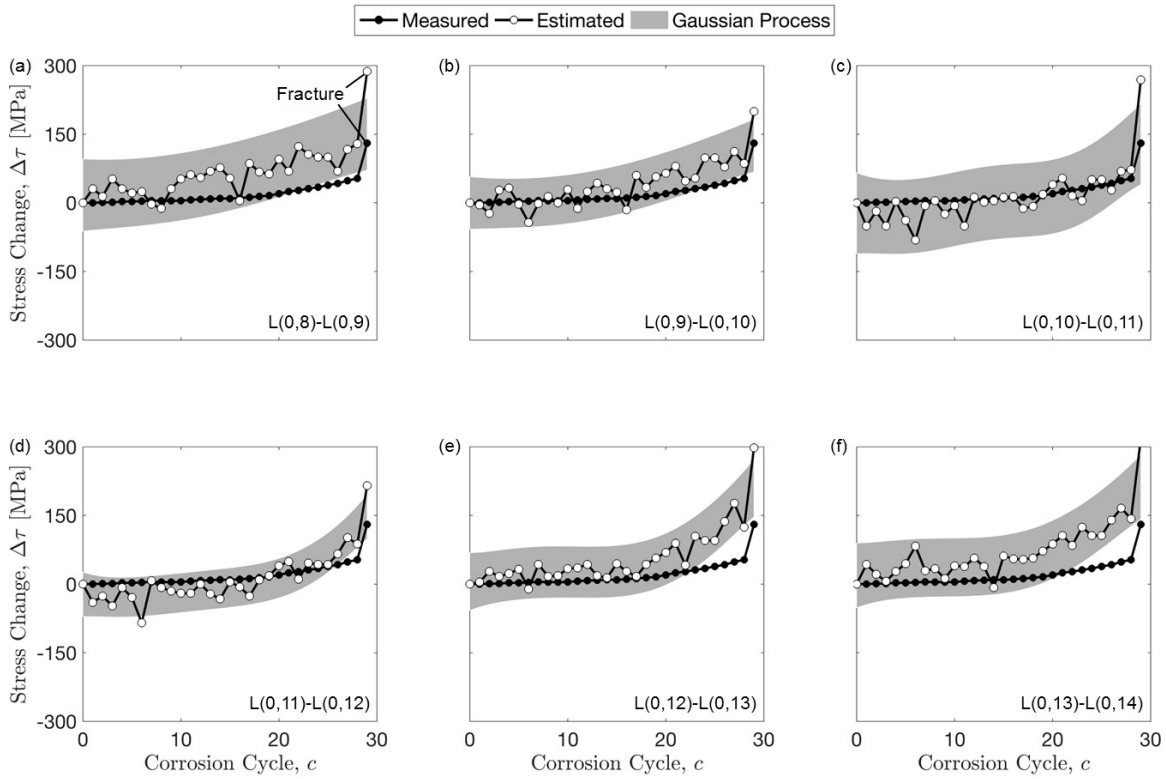

Fig. 4.6 Stress change estimated using velocity change for six higher-order mode pairs, shown in (a)-(f), respectively. Velocity change measured at plateau frequency for each mode. Shaded area overlain as 95% confidence interval from gaussian process regression. Stress change measured based on strain gages overlain.

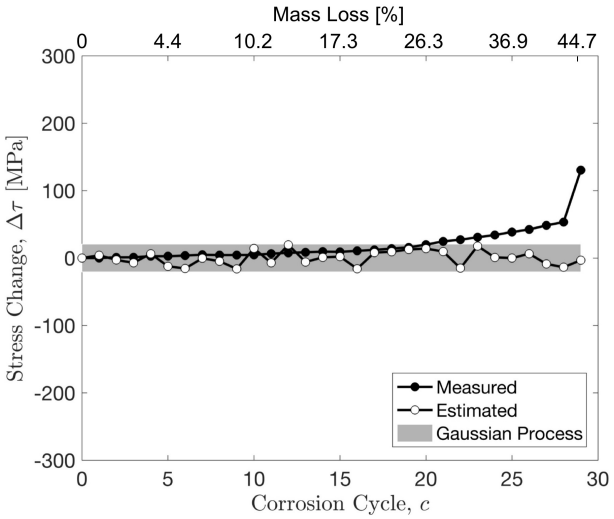

Fig. 4.7 Stress change estimated using data fusion of six higher-order mode pairs, ranging from L(0,8) to L(0,14). Shaded area overlain as 95% confidence interval from gaussian process regression. Stress change measured based on strain gages is overlain.

beyond this cycle. Importantly, the large stress increase caused by peripheral wire fracture in cycle 29 is revealed in each of the mode pairs. In particular, the largest cycle-to-cycle change in the estimated data is from cycle 28-29, where the fracture occurred. To quantify uncertainty in the estimates, gaussian process regression (GPR) was computed from Eq. (3.20) and overlain in Fig. 4.6. Some variation in the uncertainty may be seen between different mode pairs, with the standard deviation of the GPR ranging from 27-41 MPa.

18.2 Data fusion

The previous subsection demonstrated that multiple higher-order mode pairs yield (beneficially) redundant estimations of stress change. Therefore, the data fusion approach outlined in Sec. 12 was adopted in order to combine the data shown in Fig. 4.6 into a single stress change estimate. In particular, data fusion was performed by applying Eq. (3.15) at each corrosion cycle. The amplitudes input to the weight assignment in Eq. (3.18) were obtained from the wavelet transform at each cycle, as shown in dB in Fig. 4.4.

To provide a benchmark assessment of stress change, data fusion results are first shown in Fig. 4.7 for traditional phase-based stress measurement. Modal modulation is therefore not applied in this case. Within the data fusion framework, $P = 7$ modes were incorporated, from L(0,8) to L(0,14). It may be seen that the results were not largely different from a random estimation, due to the artificial phase shifts introduced at each cycle through sensor reattachment. Indeed, the GPR indicates that the results are zero-mean noise across the corrosion process. The incoherent results demonstrate that there is no value in using phase measurements under such longterm monitoring conditions.

Building upon this benchmark, Fig. 4.8 shows the estimated stress change found by incorporating modal modulation within the data fusion framework. Specifically, the modulation-based estimates from Fig. 4.6 were used, with $P = 6$ mode pairs contributing to the fusion estimate in Eq. (3.15). It may be seen that the initial period up to 17% mass loss (cycle 1-15), which had a slow rate of stress change, was accurately captured by the data fusion estimate. Although there was considerable mass loss, the estimates were able to capture that the strand had not yet significantly lost load-carrying capacity. These estimates were achieved even with significant surface roughness and corrosion products building up on the surface of the strand. It demonstrates the advantage of using higher-order modes in the core wire, which diminishes the influence of surface effects. This may be contrasted to the fundamental mode, which is more sensitive to geometrical effects like surface roughness. Although there was a slight divergence from the measured stress change after cycle 20, the major spike caused by peripheral wire fracture at cycle 29 was well identified. It may be seen from the overlain GPR that the uncertainty of the estimated stress change was lower for the fused data than for any of the original mode pairs (see Fig. 4.6). Specifically, the standard deviation of the fused data was 25 MPa (defined as the average standard deviation of the GPR). In contrast, the standard deviation for the original data ranged from 27-41 MPa. Greater confidence was therefore found when

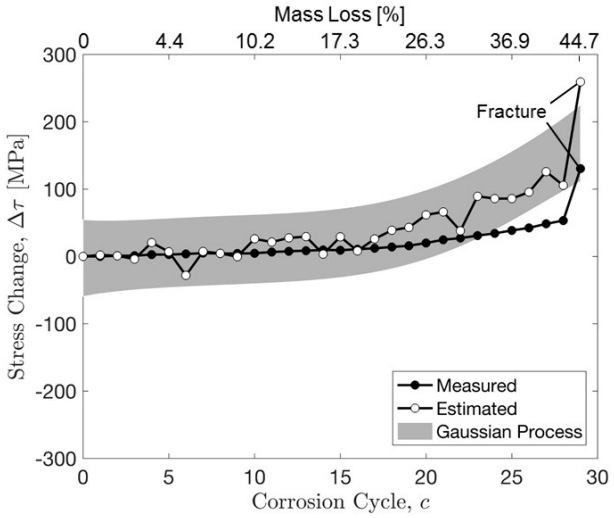

Fig. 4.8 Stress change estimated using data fusion of six higher-order mode pairs, ranging from L(0,8) to L(0,14). Shaded area overlain as 95% confidence interval from gaussian process regression. Stress change measured based on strain gages is overlain.

using data fusion to estimate the stress change, as opposed to using a single mode pair.

19 Summary

This application has demonstrated the ability of higher-order modes to estimate corrosion-induced stress change in a strand up to the point of fracture. This was made possible through a data fusion approach and a proposed modal modulation technique. The framework relied on exploiting various advantageous properties of higher-order modes (*e.g.*, stable velocity, low surface roughness sensitivity). The suitability of higher-order modes for data fusion is a further advantage of their use, which has not been noted in the literature.

The estimated stress change closely followed the measured values during the first half of the corrosion process (up to roughly 17% mass loss). The major stress increase caused by fracture was also captured well. Even though the approach was

validated on corrosion-induced stress change, it is conceivable that stress change due to non-damage sources may also be monitored (*e.g.*, traffic loading). Moreover, the value of the modal modulation technique for real-world settings was demonstrated, with the transducers being reattached after each corrosion cycle.

It should be noted that only stress *changes* can be monitored using the presented approach. Monitoring absolute stress would require a reference value (*e.g.*, the initial stress before corrosion). Furthermore, this approach is only able to monitor the average stress change along a given length of strand and therefore is not able to map the stress change distribution along such a length. Finally, temperature effects were not studied, but these will likely need to be compensated for in real applications. Fortunately, substantial research has already been established on temperature effects and compensation for GWs [29, 121].

CHAPTER 5

Corrosion Monitoring in Prestressed Concrete

This chapter* presents the validation of corrosion monitoring via acoustic emission (AE). It is used to demonstrate the research statement that understanding complexities in AE data enhances corrosion monitoring. The data processing involved from Chapter 3 includes computing AE features, topological data analysis (TDA), and hidden Markov models (HMMs).

20 Experiment

20.1 Test specimens

Two prestressed concrete specimens were considered for corrosion testing. The first served as a control specimen, from which hypotheses were generated about the proposed AE-based corrosion monitoring. The second specimen served as a means of evaluating and generalizing these hypotheses.

The prestressed specimens were cast as rectangular blocks with nominal dimensions of $51 \times 25 \times 23$ cm ($20 \times 10 \times 9$ in.) and mix proportions according to Table 5.1. An example of one of the specimens may be seen in Fig. 5.1. A single seven-wire strand (same specifications as in Chapter 4) was cast lengthwise through each block at a 4.5 cm (1.8 in.) cover and prestressed to 89 kN (20 kip). The strand extended roughly 18 cm (7 in.) outside the concrete on either side.

* This chapter is derived in part from the author's work in [64, 67].

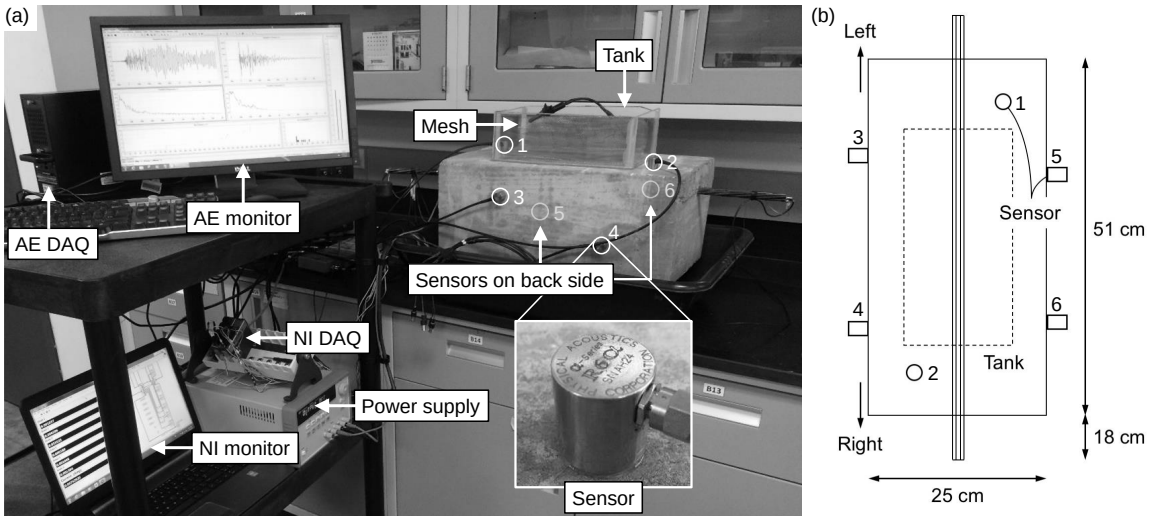

Fig. 5.1 (a) Experimental setup and data acquisition system for accelerated corrosion testing of a prestressed concrete specimen. Acoustic emission sensors are highlighted, with those hidden from view indicated. (b) Schematic of instrumented specimen, as viewed from above, with rightward and leftward ends indicated.

Table 5.1 Mix proportions for prestressed concrete specimens.

Material	Description	Metric	Imperial
Water	–	117 kg/m^3	252 lb/yd^3
Cement	Type III	418 kg/m^3	705 lb/yd^3
Fine aggregate	SSD river sand	835 kg/m^3	1407 lb/yd^3
Coarse aggregate	SSD river gravel	1043 kg/m^3	1758 lb/yd^3
Chemical admixture	Superplasticizer	2298 ml/m^3	8.46 fl oz/cwt
	Retarder	766 ml/m^3	2.82 fl oz/cwt

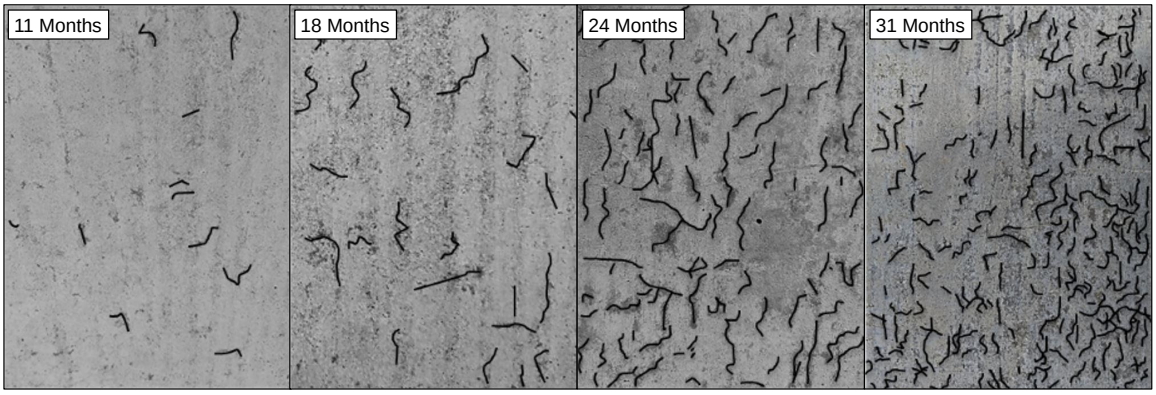

Fig. 5.2 Progression of surface microcracking over time in the weathered specimen. Cracks highlighted in black.

After casting, each specimen was cured indoors for 28 days. The control specimen then remained indoors and was tested soon afterwards. The weathered specimen, however, was subsequently placed outdoors for a total of 31 months ($\approx$ 2.5 years). After 16 months outdoors, it was subjected to accelerated weathering. This consisted of 14 months of being sprayed with water for five minutes, four times per day. The accelerated weathering was applied in order to generate distributed surface microcracking, which is a common form of weathering seen in the field by the Texas Department of Transportation. The progression of microcracking in the weathered specimen may be seen in Fig. 5.2.

20.2 Accelerated corrosion testing

Accelerated corrosion was carried out in each specimen using the impressed current technique [118], which may be seen in Fig. 5.1. Accordingly, chlorides were penetrated into the concrete by ponding a 5% NaCl saltwater solution in a tank mounted on the upper concrete surface. This tank position was adopted to simulate the natural downward seepage of water and chlorides in the field. A galvanic cell was then formed between the strand and a copper mesh submerged in the tank. A constant potential of 20 V was applied to the galvanic cell using a DC power supply. The resulting current ranged from 20-70 mA (80-290 $\mu A/cm^2$) and was recorded via a shunt resistor and

a National Instruments compact data acquisition (DAQ) system. The current was applied in cycles (*i.e.*, corrosion cycles), ranging from 4-8 hours at a time, with a gap of 1-4 days between consecutive cycles. This pattern was repeated for 118 and 104 cycles (206 and 150 days) in the control and weathered specimens, respectively, until a surface cracking limit state in the concrete was reached. To limit the effect of temperature on corrosion, the laboratory environment was held relatively constant throughout the test at 22-25 °C (72-77 °F).

20.3 Acoustic emission sensing

AE was continuously recorded during each corrosion cycle using a Mistras Micro-Express DAQ system, as shown in Fig. 5.1. To this aim, six Physical Acoustics Corporation (PAC) R6α sensors were bonded to the concrete surface using hot glue. The sensors were 1.9 cm (0.75 in.) in diameter, with a peak response near 60 kHz. The sensors were bonded to three sides of the concrete surface, with two sensors per side. This arrangement was chosen in order to provide adequate sensor coverage for the tested specimen. The individual sensor locations were nominally the same (within 1 cm) between the two specimens.

AE waveforms recorded during accelerated corrosion testing were preamplified by 40 dB using 2/4/6 preamplifiers (PAC). A fixed threshold of 50 dB was used for triggering the DAQ, which was determined prior to testing by measuring the ambient noise level and adding roughly 10 dB. High- and lowpass analog filters at 1 kHz and 1 MHz, respectively, were applied during data collection. In addition, the hit lockout time was set to 2.5 ms, the hit definition time to 600 µs, the peak definition time to 300 µs, and the maximum duration to 1 ms. Lastly, the recorded signals were sampled at 5 MHz. The digitized AE waveforms (*i.e.*, hits) were then converted to feature-based representations according to Sec. 13. Each hit was therefore represented in terms of energy, peak frequency, risetime/amplitude, and average frequency.

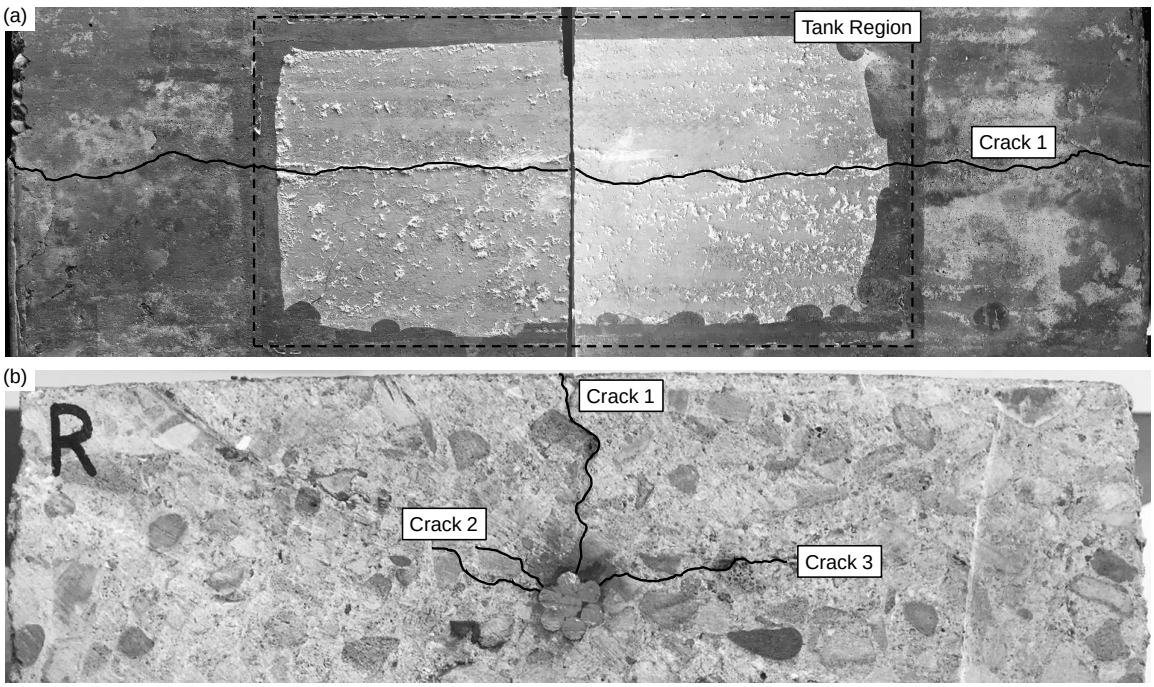

Fig. 5.3 Post-corrosion visual and destructive inspection. (a) Surface crack extending along the length of specimen, as viewed from above. (Note: two halves of cut-open specimen joined into one image.) (b) Right side of cut-open cross-section, highlighting three cracks propagating radially from strand. Cracks highlighted in black.

21 Corrosion Progression and Benchmark Assessment

A benchmark assessment of corrosion was first carried out for the control specimen. This included visual and destructive inspection, mass loss measurement, and traditional AE analysis, as described below.

21.1 Visual inspection

The control specimen did not show any visual signs of corrosion until the later stages of testing. The first concrete cover crack was found toward the right end of the specimen at cycle 108, as indicated in Fig. 5.3(a). This surface crack ran parallel to the strand, and extended from the rightward end of the saltwater tank to the nearby exiting point of the strand. It is possible that this crack opened earlier than cycle 108, along the surface underneath the saltwater tank, but was not noticed due to lack

of visibility through the tank. At cycle 115, an analogous crack was found mirrored on the opposite side of the specimen. All crack widths were in the barely visible range of roughly 0.05-0.1 mm, as defined in [15, 16]. The test was terminated a few cycles later at cycle 118, since the observed crack widths corresponded to the surface cracking limit state [12, 15]. After the test was completed, the two cracks on either end of the specimen were found to be connected through the area under the tank, as shown in Fig. 5.3(a). There was thus a continuous cover crack extending along the length of the specimen by the termination of the test.

To better understand the interior crack pattern, a destructive inspection was carried out after the completion of the test. The control specimen was cut in half perpendicular to the strand; the rightward surface of the cross-section may be seen in Fig. 5.3(b). Here, it may be seen that corrosion products primarily built up on the upper surface of the strand, which was in direct contact with downward-seeping saltwater. The accumulation of corrosion on the upper surface caused a buildup of pressure, resulting in the three radial cracks seen in Fig. 5.3(b). The crack propagating upward through the concrete cover (*i.e.*, Crack 1) was the only one visible from the outer surface. The other two cracks propagated radially at about $\pm 75^\circ$ angles with respect to Crack 1, but did not reach the surface.

21.2 Mass loss measurement

Faraday's law was used to convert impressed current to mass loss, in a similar to manner to that used in Chapter 4. However, the fact that mass loss did not begin until the moment of depassivation was accounted for through the following modification:

$$M_{\text{loss}}(c) = \begin{cases} 0 & \text{for } c < c_{\text{d}} \\ \dfrac{M_{\text{Fe}}}{Z_{\text{Fe}} F_{\text{far}}} \sum_{i=c_{\text{d}}}^{c} i_{\text{cor}}(i) t_{\text{cor}}(i) & \text{for } c \geq c_{\text{d}} \end{cases} \tag{5.1}$$

Here, c_{d} is the cycle at which the strand was depassivated (determined in Sec. 21.3). It may be noted that the mass loss reached nearly 5% by the completion of the

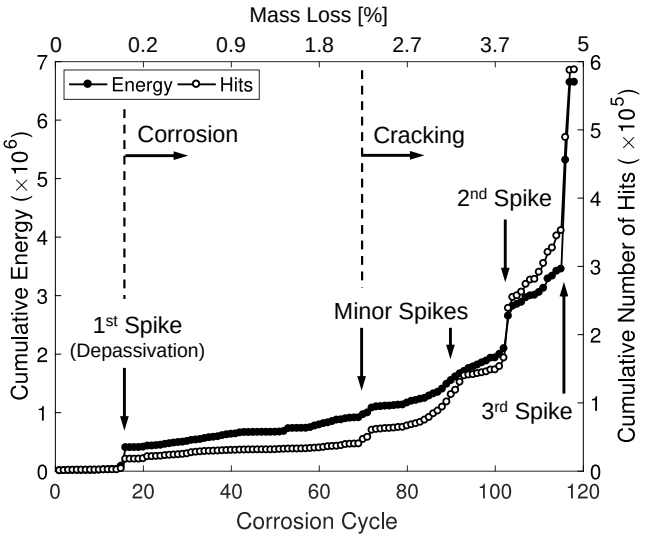

Fig. 5.4 Acoustic emission activity recorded in the control specimen, in terms of cumulative energy and number of hits. Corrosion onset (depassivation) may be seen at cycle 15 where the first activity spike occurred.

experiment, when the cover cracking was fully engaged. This level of mass loss at the point of cover cracking agrees well with reported data [21].

21.3 Traditional acoustic emission analysis

21.3.1 Activity analysis

The cumulative AE activity generated during the corrosion process for the control specimen may be seen in Fig. 5.4. Corrosion onset is indicated by the distinct first spike in AE activity [17], beginning at cycle $c_{\mathrm{d}} = 15$. The corresponding onset of corrosion is indicated at this point in Fig. 5.4. Minor AE activity spikes appeared around cycles 70 and 90, which may be seen in terms of both energy and hits. The minor spikes near cycles 70 and 90 may respectively be related to initiation and propagation of Crack 1 [42]. The next major spike in AE activity occurred at cycle 103. From the time at which it occurred, this spike may be related to near-surface propagation of Crack 1, which was found at the surface 5 cycles later. The subsequent increase in the AE activity rate may then be related to gradual propagation of the crack, with it eventually reaching the surface by cycle 108. The final and largest AE

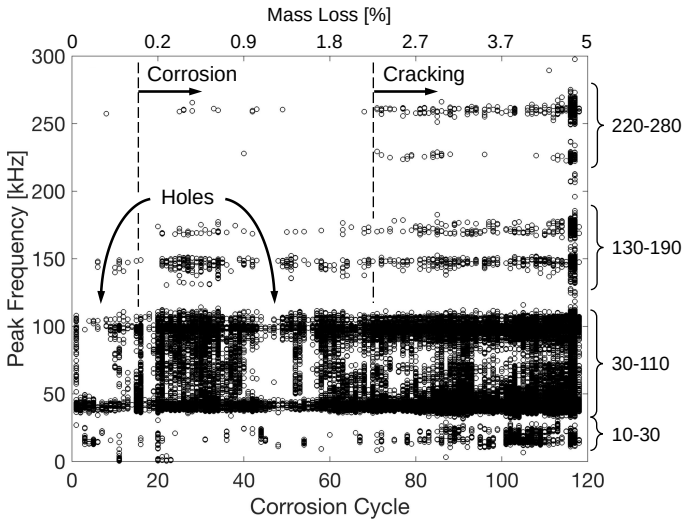

Fig. 5.5 Peak frequency datacloud for acoustic emission hits in the control specimen. Several frequency bands observed (indicated by brackets), suggesting the presence of various source mechanisms.

activity spike began at cycle 116 and continued through cycle 117. Since this spike occurred after Crack 1 extended through the entire length of concrete cover, it may be related to propagation of one (or both) of the angled subsurface cracks (*i.e.*, Crack 2 or 3).

21.3.2 Peak frequency analysis

To further distinguish the various AE activity spikes, the peak frequency for each hit recorded over the entire corrosion process is shown in Fig. 5.5. A number of distinct frequency bands may be seen in the datacloud, indicating that various mechanisms occurred during corrosion. Four main frequency bands may be observed in the concrete, appearing in the ranges 10-30, 30-110, 130-190, and 220-280 kHz (indicated in Fig. 5.5). It may be seen that these bands did not all emerge at the same point in the corrosion process. For instance, the 10-30 kHz band showed some activity near the start of the test, but did not emerge strongly until around cycle 70. This was at the point when the first minor spike in AE activity was observed. The 30-110 kHz band appeared immediately, and remained present during the entire corrosion

process. The 130-190 kHz band appeared slightly later around cycle 20, soon after corrosion onset. Lastly, the 220-280 kHz band did not emerge strongly until around cycle 70, again near the first minor spike. Interestingly, there was some degree of fusion within the 30-110 kHz band, causing the opening and closing of holes within this band as corrosion progressed. As indicated in Fig. 5.5, two dominant holes may be seen in cycles 1-20 and 40-60 (roughly), which are investigated in the next section.

The emergence of frequency content between 40-90 kHz (thus closing holes in the 30-110 kHz band) appeared to be linked to mechanisms during corrosion onset. Such frequency content was also found by Di Benedetti, *et al.* [55] near the corrosion onset point. Although the precise source is unknown, one possibility may be passive layer breakdown and/or expansion of corrosion products into the porous interface. The appearance of the 130-190 kHz band near cycle 20 (*i.e.*, shortly after corrosion onset) suggests that these were associated with corrosion mechanisms occurring prior to crack initiation. Considering data reported on similar frequency content in the literature [41, 54], a likely candidate is pitting in the strand. In combination with the minor spike near cycle 70, the strong emergence of the 220-280 kHz band near the same cycle points to these being associated with concrete cracking. Along with the observed spike patterns in AE activity, the fact that these bands remained from cycle 70 onward suggests that crack propagation took place rapidly near cycles 70, 90, 103, 116, and 117, and gradually during the intermediate cycles. From these considerations of AE activity and frequency content, the deduced start of cracking at cycle 70 is indicated in Figs. 5.4 and 5.5.

21.3.3 RA/AF analysis

To more thoroughly confirm whether the 220-280 kHz band was associated with concrete cracking (*i.e.*, crack opening, or tensile cracking), risetime/amplitude-average frequency (RA/AF) analysis was carried out. It is suggested [122] that such analysis be done on a moving average of data points, as opposed to on individual data

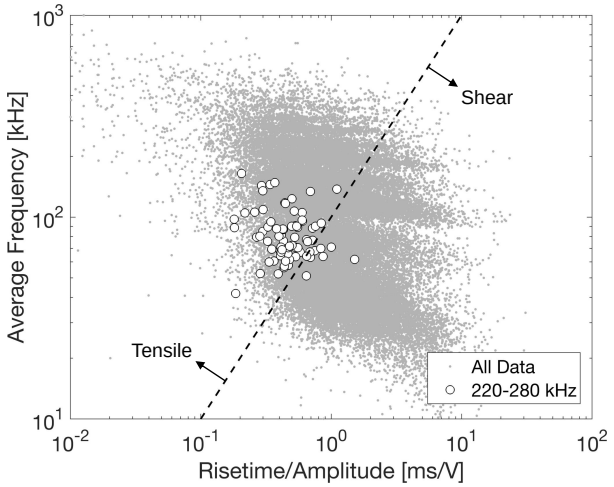

Fig. 5.6 Moving average RA/AF dataclouds for the 220-280 kHz band and entire dataset. Boundary between tensile and shear cracking overlain, classifying the 220-280 kHz band as a crack opening mechanism.

points themselves. A moving average group of 50 data points was therefore taken. The dataset was then split into groups of 50 data points each, from which average risetime/amplitude (RA) and average frequency (AF) values were computed.

Figure 5.6 shows the resulting RA/AF distribution for the 220-280 kHz band. For reference, the distribution for the moving average grouping applied to the entire dataset is also shown. Finally, overlain in the figure is the line defining $RA/AF = 1/100$, equivalent to $\log(AF) = \log(RA)+2$ in the logarithmic scale shown in the figure. This is a reasonable estimate of the demarcation between tensile and shear cracking [105, 106]. It may be seen that the large majority of the 220-280 kHz datacloud falls on the side of tensile cracking. Therefore, this result supports the conclusion formed from the peak frequency analysis that this band is associated with a crack opening mechanism in the concrete.

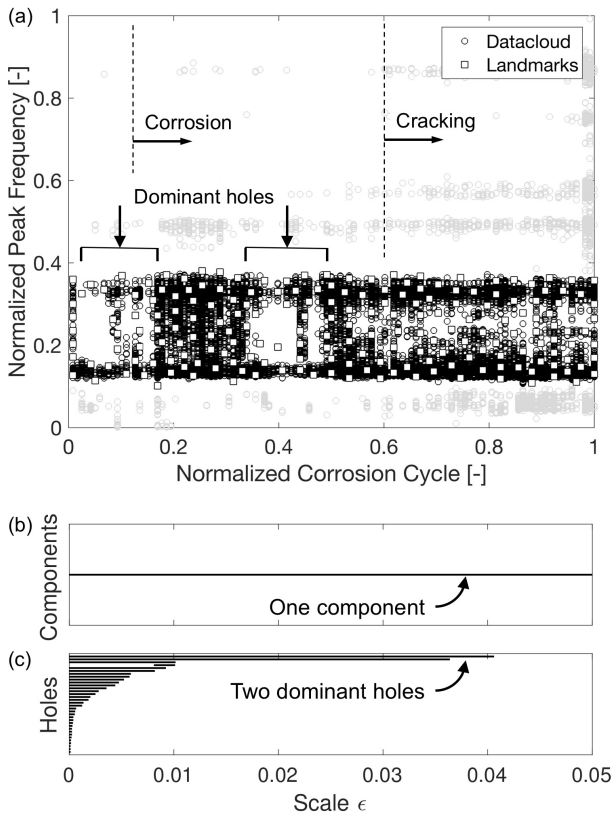

Fig. 5.7 Topological data analysis of the 30-110 kHz frequency band in the control specimen. (a) Datacloud with dominant holes highlighted, with data points from remaining bands overlain in light gray. (b),(c) Barcodes, indicating one component and two dominant holes.

22 Topological Data Analysis

In the previous section, AE activity trends, peak frequency bands, and RA/AF analysis were used to identify corrosion onset and concrete cracking in the control specimen. However, it appeared that missing frequency content, which formed holes in the 30-110 kHz band, may also be related to corrosion mechanisms. TDA was therefore used to quantitatively extract the holes from this band, allowing further conclusions to be drawn about their significance.

The extraction of holes in this frequency band using TDA is shown in Fig. 5.7. For reference, the data points in the considered frequency band are shown in black in Fig. 5.7(a), with those from all other frequency regions shown in light gray. To

ensure that the coordinates of the data points had compatible units for use in TDA, the corrosion cycle and peak frequency axes were normalized (*i.e.*, mapped) from their original ranges of $[0, 118]$ and $[0, 300]$, respectively, to $[0, 1]$. It was found that 200 landmarks for the witness complex provided a good description of the datacloud, as seen in Fig. 5.7(a). Further investigation of the optimal number of landmarks for this datacloud may be found below. From the given number of landmarks, the barcodes for components and holes may be seen in Fig. 5.7(b) and (c). One component was obtained in Fig. 5.7(b), representing the observable topology of the single band under consideration. The presence of two dominant holes may be seen in Fig. 5.7(c), corresponding to the two holes indicated in Fig. 5.7(a). It may be seen in Fig. 5.7(c) that various lesser dominant holes were also detected, revealing the relatively small scattered holes seen in the datacloud. However, these are treated as noise since their barcodes were significantly shorter than those for the two dominant holes.

In order to verify that 200 landmarks accurately captured the topology of the datacloud, the sensitivity of the barcodes with respect to the number of landmarks was investigated. Accordingly, Fig. 5.8(b) shows the barcodes for holes obtained from three different numbers of landmarks, including 50, 100, and 200. For visualization, Fig. 5.8(a) shows the landmarks for each case overlain on the datacloud. Using only 50 landmarks provided a poor encapsulation of the datacloud, and the resulting barcode shows that only one of the two holes was identified. Using 100 landmarks yielded improved results, where the existence of two dominant holes began to emerge. By 200 landmarks, the barcode converged to indicate the two dominant holes. This process therefore confirms that 200 landmarks provided an accurate result for Fig. 5.7. Although 200 landmarks may only apply to the present experiment, it is also demonstrated that the appropriate number of landmarks for any given experiment may be found by studying the convergence of barcodes. Moreover, even though the topological accuracy will only increase with an increasing number of landmarks, a trade-off may need to be made between accuracy and computation time. Using a

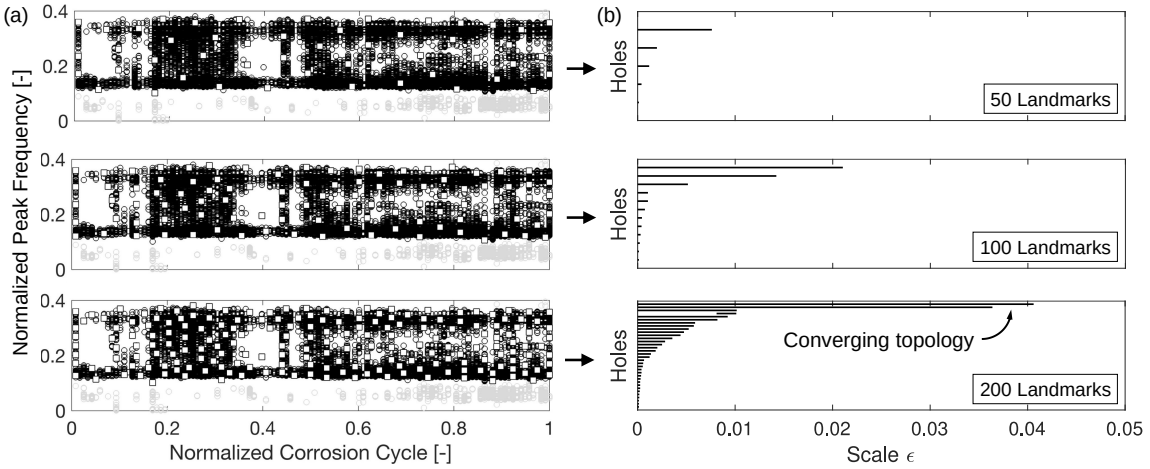

Fig. 5.8 Comparison of barcodes obtained from various numbers of landmarks. (a) Landmark selection overlain on the datacloud for 50 (top), 100 (middle), and 200 (bottom) landmarks. (b) Corresponding barcodes for 50, 100, and 200 landmarks. Converging topology of two dominant holes observed by 200 landmarks.

desktop PC, the computation times for the three cases shown in Fig. 5.8 were 2.4, 10.7, and 45.1 seconds, respectively.

These results demonstrate the ability of TDA to quantify holes in the AE datacloud for the 30-110 kHz frequency band. However, this specific framework is only able to determine the presence of holes, and not their locations within the datacloud (*e.g.*, the corrosion cycles in which they are present). Moreover, the results are only useful for offline analysis (after the entire corrosion process is completed), and is therefore not ideal for real-time monitoring. To overcome these limitations, an online cycle-by-cycle framework is proposed below.

22.1 Cycle-by-cycle TDA framework

The cycle-by-cycle framework is visualized in Fig. 5.9 for two corrosion cycles, with and without a hole, respectively. The framework involves taking a slice of the datacloud at each cycle and determining hole presence based on the number of components in the slice. First, for simplicity, the peak frequency datacloud for a given cycle is normalized, such that the range $[30, 110]$ kHz is mapped to $[-1, 1]$. The presence of a hole at a given cycle is then governed by whether or not there are at least two sig-

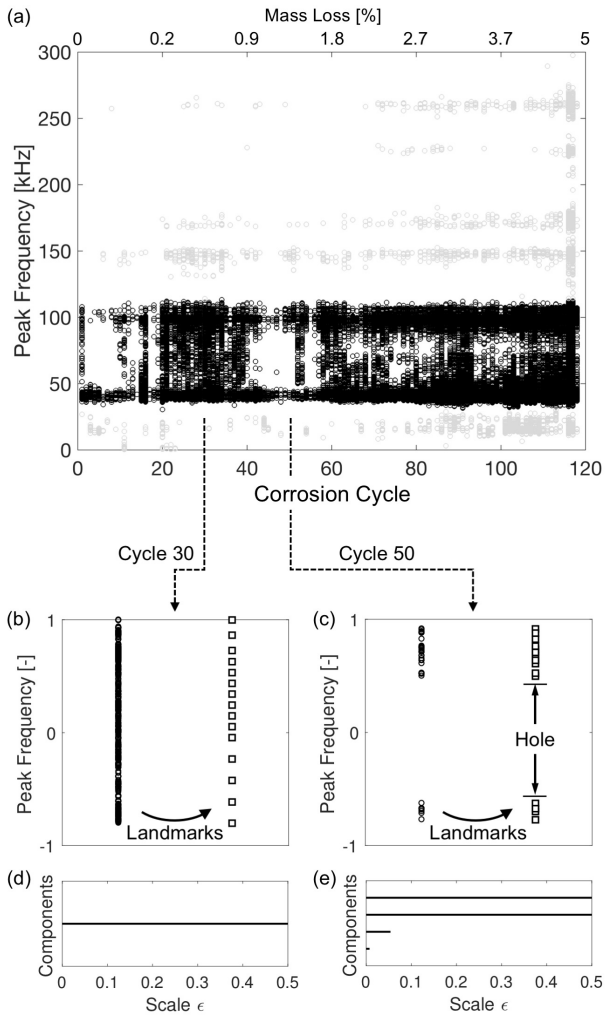

Fig. 5.9 Illustration of cycle-by-cycle TDA framework for hole measurement at two cycles based on the number of components. (a) Datacloud for 30-110 kHz frequency band highlighted. (b),(c) Selection of landmarks for cycles 30 and 50. (d),(e) Barcodes for number of components at cycles 30 and 50. Cycle 30 does not have a hole since it has only one significant component. Cycle 50 has a hole since it has at least two components which exist until $\varepsilon = \varepsilon^{\star}$ (0.5 here).

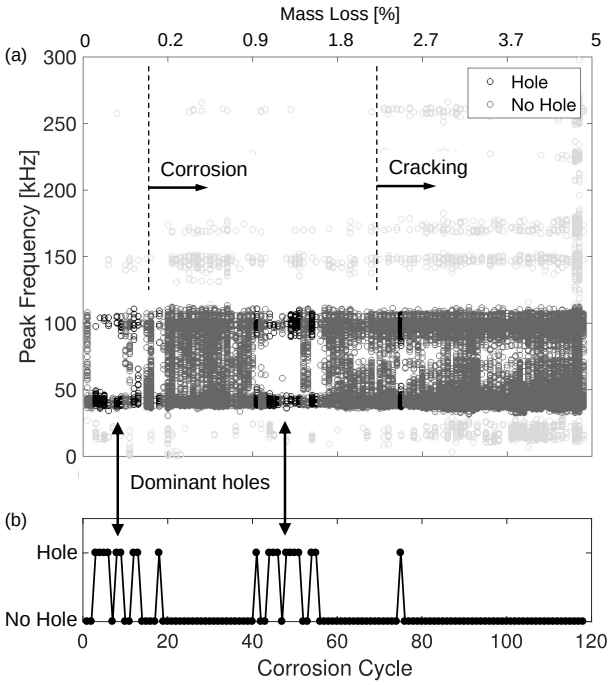

Fig. 5.10 Topological data analysis results for hole measurement at each cycle in the control specimen. (a) Identified holes color coded in datacloud. (b) Binary hole presence with respect to corrosion cycle.

nificantly distanced components (*i.e.*, if the components exist over a sufficient scale). For illustration, a hole is said to be present if they exist up to a scale of $\varepsilon^\star = 0.5$ in normalized frequency (*i.e.*, 20 kHz in original frequency). The dependence of the results for various values of $\varepsilon^\star$ is studied afterward. Determination of hole presence using this approach may be seen in Fig. 5.9(d) and (e). Since the witness complex is only applied to a 1D slice of the original 2D datacloud, the number of landmarks is set to 15. This is determined from the following dimensionality-based reasoning: if 200 landmarks are required to cover a 2D space, then $\sqrt{200} \approx 15$ are required to cover a 1D slice of that space. The selection of landmarks from slices of the datacloud may be seen in Fig. 5.9(b) and (c).

Results of the cycle-by-cycle TDA hole measurement may be seen in Fig. 5.10. Here, the datacloud is color coded based on the hole presence at given cycles. As in Fig. 5.7(a), those data points which are outside the 30-110 kHz band are colored in light gray. The two main holes from cycles 1-20 and 40-60 are identified, as well as

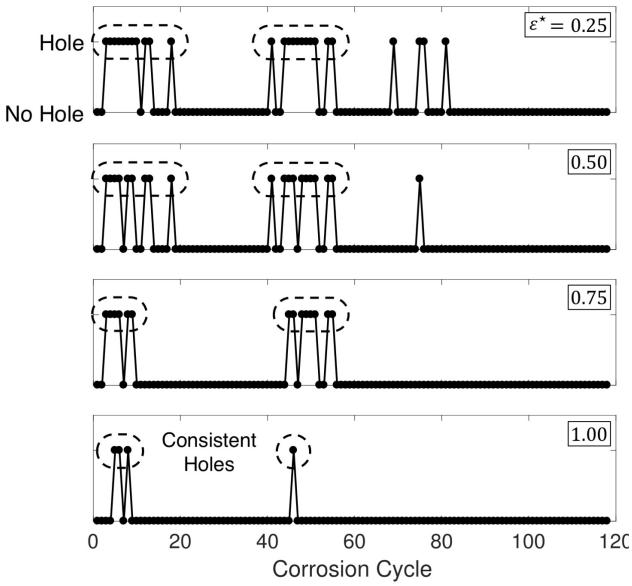

Fig. 5.11 Results of cycle-by-cycle framework for various values of $\varepsilon^\star$. Only the dominant holes near cycles 1-20 and 40-60 consistently appear across a range of $\varepsilon^\star$ values.

lesser-dominant holes around cycle 70-80. However, since the minor hole around cycle 70-80 is less definitive, it is unclear if it is meaningful or simply noise. Considering Fig. 5.10, it may be seen that the closure of the first hole was correlated with corrosion onset. The presence of a hole before this point may point to a lack of variety in source mechanisms. Once corrosion begins, however, new mechanisms may take place involving the strand (such as passive film breakdown or corrosion product expansion), producing frequency content between 40-90 kHz and closing the hole. From roughly cycle 20-40, immediately after corrosion onset, the hole remained strongly closed. This correlates with corrosion products building up around the strand from the model in Fig. 1.3. Along with the AE activity analysis, the second hole near cycle 40-60 may be an indication of the corrosion rate slowing due to the buildup of corrosion products (as discussed in [7]), again resulting in less variety of source mechanisms. However, the closing of this hole near cycle 60 appears to serve as an early indication of crack initiation.

To study the influence of $\varepsilon^\star$ on the cycle-by-cycle framework, analogous results for a variety of $\varepsilon^\star$ values were computed, as shown in Fig. 5.11. Here, results for four

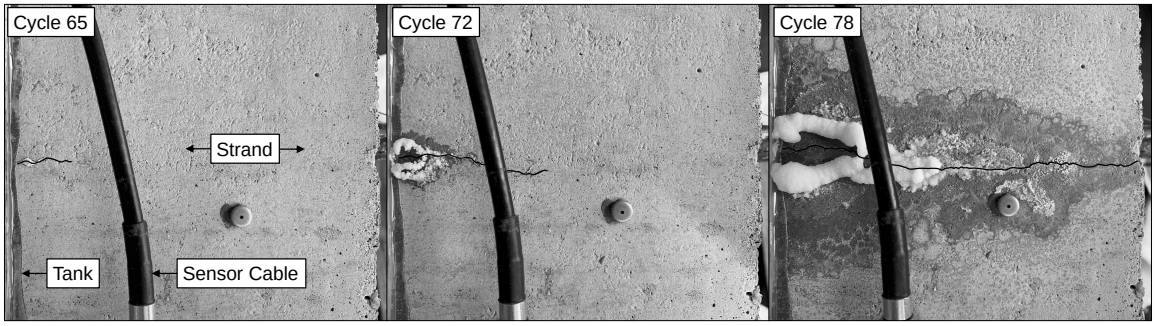

Fig. 5.12 Corrosion-induced propagation of surface microcracking in the weathered specimen. Crack highlighted in black.

values are shown, within the wide range of [0.25,1]. For a small value of $\varepsilon^\star = 0.25$, it may be seen that the definition of a hole is not sufficiently strict. On the contrary, as the value reaches 1, the definition of a hole becomes overly strict. By studying a wide range of values, it may be seen that the two dominant holes are the only ones present throughout the entire range. The consistency of these holes identifies them as dominant, while demonstrating that a wide range of $\varepsilon^\star$ may be studied in order to identify true holes within this framework. Although various values are satisfactory for hole determination, selecting $\varepsilon^\star = 0.75$ provides the greatest agreement with the least noise.

Lastly, to illustrate the computation time of the cycle-by-cycle framework, the cycle with the largest AE activity rate (*i.e.*, highest number of hits/time) was selected. This was cycle 116, which contained 134,078 hits over a time period of 7 hours. In this case, the required computation time was 0.4 seconds on a PC, demonstrating that there would be no issue performing TDA in real-time on this data.

22.2 Weathering effects

Having established the traditional and TDA-based analysis approaches for the control specimen, this subsection considers their evaluation on the weathered specimen. Of interest are the generalizability of the approach and the effects of weathering on corrosion in particular.

To first establish benchmark points for corrosion onset and concrete crack initiation, visual inspection and traditional AE analysis were jointly considered, as in Sec. 21. As with the control specimen, no visual signs of corrosion were observed until a relatively late stage in testing. The first sign was observed at cycle 65 when saltwater began seeping from a surface crack running from the tank edge. This occurred on the rightward side of the specimen, and the crack extended the entire length of the rightward half by cycle 78, as shown in Fig. 5.12. An analogous crack opening was also observed on the leftward edge of the tank at cycle 65. This crack completely extended through the leftward half by cycle 97. There was thus a full cover crack in the concrete by cycle 97, and data collection was stopped soon after at cycle 104.

AE activity analysis was used to first identify corrosion onset, as seen in Fig. 5.13(a) in its cumulative form. The first spike in activity began at cycle 8 (*i.e.*, $c_{\mathrm{d}} = 8$). This agreed well with the peak frequency distribution shown in Fig. 5.13(b), where the pitting corrosion activity (130-190 kHz) emerged near the same point. The next significant spike in AE activity occurred near cycle 60, suggesting the initiation of concrete cracking. Indeed, this point corresponded with the first visual signs appearing at the concrete surface, where preexisting microcracks running parallel to the strand began to open slightly. In addition, the spike near cycle 60 also coincided with the emergence of 220-280 kHz frequency content (proposed to be related to concrete cracking).

As seen from Fig. 5.13, the onset of corrosion began slightly earlier (by seven cycles) in the weathered specimen. It is likely that this is due to the specimen having already spent 2.5 years outdoors, gradually accumulating aggressive agents within the concrete. The slightly earlier initiation of concrete cracking (by ten cycles) is then consistent with the earlier corrosion onset. However, it is interesting what effect the surface microcracking has on corrosion. These preexisting cracks appeared to allow corrosion-induced crack initiation at the outer surface, in addition to the expected location at the strand-concrete interface. This resulted in significantly earlier surface

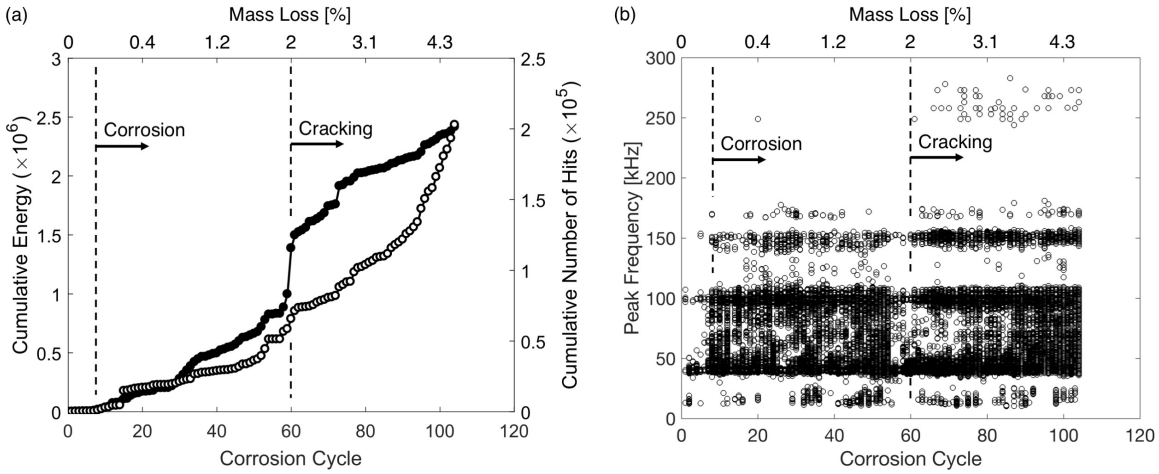

Fig. 5.13 (a) Acoustic emission activity recorded in the weathered specimen, in terms of cumulative energy and number of hits. (b) Peak frequency datacloud for acoustic emission hits in the weathered specimen.

crack propagation.

With the benchmark study completed, Fig. 5.14 shows the results of the cycle-by-cyle TDA framework applied to the AE data obtained from the weathered specimen. The points of corrosion onset and crack initiation are overlain here. It may be seen that the same 30-110 kHz band (found in the control specimen) was present in the peak frequency datacloud. This band is highlighted with darker colors in Fig. 5.14, where the black and dark gray coloring distinguishes cycles with and without holes, respectively. The framework is applied with $\varepsilon^\star = 0.75$, which was determined as the optimal value from the control specimen in Sec. 22.1.

It may be seen from Fig. 5.14 that both the size of the hole (in the peak frequency dimension) and the correlation with corrosion onset remain present in the weathered specimen. It is interesting, however, that there is no second hole preceding crack initiation, as was the case for the control specimen. The early warning provided by the hole in the control specimen therefore does not appear to generalize to weathered and microcracked specimens. Nevertheless, these results suggest that TDA possesses a high reliability in corrosion onset determination, and may be advantageous when combined with traditional AE analysis.

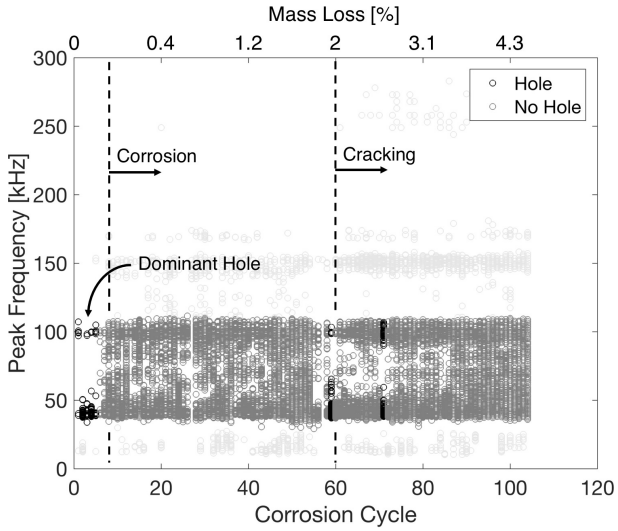

Fig. 5.14 Cycle-by-cycle topological data analysis for the weathered specimen. (a) Identified holes color coded in datacloud. (b) Binary hole presence with respect to corrosion cycle.

23 Hidden Markov Modeling

Aside from AE activity, the 130-190 kHz band and the hole in the 30-110 kHz band have been shown to indicate corrosion onset in this thesis. In addition, the 220-280 kHz band was shown to indicate concrete cracking. The fact that this collection of features alone can indicate corrosion mechanisms motivates pursuing their use for automated corrosion diagnostics without the need to rely on AE activity (which may be prone to contamination). The hidden Markov modeling outlined in Sec. 15 was therefore adapted to this purpose. In particular, data from the control specimen was used to train a HMM, with the weathered specimen then used to test the HMM in probabilistically synthesizing the traditional and topological AE features.

23.1 Model selection

23.1.1 States

Before the parameters of the HMM were trained, physical insight was leveraged to impose constraints on the model. This helped simplify and reduce the amount of parameters that were trained. For simplicity, a 3-state model was taken, with the states

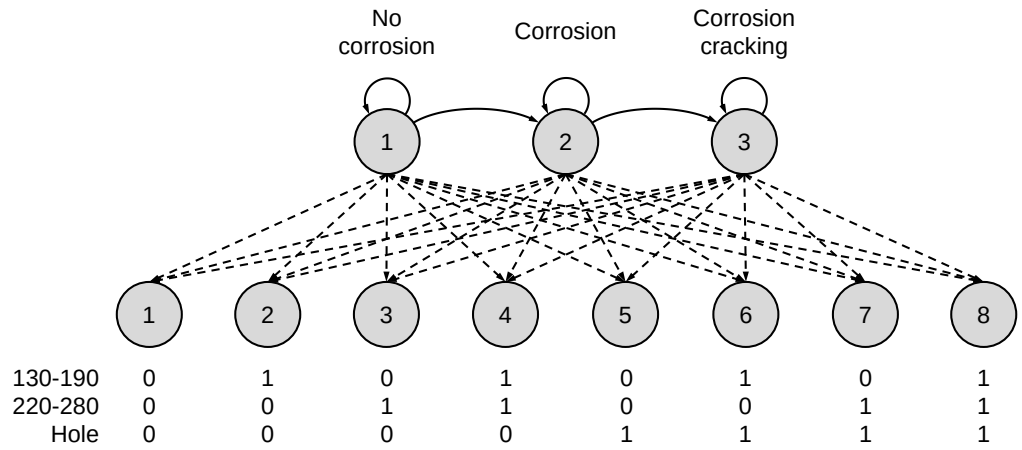

Fig. 5.15 Hidden Markov model definition for states and observations. Solid and dashed lines indicate nonzero probability. Binary coding scheme for each of the eight observations is detailed.

corresponding to no corrosion, corrosion, and corrosion-induced concrete cracking.

The first physical assumption incorporated into the model was that corrosion only progresses, it does not regress. Therefore, a left-right model was adopted, where backward state transitions were not allowed: $A_{ij} = 0$ for $i < j$. The ordering of states was therefore taken as: (1) no corrosion; (2) corrosion; and (3) corrosion-induced cracking.

A second assumption was that corrosion mechanisms cannot be skipped. For instance, the corrosion-induced cracking comprising State 3 cannot be reached unless the corrosion in State 2 has been reached. This constraint was incorporated as follows: $A_{ij} = 0$ for $j > i + 1$. Combined with the previous assumptions, the state transition matrix has the following form:

$$\mathbf{A} = \begin{bmatrix} A_{11} & A_{12} & 0 \\ 0 & A_{22} & A_{23} \\ 0 & 0 & A_{33} \end{bmatrix} \tag{5.2}$$

23.1.2 Observations

The traditional and topological AE features were then incorporated into observations for the 3-state HMM. For simplicity, the AE features were discretized into a binary coding scheme. At each time step, there are three possible binary outcomes: (1) in the 130-190 kHz band there are either no hits or at least one hit; (2) in the 220-280 kHz band there are either no hits or at least one hit; and (3) there is either a hole in the 30-100 kHz band or there is not. Combining the three binary outcomes leads to one of eight possible observations at each time step. This binary scheme was assumed to be appropriate for characterizing activity in the frequency bands, since it is posited that what is important is not the amount of hits in each band but the sustained presence of hits over time. To support arbitrary corrosion rates i_{cor}, the bin width for the time steps was voluntarily taken as the normalized value $b = 25 \times 10^{-3}$ $\mu\text{A}\cdot\text{cm}^{-2}\cdot\text{yr}$. This value was adopted to provide a reasonable time-step resolution (*e.g.*, the training specimen spanned roughly 500 units). For reference, with natural corrosion rates on the order of 1 $\mu\text{A/cm}^2$ [11, 18, 123], this would yield roughly one time step every nine days. The resulting HMM is visualized in Fig. 5.15 showing state and observation definitions.

23.2 Model training

With b taken as above, the control specimen yielded $T = 513$ time steps for the training sequence. The training state sequence was measured from the corrosion onset and crack initiation points determined in Sec. 21. In addition, the training observation sequence was measured from the binned AE data for that specimen.

23.2.1 Parameter estimation

It was first assumed that there is no knowledge about which state the corrosion process starts in. The initial distribution was therefore estimated as $\boldsymbol{\pi}^0 = [\frac{1}{3}\ \frac{1}{3}\ \frac{1}{3}]$. Since there was only one corrosion sequence (*i.e.*, specimen) available for training,

the above distribution was not trained. The trained value for the initial distribution was therefore taken as

$$\boldsymbol{\pi} = \begin{bmatrix} \frac{1}{3} & \frac{1}{3} & \frac{1}{3} \end{bmatrix} \tag{5.3}$$

To estimate the transition probability matrix, the mean duration of each state was first estimated. With only one training sequence, the mean duration was taken as the sample duration for each state. However, since no transitions are allowed from the final state, the corresponding sample duration was taken as infinity. The transition probability matrix was then estimated according to Eqs. (3.32) and (3.33). After $K = 100$ iterations of the Baum-Welch algorithm (see Sec. 15.1) this was trained to

$$\mathbf{A} = \begin{bmatrix} 0.971 & 0.029 & 0 \\ 0 & 0.995 & 0.005 \\ 0 & 0 & 1 \end{bmatrix} \tag{5.4}$$

Lastly, the observation probabilities were estimated according to Eq. (3.34). These were also then trained using 100 iterations. However, special care was taken to avoid zero-valued probabilities for observations which were simply not recorded in the training sequence. Specifically, trained observations with zero probability were first set to a small value of 1×10^{-3}. Each row of the trained observation probability matrix was then normalized to a unit sum to ensure they were valid probability measures. The trained probability matrix was then

$$\mathbf{B} = \begin{bmatrix} 0.398 & 0.048 & 0.001 & 0.001 & 0.437 & 0.095 & 0.019 & 0.001 \\ 0.290 & 0.317 & 0.010 & 0.034 & 0.237 & 0.093 & 0.009 & 0.010 \\ 0.143 & 0.202 & 0.051 & 0.375 & 0.072 & 0.090 & 0.024 & 0.043 \end{bmatrix} \tag{5.5}$$

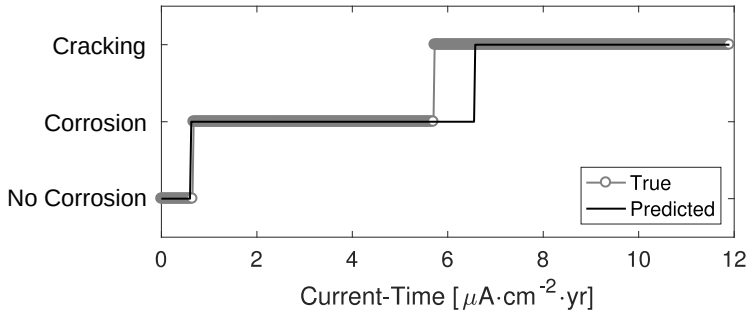

Fig. 5.16 Comparison of true and predicted corrosion state sequence using hidden Markov modeling.

23.3 Model testing for corrosion diagnostics

AE data recorded from the weathered specimen was used for testing the trained HMM. This data was binned into a uniform-interval time axis, from which an observation sequence and a true state sequence were generated. The bin width was taken as the same value used for training in the previous subsection (*i.e.*, 25×10^{-3} μA·cm^{-2}·yr) and yielded a testing sequence of length $T = 477$. The Viterbi algorithm described in Sec. 15.2 was then used to decode the observation sequence into a predicted state sequence. A comparison of the true and predicted state sequences may be seen in Fig. 5.16.

Figure 5.16 shows excellent agreement for the corrosion onset point in the true and predicted state sequences. Although there is some disagreement in the exact point of crack initiation between the two sequences, the general point of concrete cracking is also predicted well by the HMM. The fact that better agreement was found for corrosion onset may be due to the fact that two AE features were indicative of corrosion onset, while only one was indicative of cracking. It may also be noted that the HMM correctly identified the starting state as "no corrosion," even though it was designed without such information. This demonstrates the value of the HMM under real-world scenarios where this information may be unknown.

24 Summary

This chapter demonstrated an automated diagnostic approach with potential for real-time corrosion monitoring in prestressed concrete. The probabilistic approach relied on various information gained from traditional and topological analyses of AE data. Specifically, a HMM was used to combine this information, with it being trained on a control specimen and evaluated on a weathered specimen with typical in-field conditions.

The topology of the main frequency band (spanning 30-110 kHz) correlated reliably with corrosion onset. It was suggested that this feature may be related to corrosion product expansion around the embedded prestressing strand. Moreover, it was shown that topological computation could be performed significantly faster than the continuous recording of AE data, thus validating the potential for real-time monitoring. Two other frequency bands were also associated with corrosion. Frequencies in the 130-190 kHz range correlated with corrosion onset, which is in accordance with suggestions in the literature that such content is related to pitting in the strand [18, 41]. Additionally, the 220-280 kHz was linked to concrete cracking and confirmed through RA/AF analysis.

Through these features, the HMM approach was shown to indicate corrosion onset and corrosion-induced crack initiation before external visual signs of corrosion were evident. The fact that the model does not rely on AE activity information strengthens its transitional potential from laboratory to field applications. In addition, a normalized current-time was used to accommodate future transitions from accelerated corrosion to natural corrosion rates.

CHAPTER 6

Conclusion

25 Overview and Contributions

This thesis demonstrated how harnessing complexities in acoustic data can enhance longterm autonomous corrosion monitoring in structures. This was shown in two manners through understanding and simplifying such complexities in steel strands and prestressed concrete.

First, tailoring the generation of guided waves (GWs) in strands was shown to isolate the desired corrosion-induced stress evolution from confounding geometric effects. This was due to the core-seeking nature of targeted higher-order GW modes, which limited their interaction with effects like surface roughness and material loss occurring mainly in the peripheral strand wires. Acoustoelasticity was advanced to properly describe the stress dependence of these modes, and various data processing techniques were adapted toward enabling reliable longterm stress measurement (including wavelet transforms, modal modulation, and data fusion). Modal modulation and data fusion, in particular, demonstrated how the multiplicity of higher-order modes may be leveraged toward improved measurements.

On the other hand, studying the topology of acoustic emission (AE) data in prestressed concrete furthered the understanding of complex corrosion-related information embedded in such data. A real-time adaptation of topological data analysis (TDA) was proposed for continuous monitoring, with the witness complex incorporated to achieve fast topological quantification on the large amount of recorded AE

data. The additional information unearthed in the data allowed new corrosion indicators to be gained. Specifically, the closure of a hole in the data coincided with corrosion onset, while high-frequency content in the 220-280 kHz range was linked to corrosion-induced concrete cracking. Lastly, the usefulness of hidden Markov modeling in combining insight from these complexities was demonstrated in automated corrosion diagnostics. In conjunction with degradation models [11, 20], these diagnostics have valuable applications in forecasting damage to prestressed concrete structures.

26 Recommendations

In the context of GWs, this thesis primarily focused on understanding the beneficial modes for stress monitoring, and how those benefits can be exploited. However, to achieve a wide range of practical applications, alternative sensing techniques should be investigated. These may allow higher-order modes to be transmitted through strands in a more flexible manner, as well as help tackle the issue of attenuation. Secondly, it may be noted that the tested specimen fractured at subyield stress (possibly due to hydrogen embrittlement [120]). It is therefore important to investigate how this approach may be modified to accommodate plastic strain. Even in the experiment presented here, it is possible that local areas near the strand surface became plastic due to nonuniformly distributed residual stress [124]. Some researchers have recently studied the effect of nonuniform stress on GWs [125, 126]. From these considerations, future work should also study GWs under plastic strain, while perhaps considering a nonuniform strain distribution.

The AE approach to prestressed concrete will significantly benefit from experimentation in large-scale specimens. In addition to the impact of realistic geometries [49], this may help evaluate the effect of multiple strands and reinforcing bars on the

automated diagnostic approach. Finally, it should be noted that TDA is an emerging computational tool, with new developments continually underway. For instance, strategies are being investigated for accommodating noisy data points [127], which may be considered for future work.

APPENDIX

A Tensor Analysis

A.1. Christoffel symbols

This subsection details various aspects of Christoffel symbols, summarized from [68]. For brevity, these are presented for the symbols Γ^k_{ij} of the predeformed body $\mathscr{B}$. Analogous relations hold for the symbols of an arbitrary body by replacing the metric tensors G_{ij}, G^{ij} and determinant G with those for the body under consideration.

First, Christoffel symbols have the following symmetry:

$$\Gamma^k_{ij} = \Gamma^k_{ji} \tag{A.1}$$

The following is a useful relation for computing a particular summation over Christoffel symbols:

$$\begin{aligned} \Gamma^i_{ij} &= \tfrac{1}{2} G^{ik} G_{ik,j} \\ &= \frac{G_{ik,j}}{2G} \frac{\partial G}{\partial G_{ik}} \\ &= \frac{(\sqrt{G})_{,j}}{\sqrt{G}} \end{aligned} \tag{A.2}$$

For orthogonal curvilinear coordinates (*e.g.*, cartesian or cylindrical coordinates), the symbols reduce to

$$\begin{aligned} &\Gamma^k_{ij} = 0 \quad (i \neq j \neq k \neq i) \\ &\Gamma^k_{ii} = -\frac{G_{ii,k}}{2G_{kk}} \quad (i \neq k) \\ &\Gamma^i_{ij} = \frac{G_{ii,j}}{2G_{ii}} \end{aligned} \tag{A.3}$$

For cartesian coordinates, the Christoffel symbols vanish, $\Gamma^k_{ij} = 0$. This reflects the fact that space described by Cartesian coordinates has no curvature.

A.2. Raising and lowering indices

It was seen that a vector $\mathbf{u}$ may be expressed in terms of either covariant or contravariant components. If the components are referenced to the undeformed body, then the vector may be written as either $\mathbf{u} = u_i\mathbf{g}^i$ or $u^i\mathbf{g}_i$. The covariant and contravariant components may therefore be related by incorporating Eqs. (2.5), (2.8), and (2.9),

$$\begin{aligned} u_i &= g_{ij}u^j \\ u^i &= g^{ij}u_j \end{aligned} \tag{A.4}$$

It may then be seen that when the components of a vector are referenced to the undeformed body, the indices may be raised or lowered by multiplying by the metric tensors for that body. Similarly, the vector components may be referenced to the deformed body as either $\mathbf{u} = U_i\mathbf{G}^i$ or $U^i\mathbf{G}_i$. The covariant and contravariant components U_i and U^i are therefore related by

$$\begin{aligned} U_i &= G_{ij}U^j \\ U^i &= G^{ij}U_j \end{aligned} \tag{A.5}$$

where the metric tensors G_{ij} and G^{ij} may be used to raise or lower indices when referenced to the deformed body. In a similar manner, the indices on an arbitrary second-order tensor (referenced to the undeformed body) may be raised or lowered as follows:

$$\begin{aligned} a^{ij} &= g^{ik}g^{jl}a_{kl} \\ a_{ij} &= g_{ik}g_{jl}a^{kl} \end{aligned} \tag{A.6}$$

Analogous equations may be written for a second-order tensor referenced to the de-

formed body using instead the metric tensors G_{ij}, G^{ij}.

B Structural Analysis

Linear-elastic structural analysis was carried out to convert the strain in the uncorroded segment to stress in the corroding segment in Sec. 17.3. To this end, the structural system formed by the strand and the loading frame is studied. In particular, since the axial stress in the strand is desired, the stiffness of the frame along the strand's axis is considered.

For axial deformation, the corroding and uncorroded segments of the strand may be idealized as springs with stiffnesses k_{c} and k_{uc}. Considering linear elasticity, the stiffnesses are

$$k_{\mathrm{c}} = \frac{EA_{\mathrm{c}}}{\ell_{\mathrm{c}}} \qquad k_{\mathrm{uc}} = \frac{EA_{\mathrm{uc}}}{\ell_{\mathrm{uc}}} \tag{B.1}$$

The stiffness of the corroding segment varies over the corrosion process due to cross-section loss (*i.e.*, change in A_{c}). However, since the uncorroded segment does not experience any cross-section loss, the stiffness k_{uc} was fixed and may be computed at 41.9 kN/mm.

As shown in Fig. B.1, the stiffness k_{fr} of the frame may be split into three parts: arm k_{arm}, rod k_{rod}, and bed k_{bed}. The arm may be modeled as a simply-supported beam under three-point bending, whose stiffness is found from Euler beam theory,

$$k_{\mathrm{arm}} = \frac{48EI_{\mathrm{arm}}}{\ell_{\mathrm{arm}}^3} \tag{B.2}$$

The stiffness of each rod is

$$k_{\mathrm{rod}} = \frac{EA_{\mathrm{rod}}}{\ell_{\mathrm{rod}}} \tag{B.3}$$

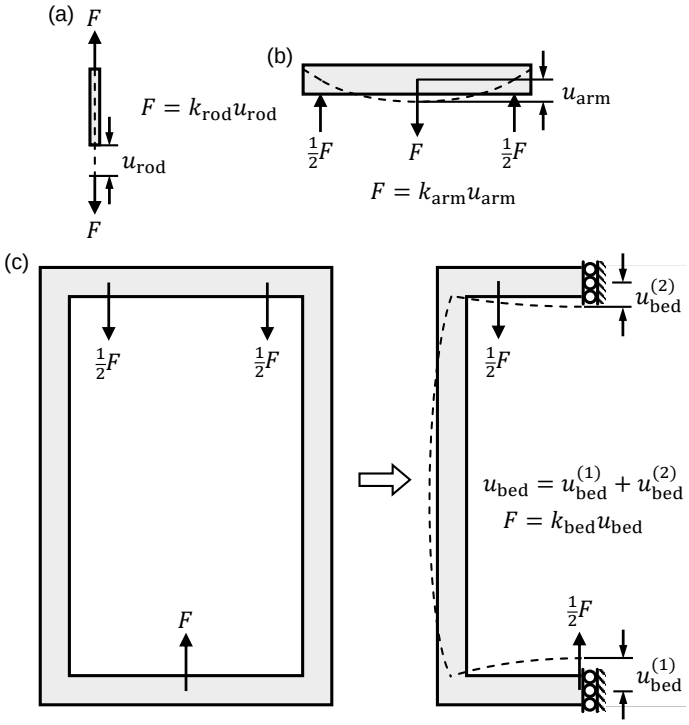

Fig. B.1 Components of frame undergoing deformation due to force F, illustrating their respective stiffnesses: (a) bed, (b) rod, and (c) arm.

where A_{rod} is the cross-sectional area of each rod, and ℓ_{rod} is the rod length. The bed stiffness may be derived by considering the displacement induced at the strand and rod connection points by a unit force F, as shown in Fig. B.1(c). Furthermore, the symmetry of the frame and loading may be exploited as shown in the figure. Denoting the absolute displacements at these points by $u_{\text{bed}}^{(1)}$ and $u_{\text{bed}}^{(2)}$, respectively, then the bed displacement is $u_{\text{bed}} = u_{\text{bed}}^{(1)} + u_{\text{bed}}^{(2)}$. Based on Euler beam theory (while considering axial deformation) the total bed displacement may be expressed

$$u_{\text{bed}} = \frac{bF\ell_{\text{bed}}^3}{120EI_{\text{bed}}} \tag{B.4}$$

where ℓ_{bed} is defined in Fig. 4.1(b), and the dimensionless parameter b is defined:

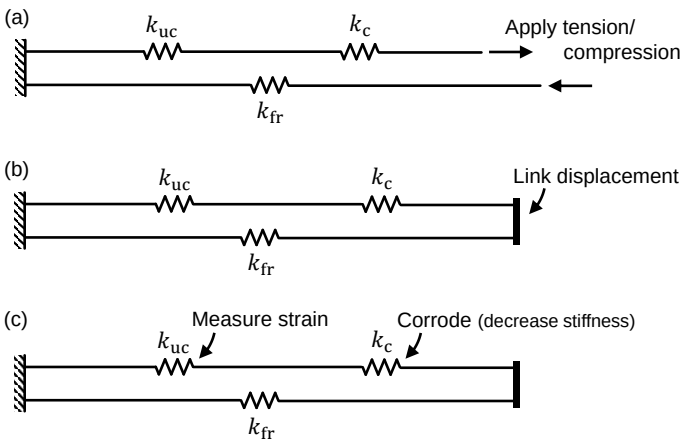

Fig. B.2 Representation of loading frame and strand segments (uncorroded and corroding) as springs k_f, k_{uc}, k_c. Stages of experiment: (a) strand loaded in tension, (b) displacement of system linked, (c) accelerated corrosion applied, decreasing stiffness in corroding segment, with strain measured in uncorroded segment.

$$b = 15 + \frac{240 I_{bed}}{A_{bed} \ell_{bed}^2} + \left(\frac{9 I_{bed}}{A_{bed} \ell_{bed}^2} - 2 \right) \left(\frac{\ell_{bed} - \ell_{off}}{\ell_{bed}} \right)^2 + 4 \left(\frac{\ell_{off}}{\ell_{bed}} \right) + 30 \left(\frac{\ell_{off}}{\ell_{bed}} \right)^2 - 12 \left(\frac{\ell_{off}}{\ell_{bed}} \right)^3 - 7 \left(\frac{\ell_{off}}{\ell_{bed}} \right)^4 \tag{B.5}$$

The bed stiffness is then defined from $F = k_{bed} u_{bed}$, with

$$k_{bed} = \frac{120 E I_{bed}}{b \ell_{bed}^3} \tag{B.6}$$

The frame stiffness may then be found in terms of its component stiffnesses ($2k_{rod}$, k_{arm}, and k_{bed}, placed in series) as

$$k_{fr} = \frac{2 k_{rod} k_{arm} k_{bed}}{2 k_{rod} k_{arm} + 2 k_{rod} k_{bed} + k_{arm} k_{bed}} \tag{B.7}$$

This may be evaluated as $k_{fr} = 66.5$ kN/mm. The fact that the frame and strand stiffnesses are comparable confirms that the deformation of the frame must be considered in the analysis.

The structural system (*i.e.*, frame and strand) is then equivalent to three springs k_c, k_{uc}, k_{fr}, arranged as shown in Fig. B.2. Before accelerated corrosion is applied, the

strand is loaded until the strain gages in the uncorroded segment reach e_{uc0}, as shown in Fig. B.2(a). The system is then held in this position by locking the threaded rods, which is equivalent to linking the displacements of the frame and strand, as shown in Fig. B.2(b). Finally, as shown in Fig. B.2(c), the strain in the uncorroded segment is monitored while accelerated corrosion is applied, which causes a reduction in the corroding segment stiffness.

As corrosion progressed, the strain in the uncorroded segment changed to $e_{\text{uc}} = e_{\text{uc0}} + \Delta e_{\text{uc}}$. The displacement change Δu_{uc} in this segment may then be obtained as

$$\Delta u_{\text{uc}} = \ell_{\text{uc}} \Delta e_{\text{uc}} \tag{B.8}$$

Since the stiffness k_{uc} of the uncorroded segment is fixed, the force change ΔF may be obtained as

$$\Delta F = k_{\text{uc}} \Delta u_{\text{uc}} \tag{B.9}$$

From the arrangement of the frame and strand, the force change in the frame is $-\Delta F$. With the frame stiffness k_{f} fixed, the frame displacement change Δu_{fr} may be found as

$$\Delta u_{\text{fr}} = -\frac{\Delta F}{k_{\text{fr}}} \tag{B.10}$$

From the linked displacement conditions, the displacement change Δu_{c} in the corroding segment is

$$\Delta u_{\text{c}} = \Delta u_{\text{fr}} - \Delta u_{\text{uc}} \tag{B.11}$$

Combining the above equations, the strain in the corroding segment may then be related to that in the uncorroded segment as

$$\Delta e_{\mathrm{c}} = -\left(1 + \frac{k_{\mathrm{uc}}}{k_{\mathrm{fr}}}\right)\frac{\ell_{\mathrm{uc}}}{\ell_{\mathrm{c}}}\Delta e_{\mathrm{uc}} \tag{B.12}$$

Considering linear elasticity, the uncorroded and corroding segment stress changes, denoted $\Delta\tau_{\mathrm{uc}}$ and $\Delta\tau_{\mathrm{c}}$, may be found as

$$\begin{aligned} \Delta\tau_{\mathrm{uc}} &= E\Delta e_{\mathrm{uc}} \\ \Delta\tau_{\mathrm{c}} &= -\left(1 + \frac{k_{\mathrm{uc}}}{k_{\mathrm{fr}}}\right)\frac{\ell_{\mathrm{uc}}}{\ell_{\mathrm{c}}}E\Delta e_{\mathrm{uc}} \end{aligned} \tag{B.13}$$

REFERENCES

[1] G. H. Koch, M. P. H. Brongers, N. G. Thompson, Y. P. Virmani, and J. H. Payer, "Corrosion Costs and Preventative Strategies in the United States," tech. rep., Feredal Highway Administration, 2001.

[2] N. G. Thompson, M. Yunovich, and D. Dunmire, "Cost of corrosion and corrosion maintenance strategies," *Corrosion Reviews*, vol. 25, no. 3-4, pp. 247–261, 2007.

[3] J. P. Broomfield, *Corrosion of Steel in Concrete*. London: Taylor & Francis, 2nd ed., 2007.

[4] W. Podolny, "Corrosion of prestressing steels and its mitigation," *PCI J.*, vol. 37, no. 5, pp. 34–55, 1992.

[5] M. S. Darmawan and M. G. Stewart, "Effect of pitting corrosion on capacity of prestressing wires," *Mag. Concrete Res.*, vol. 59, no. 2, pp. 131–139, 2007.

[6] G. Song, Y. Zheng, and B. Wu, "Emerging construction materials and sustainable infrastructure," *Appl. Sci.*, vol. 9, p. 4127, 2019.

[7] R. E. Melchers and C. Q. Li, "Phenomenological modeling of reinforcement corrosion in marine environments," *ACI Mater. J.*, vol. 103, no. 1, pp. 25–32, 2006.

[8] A. S. Sason, "Evaluation of degree of rusting on prestressed concrete strand," *PCI J.*, vol. 37, no. 3, pp. 25–30, 1992.

[9] R. A. Reis, "Corrosion Evaluation and Tensile Results of Selected Post-Tensioning Strands at the SFOBB Skyway Seismic Replacement Project – Phase III Report," tech. rep., Materials Engineering and Testing Services, 2007.

[10] A. Farhidzadeh and S. Salamone, "Reference-free corrosion damage diagnosis in steel strands using guided ultrasonic waves," *Ultrasonics*, vol. 57, pp. 198–208, 2015.

[11] M. S. Darmawan and M. G. Stewart, "Spatial time-dependent reliability analysis of corroding pretensioned prestressed concrete bridge girders," *Structural Safety*, vol. 29, no. 1, pp. 16–31, 2007.

[12] K. Tuutti, "Corrosion of Steel in Concrete," tech. rep., Swedish Cement and Concrete Research Institute, 1982.

[13] J. G. Cabrera, "Deterioration of concrete due to reinforcement steel corrosion," *Cement and Concrete Composites*, vol. 18, no. 1, pp. 47–59, 1996.

[14] P. Ziehl and M. ElBatanouny, "Low-Level Acoustic Emission (AE) in the Long-Term Monitoring of Concrete," in *Acoustic Emission (AE) and Related Non-Destructive Evaluation (NDE) Techniques in the Fracture Mechanics of Concrete* (M. Ohtsu, ed.), ch. 11, pp. 217–236, Cambridge: Woodhead, 1st ed., 2015.

[15] C. Andrade, C. Alonso, and F. J. Molina, "Cover cracking as a function of bar corrosion: Part I-Experimental test," *Mater. Struct.*, vol. 26, no. 8, pp. 453–464, 1993.

[16] C. Alonso, C. Andrade, J. Rodriguez, and J. M. Diez, "Factors controlling cracking of concrete affected by reinforcement corrosion," *Materials and Structures*, vol. 31, no. 7, pp. 435–441, 1998.

[17] S. A. Austin, R. Lyons, and M. J. Ing, "Electrochemical behavior of steel-reinforced concrete during accelerated corrosion testing," *Corrosion*, vol. 60, no. 2, pp. 203–212, 2004.

[18] F. Li, Y. Yuan, and C.-Q. Li, "Corrosion propagation of prestressing steel strands in concrete subject to chloride attack," *Constr. Build. Mater.*, vol. 25, no. 10, pp. 3878–3885, 2011.

[19] R. E. Weyers, "Service life model for concrete structures in chloride laden environments," *ACI Mater. J.*, vol. 95, no. 4, pp. 445–451, 1998.

[20] T. El Maaddawy and K. Soudki, "A model for prediction of time from corrosion initiation to corrosion cracking," *Cement Concrete Comp.*, vol. 29, no. 3, pp. 168–175, 2007.

[21] B. H. Oh, K. H. Kim, and B. S. Jang, "Critical corrosion amount to cause cracking of reinforced concrete structures," *ACI Mater. J.*, vol. 106, no. 4, pp. 333–339, 2009.

[22] M. D. Pandey and M. A. Nessim, "Reliability-based inspection of post-tensioned concrete slabs," *Can. J. Civil Eng.*, vol. 23, no. 1, pp. 242–249, 1996.

[23] C. MacDougall and S. Li, "Determining broken wires in unbonded seven-wire strands using penetration tests," *PCI J.*, vol. 52, no. 5, pp. 96–104, 2007.

[24] ASTM, "ASTM C876 – Standard Test Method for Corrosion Potentials of Uncoated Reinforcing Steel in Concrete," 2015.

[25] W.-B. Na, T. Kundu, and M. R. Ehsani, "Lamb waves for detecting delamination between steel bars and concrete," *Comput.-Aided Civ. Inf. Eng.*, vol. 18, no. 1, pp. 58–63, 2003.

[26] H. Kwun, K. A. Bartels, and J. J. Hanley, "Effects of tensile loading on the properties of elastic-wave propagation in a strand," *J. Acoust. Soc. Am.*, vol. 103, no. 6, pp. 3370–3375, 1998.

[27] F. Treyssède, "Dispersion curve veering of longitudinal guided waves propagating inside prestressed seven-wire strands," *J. Sound Vib.*, vol. 367, pp. 56–68, 2016.

[28] X. Liu, B. Wu, F. Qin, C. He, and Q. Han, "Observation of ultrasonic guided wave propagation behaviours in pre-stressed multi-wire structures," *Ultrasonics*, vol. 73, pp. 196–205, 2017.

[29] G. A. Washer, *The Acoustoelastic Effect in Prestressing Tendons*. PhD thesis, Johns Hopkins University, 2001.

[30] S. Chaki and G. Bourse, "Guided ultrasonic waves for non-destructive monitoring of the stress levels in prestressed steel strands," *Ultrasonics*, vol. 49, no. 2, pp. 162–171, 2009.

[31] H.-L. Chen, Y. He, and H. V. GangaRao, "Measurement of prestress force in the rods of stressed timber bridges using stress waves," *Mater. Eval.*, vol. 56, no. 8, pp. 977–981, 1998.

[32] H.-L. Chen and K. Wissawapaisal, "Measurement of tensile forces in a seven-wire prestressing strand using stress waves," *J. Eng. Mech.*, vol. 127, no. 6, pp. 599–606, 2001.

[33] F. Lanza di Scalea, P. Rizzo, and F. Seible, "Stress measurement and defect detection in steel strands by guided stress waves," *J. Mater. Civ. Eng.*, vol. 15, no. 3, pp. 219–227, 2003.

[34] L. Pochhammer, "Ueber die fortpflanzungsgeschwindigkeiten kleiner schwingungen in einem unbegrenzten isotropen kreiscylinder," *J. Reine Angew. Math.*, vol. 81, pp. 324–336, 1876.

[35] T. R. Meeker and A. H. Meitzler, "Guided Wave Propagation in Elongated Cylinders and Plates," in *Physical Acoustics* (W. P. Mason and R. N. Thurston, eds.), ch. 2, pp. 111–167, New York: Academic Press, 1st ed., 1964.

[36] P. Rizzo, "Ultrasonic wave propagation in progressively loaded multi-wire strands," *Exp. Mech.*, vol. 46, pp. 297–306, 2006.

[37] I. Bartoli, S. Salamone, R. R. Phillips, F. Lanza di Scalea, and C. S. Sikorsky, "Use of interwire ultrasonic leakage to quantify loss of prestress in multiwire tendons," *J. Eng. Mech.*, vol. 137, no. 5, pp. 324–333, 2011.

[38] C. Nucera and F. Lanza di Scalea, "Monitoring load levels in multi-wire strands by nonlinear ultrasonic waves," *Struct. Health Monit.*, vol. 10, no. 6, pp. 617–629, 2011.

[39] X. H. Wan, N. Xu, Q. Q. Guo, and J. Chen, "Load monitoring in multiwire strands by ultrasonic second harmonic measurements," in *7th APWSHM*, (Hong Kong), 2018.

[40] H. Kwun and K. A. Bartels, "Experimental observation of elastic-wave dispersion in bounded solids of various configurations," *J. Acoust. Soc. Am.*, vol. 99, no. 1, pp. 962–968, 1996.

[41] S. Ramadan, L. Gaillet, C. Tessier, and H. Idrissi, "Detection of stress corrosion cracking of high-strength steel used in prestressed concrete structures by acoustic emission technique," *Applied Surface Science*, vol. 254, no. 8, pp. 2255–2261, 2008.

[42] S. E. Dunn, J. D. Young, W. H. Hartt, and R. P. Brown, "Acoustic emission characterization of corrosion induced damage in reinforced concrete," *Corrosion*, vol. 40, no. 7, pp. 339–343, 1984.

[43] R. Joseph, M. Y. Bhuiyan, and V. Giurgiutiu, "Acoustic emission from vibration of cracked sheet-metal samples," *Eng. Fract. Mech.*, vol. 217, p. 106544, 2019.

[44] E. Pomponi and A. Vinogradov, "A real-time approach to acoustic emission clustering," *Mech. Syst. Signal Pr.*, vol. 40, no. 2, pp. 791–804, 2013.

[45] A. D. Zdunek, D. Prine, Z. Li, E. Landis, and S. Shah, "Early detection of steel rebar corrosion by acoustic emission monitoring," in *CORROSION95*, (Houston, TX), pp. 1–9, NACE, Int., 1995.

[46] M. Ing, S. Austin, and R. Lyons, "Cover zone properties influencing acoustic emission due to corrosion," *Cement Concrete Res.*, vol. 35, no. 2, pp. 284–295, 2005.

[47] M. Ohtsu, K. Mori, and Y. Kawasaki, "Corrosion process and mechanisms of corrosion-induced cracks in reinforced concrete identified by AE analysis," *Strain*, vol. 47, pp. 179–186, 2011.

[48] J. Mangual, M. ElBatanouny, P. Ziehl, and F. Matta, "Corrosion damage quantification of prestressing strands using acoustic emission," *J. Mater. Civ. Eng.*, vol. 25, no. 9, pp. 1326–1334, 2013.

[49] M. K. ElBatanouny, J. Mangual, P. H. Ziehl, and F. Matta, "Early corrosion detection in prestressed concrete girders using acoustic emission," *J. Mater. Civ. Eng.*, vol. 26, no. 3, pp. 504–511, 2014.

[50] M. S. Weng, S. E. Dunn, W. H. Hartt, and R. P. Brown, "Application of acoustic emission to detection of reinforcing steel corrosion in concrete," *Corrosion*, vol. 38, no. 1, pp. 9–14, 1982.

[51] Z. Li, F. Li, A. Zdunek, E. Landis, and S. P. Shah, "Application of acoustic emission technique to detection of reinforcing steel corrosion in concrete," *ACI Mater. J.*, vol. 95, no. 1, pp. 68–76, 1998.

[52] D.-J. Yoon, W. J. Weiss, and S. P. Shah, "Assessing damage in corroded reinforced concrete using acoustic emission," *J. Eng. Mech.*, vol. 126, no. 3, pp. 273–283, 2000.

[53] S. Patil, B. Karkare, and S. Goyal, "Acoustic emission vis-a-vis electrochemical techniques for corrosion monitoring of reinforced concrete element," *Constr. Build. Mater.*, vol. 68, pp. 326–332, 2014.

[54] D. Li, W. Yang, and W. Zhang, "Cluster analysis of stress corrosion mechanisms for steel wires used in bridge cables through acoustic emission particle swarm optimization," *Ultrasonics*, vol. 77, pp. 22–31, 2017.

[55] M. Di Benedetti, G. Loreto, F. Matta, and A. Nanni, "Acoustic emission historic index and frequency spectrum of reinforced concrete under accelerated corrosion," *J. Mater. Civ. Eng.*, vol. 26, no. 9, p. 04014059, 2014.

[56] G. Carlsson, "Topology and data," *B. Am. Math. Soc.*, vol. 46, no. 2, pp. 255–308, 2009.

[57] J. A. Perea and J. Harer, "Sliding windows and persistence: An application of topological methods to signal analysis," *Found. Comput. Math.*, vol. 15, no. 3, pp. 799–838, 2015.

[58] P. Y. Lum, G. Singh, A. Lehman, T. Ishkanov, M. Vejdemo-Johansson, M. Alagappan, J. Carlsson, and G. Carlsson, "Extracting insights from the shape of complex data using topology," *Scientific Reports*, vol. 3, pp. 1–7, 2013.

[59] M. Z. Li, M. S. Ryerson, and H. Balakrishnan, "Topological data analysis for aviation applications," *Transport. Res. E*, vol. 128, pp. 149–174, 2019.

[60] C. R. Farrar and K. Worden, *Structural Health Monitoring: A Machine Learning Perspective*. John Wiley & Sons, 1st ed., 2013.

[61] B. Dubuc, A. Ebrahimkhanlou, and S. Salamone, "Stress measurement in seven-wire strands using higher order guided ultrasonic wave modes," *Transp. Res. Rec.*, vol. 2672, no. 41, pp. 123–131, 2018.

[62] B. Dubuc, A. Ebrahimkhanlou, and S. Salamone, "Higher order longitudinal guided wave modes in axially stressed seven-wire strands," *Ultrasonics*, vol. 84, pp. 382–391, 2018.

[63] B. Dubuc, A. Ebrahimkhanlou, and S. Salamone, "A spectral method for computing the effect of stress on guided modes in plates and rods," in *Health Monitoring of Structural and Biological Systems* (T. Kundu, ed.), vol. 10600, (Denver), p. 106001Z, SPIE, 2018.

[64] B. Dubuc, A. Ebrahimkhanlou, and S. Salamone, "Corrosion monitoring of prestressed concrete structures by using topological analysis of acoustic emission data," *Smart Mater. Struct.*, vol. 28, no. 5, p. 055001, 2019.

[65] B. Dubuc, A. Ebrahimkhanlou, and S. Salamone, "Data fusion approach for characterization of corrosion-induced stress change in prestressing strands using modulated higher-order guided ultrasonic waves," in *Health Monitoring of Structural and Biological Systems* (P. Fromme, ed.), vol. 10972, p. 109721D, SPIE, 2019.

[66] B. Dubuc, A. Ebrahimkhanlou, and S. Salamone, "Stress monitoring of prestressing strands in corrosive environments using modulated higher-order guided ultrasonic waves," *Struct. Health Monit.*, vol. 19, no. 1, pp. 202–214, 2020.

[67] B. Dubuc, A. Ebrahimkhanlou, K. Sitaropoulos, and S. Salamone, "Topological-based acoustic emission data analysis for passive corrosion monitoring in prestressed concrete structures," in *Health Monitoring of Structural and Biological Systems* (P. Fromme and Z. Su, eds.), vol. 11381, (Anaheim), p. 113811T, SPIE, 2020.

[68] A. E. Green and W. Zerna, *Theoretical Elasticity*. Dover, 2nd ed., 1968.

[69] E. S. Suhubi, "Small longitudinal vibration of an initially stretched circular cylinder," *Int. J. Engng. Sci.*, vol. 2, pp. 509–517, 1965.

[70] W. Flugge, *Tensor Analysis and Continuum Mechanics*. Heidelberg: Springer-Verlag, 1972.

[71] D. S. Hughes and J. L. Kelly, "Second-order elastic deformation of solids," *Phys. Rev.*, vol. 92, no. 5, pp. 1145–1149, 1953.

[72] Y.-H. Pao and U. Gamer, "Acoustoelastic waves in orthotropic media," *J. Acoust. Soc. Am.*, vol. 77, no. 3, pp. 806–812, 1985.

[73] F. D. Murnaghan, *Finite Deformation of an Elastic Solid*. New York: John Wiley & Sons, 1st ed., 1951.

[74] R. S. Rivlin, "The solution of problems in second order elasticity theory," *J. Ratl. Mech. Anal.*, vol. 2, pp. 53–81, 1953.

[75] R. N. Thurston and K. Brugger, "Third-order elastic constants and the velocity of small amplitude elastic waves in homogeneously stressed media," *Phys. Rev.*, vol. 133, no. 6A, pp. A1604–A1610, 1964.

[76] R. A. Toupin and B. Bernstein, "Sound waves in deformed perfectly elastic materials. Acoustoelastic effect," *J. Acoust. Soc. Am.*, vol. 33, no. 2, pp. 216–225, 1961.

[77] L. D. Landau and E. M. Lifshitz, *Theory of Elasticity*. Oxford: Pergamon Press, 2nd ed., 1970.

[78] A. C. Eringen and E. S. Suhubi, *Elastodynamics*. New York: Academic Press, 1st ed., 1974.

[79] A. Tverdokhlebov, "On the acoustoelastic effect," *J. Acoust. Soc. Am.*, vol. 73, no. 6, pp. 2006–2012, 1983.

[80] S. Kostek, B. K. Sinha, and A. N. Norris, "Third-order elastic constants for an inviscid fluid," *J. Acoust. Soc. Am.*, vol. 94, no. 5, pp. 3014–3017, 1993.

[81] F. D. Murnaghan, "Finite deformations of an elastic solid," *Am. J. Math.*, vol. 59, no. 2, pp. 235–260, 1937.

[82] J. D. Achenbach, *Wave Propagation in Elastic Solids*. Amsterdam: North Holland Publishing Co., 1st ed., 1973.

[83] J. Holder and A. V. Granato, "Third-Order Elastic Constants and Thermal Equilibrium Properties of Solids," in *Physical Acoustics* (W. P. Mason and R. N. Thurston, eds.), ch. 5, pp. 237–279, New York: Academic Press, 1st ed., 1971.

[84] S. Machida and A. J. Durelli, "Response of a strand to axial and torsional displacements," *J. Mech. Eng. Sci.*, vol. 15, no. 4, pp. 241–251, 1973.

[85] I. Bartoli, *Structural Health Monitoring By Ultrasonic Guided Waves*. PhD thesis, UC San Diego, 2007.

[86] I. Bartoli, G. Castellazzi, A. Marzani, and S. Salamone, "Prediction of stress waves propagation in progressively loaded seven wire strands," in *Sensors and Smart Structures Technologies for Civil, Mechanical, and Aerospace Systems* (M. Tomizuka, C.-B. Yun, and J. P. Lynch, eds.), vol. 8345, (San Diego, CA), p. 834505, 2012.

[87] D. Husson, "A perturbation theory for the acoustoelastic effect of surface waves," *J. Appl. Phys.*, vol. 57, no. 5, pp. 1562–1568, 1985.

[88] K. F. Graff, *Wave Motion in Elastic Solids*. London: Oxford University Press, 1st ed., 1975.

[89] M. J. S. Lowe, "Matrix techniques for modeling ultrasonic waves in multilayered media," *IEEE T. Ultrason. Ferr.*, vol. 42, no. 4, pp. 525–542, 1995.

[90] L. N. Trefethen, *Spectral Methods in Matlab*. Philadelphia, PA: SIAM, 1st ed., 2000.

[91] L. Brillouin, *Wave Propagation and Group Velocity*. New York: Academic Press, 1st ed., 1960.

[92] R. T. Smith, R. Stern, and R. W. B. Stephens, "Third-order elastic moduli of polycrystalline metals from ultrasonic velocity measurements," *J. Acoust. Soc. Am.*, vol. 40, no. 5, pp. 1002–1008, 1966.

[93] M. Onoe, H. D. McNiven, and R. D. Mindlin, "Dispersion of axially symmetric waves in elastic rods," *J. Appl. Mech.*, vol. 29, no. 4, pp. 729–734, 1962.

[94] M. G. Silk and K. F. Bainton, "The propagation in metal tubing of ultrasonic wave modes equivalent to Lamb waves," *Ultrasonics*, vol. 17, no. 1, pp. 11–19, 1979.

[95] R. D. Mindlin, "Waves and Vibrations in Isotropic, Elastic Plates," in *Structural Mechanics* (J. N. Goodier and N. Hoff, eds.), pp. 199–232, Oxford, UK: Pergamon Press, 1st ed., 1960.

[96] I. Tolstoy and E. Usdin, "Wave propagation in elastic plates: Low and high mode dispersion," *J. Acoust. Soc. Am.*, vol. 29, no. 1, pp. 37–42, 1957.

[97] B. N. Pavlakovic, M. J. S. Lowe, and P. Cawley, "High-frequency low-loss ultrasonic modes in imbedded bars," *J. Appl. Mech.*, vol. 68, no. 1, pp. 67–75, 2001.

[98] B. Dubuc, A. Ebrahimkhanlou, and S. Salamone, "The effect of applied stress on the phase and group velocity of guided waves in anisotropic plates," *J. Acoust. Soc. Am.*, vol. 142, no. 6, pp. 3553–3563, 2017.

[99] N. Gandhi, J. E. Michaels, and S. J. Lee, "Acoustoelastic Lamb wave propagation in biaxially stressed plates," *J. Acoust. Soc. Am.*, vol. 132, no. 3, pp. 1284–1293, 2012.

[100] S. G. Mallat, *A Wavelet Tour of Signal Processing*. Amsterdam: Academic Press, 3rd ed., 2009.

[101] K. Kishimoto, H. Inoue, M. Hamada, and T. Shibuya, "Time frequency analysis of dispersive waves by means of wavelet transform," *J. Appl. Mech.*, vol. 62, no. 4, pp. 841–846, 1995.

[102] D. L. Hall and J. Llinas, "An introduction to multisensor data fusion," *Proc. IEEE*, vol. 85, no. 1, pp. 6–23, 1997.

[103] C. E. Rasmussen and C. K. I. Williams, *Gaussian Processes for Machine Learning*. Cambridge, MA: MIT Press, 2006.

[104] W. H. Press, S. A. Teukolsky, W. T. Vetterling, and B. P. Flannery, *Numerical Recipes in Fortran 77: The Art of Scientific Computing*. Cambridge University Press, 2nd ed., 1997.

[105] M. Ohtsu, T. Isoda, and Y. Tomoda, "Acoustic emission techniques standardized for concrete structures," *J. Acoust. Emission*, vol. 25, pp. 21–32, 2007.

[106] K. Ohno and M. Ohtsu, "Crack classification in concrete based on acoustic emission," *Constr. Build. Mater.*, vol. 24, pp. 2339–2346, 2010.

[107] P. J. Shull, *Nondestructive Evaluation: Theory, Techniques, and Applications*. New York: Marcel Dekker, Inc., 1st ed., 2002.

[108] A. Hatcher, *Algebraic Topology*. Cambridge: Cambridge University Press, 1st ed., 2001.

[109] R. Ghrist, "Barcodes: The persistent topology of data," *B. Am. Math. Soc.*, vol. 45, no. 1, pp. 61–75, 2008.

[110] V. de Silva and G. Carlsson, "Topological estimation using witness complexes," in *Symposium on Point-Based Graphics*, pp. 157–166, 2004.

[111] H. Adams, A. Tausz, and M. Vejdemo-Johansson, "javaPlex : A research software package for persistent (co)homology," in *4th ICMS*, pp. 129–136, Springer, 2014.

[112] H. Edelsbrunner, D. Letscher, and A. Zomorodian, "Topological persistence and simplification," *Discrete and Computational Geometry*, vol. 28, no. 4, pp. 511–533, 2002.

[113] M. Vejdemo-Johansson and P. Skraba, "Topology, Big Data, and Optimization," in *Big Data Optimization: Recent Challenges and Developments* (J. Kacprzyk, ed.), ch. 7, pp. 147–176, Springer, 1st ed., 2016.

[114] L. R. Rabiner, "A tutorial on hidden Markov models and selected applications in speech recognition," *Proc. IEEE*, vol. 77, no. 2, pp. 257–286, 1989.

[115] C. M. Bishop, *Pattern Recognition and Machine Learning*. Springer, 2006.

[116] L. Himmelmann, "HMM – Hidden Markov Models," 2015.

[117] ASTM, "ASTM A416/A416M – Standard Specification for Low-Relaxation, Seven-Wire Steel Strand for Prestressed Concrete," 2016.

[118] ASTM, "ASTM F2832 – Standard Guide for Accelerated Corrosion Testing for Mechanical Fasteners," 2011.

[119] R. E. Melchers, "Modeling of marine immersion corrosion for mild and low-alloy steels–Part 1: Phenomenological model," *Corrosion*, vol. 59, no. 4, pp. 319–334, 2003.

[120] S. C. Barton, G. W. Vermaas, P. F. Duby, A. C. West, and R. Betti, "Accelerated corrosion and embrittlement of high-strength bridge wire," *J. Mater. Civ. Eng.*, vol. 12, no. 1, pp. 33–38, 2000.

[121] Z. Liu, J. Zhao, B. Wu, and H. Cunfu, "Temperature dependence of ultrasonic longitudinal guided wave propagation in long range steel strands," *Chinese J. Mech. Eng.*, vol. 24, no. 3, pp. 487–494, 2011.

[122] JCMS, "JCMS-III B5706: Monitoring method for active cracks in concrete by acoustic emission," 2003.

[123] K. A. T. Vu, M. G. Stewart, and J. Mullard, "Corrosion-induced cracking: Experimental data and predictive models," *ACI Struct. J.*, vol. 102, no. 5, pp. 719–726, 2005.

[124] P. J. Webster and G. Mills, "Residual stresses in a steel strand," *Physica B*, vol. 241-243, pp. 1270–1273, 1998.

[125] B. Dubuc, A. Ebrahimkhanlou, and S. Salamone, "Computation of propagating and non-propagating guided modes in nonuniformly stressed plates using spectral methods," *J. Acoust. Soc. Am.*, vol. 143, no. 6, pp. 3220–3230, 2018.

[126] K. Peddeti and S. Santhanam, "Dispersion curves for Lamb wave propagation in prestressed plates using a semi-analytical finite element analysis," *J. Acoust. Soc. Am.*, vol. 143, no. 2, pp. 829–840, 2018.

[127] F. Chazal and B. Michel, "An introduction to topological data analysis: fundamental and practical aspects for data scientists," pp. 1–38, 2017.